Technical Physics Letters, Vol. 27, No. 2, 2001, pp. 102–103. Translated from Pis'ma v Zhurnal Tekhnicheskoĭ Fiziki, Vol. 27, No. 3, 2001, pp. 31–35.

Dispersive Resonators with Volume Holographic Gratings

E. A. Tikhonov, V. I. Bezrodnyĭ, and T. N. Smirnova

Institute of Physics, National Academy of Sciences of Ukraine, Kiev, Ukraine

Received August 2, 2000

Abstract—A dispersive resonator with volume holographic phase gratings for a tunable laser is described. The experimental results showed advantages of these resonators over the analogous devices using blaze-angle reflection relief gratings. © *2001 MAIK "Nauka/Interperiodica".*

Volume holographic gratings (VHGs) belong to the class of optical diffraction elements with dispersion obeying the Bragg condition [1]. There are several types of holographic media with phase response in which the VHG recording is possible (bichromated gelatin, photopolymers, photorefractive crystals). From the standpoint of obtaining the transmission diffraction gratings, the self-developing photopolymers are the most promising media with respect to both the recording technology (real-time recording) and the level of record characteristics attained [2, 3].

Within the framework of a two-wave theory [1], the angular ($\Delta\theta$) and spectral ($\Delta\lambda$) selectivity of transmission VHGs with a harmonic profile of the refractive index modulation are determined by the relationships

$$2\Delta\theta \approx \frac{\Lambda}{T}, \tag{1a}$$

$$2\Delta\lambda \approx \frac{\lambda \cot\theta_0 \Lambda}{T}, \tag{1b}$$

where Λ is the grating period, T is the grating thickness, and θ_0 is the Bragg angle. As seen from the formulas, the grating thickness T is a key parameter controlling both the angular and spectral VHG selectivity. Accordingly, the transmission VHGs differ from the reflection relief gratings by the ability to provide for the spectral-angular selectivity. With respect to the possibility of variation of the T value, photopolymers are advantageous to other holographic recording media [4].

In contrast to the reflection relief gratings, where the resolution is determined by the total number of lines within the beam aperture, the resolution of VHGs is defined as

$$\lambda/\delta\lambda = (T/\Lambda)\tan\theta_0. \tag{2}$$

This characteristic, as well as the resolution of reflection gratings, is essentially the effective number of phase planes of the grating that contribute to the diffraction. As seen, the resolving power of a transmission Bragg grating is independent of the transverse beam size. In addition, the presence of the angular selectivity removes the requirement of illuminating the Bragg grating with a collimated beam. Therefore, using such gratings in all spectral instruments and, in particular, in dispersive resonators, simplifies the instrument design. In order to provide for a narrow generation linewidth, the conventional dispersive resonators for tunable lasers with relief gratings either contain telescopic systems of beam expansion [5] or employ a "glancing" beam incidence onto the grating in order to increase N [6].

At present, VHGs are still not systematically employed in the optical instrument building, since no obvious advantages were reported for these devices in comparison with the relief gratings on photoresists with reflection coatings. The latter gratings are widely used in the spectral instruments and lasers, replacing cut crystal gratings with the well-established optical schemes retained.

Below, we present the results of the investigation of a dispersive resonator with volume holographic phase gratings in a tunable laser. In creating such resonators, the main purpose is to provide for a homogeneous generation in combination with a sufficiently simple mechanism of frequency tuning within the gain contour limits of a particular laser medium employed.

For self-developing photopolymers of the FPK-488 grade, the range of thickness variation with the η value retained on a 100% level extends from 10 to 1000 μm [4], which allows the angular ($2\Delta\theta$) and spectral ($2\Delta\lambda$) half-widths to vary over several orders of magnitude. For example, at λ = 600 nm, a grating with the period Λ = 1 μm and T = 10 μm has $2\Delta\theta = 5.3°$ and $2\Delta\lambda$ = 60 nm, while an increase in the thickness to T = 200 μm gives $2\Delta\lambda$ = 3 nm. Selecting (for a grating with T = 10 μm) the Bragg angle with zero detuning at a wavelength corresponding to the maximum gain, we obtain a tuning range of $\Delta\lambda = \pm 300$ nm with a mirror tilt angle varied within ±4.5°. For a grating with T = 200 μm, the ability of tuning in the same wavelength range would require rotating the mirror between the same limits. However, the angular range of ±4.5° exceeds the angular selectivity of this grating (0.26°) by one and a half orders of magnitude, which implies that the tuning within 60 nm cannot be provided in this

1063-7850/01/2702-0102$21.00

case by only rotating the mirror and it is necessary to jointly rotate the mirror–grating system.

Figure 1 shows the scheme of a laser with the dispersive resonator employing a volume transmission grating. The laser frequency tuning is achieved by rotating one of the mirrors (M_1 or M_2) with an immobile grating. The laser radiation can be conventionally extracted from the resonator via a semitransparent mirror (M_2). The presence of a zero-order diffraction beam at $\eta < 100\%$ allows the radiation to be extracted via outputs 1 and 2 (in this case, mirror M_2 can be totally reflecting).

In order to decrease the laser linewidth (in the limit to provide for a single-mode lasing at the longitudinal mode), it is necessary to increase the grating thickness *T*. However, the laser frequency tuning within the gain contour limits of the active element (AE) medium would require synchronous rotation of the joint mirror–grating system. The tuning is performed by fixing the mirror–grating angle (α = const) and rotating this unit about an axis denoted by a star symbol in Fig. 1 (the axis is perpendicular to the figure plane).

Figure 2 shows typical tuning spectra of a laser with dyes in a poly(urethane) matrix employing longitudinal pulse pumping with a second harmonic of a YAG:Nd^{3+} laser. The dispersive resonator is based on a VHG with $N = 1200$ mm^{-1} and $T = 10$ μm.

The dispersive resonator with VHG exhibits a considerable difference from an analogous system employing a blaze-angle reflection relief grating. Indeed, the results of measuring the angular divergence (averaged over the laser pulse width ≈20 ns) for the lasers with equal resonator lengths (25 cm) showed this value to be systematically lower for a resonator with VHG (N = 1200 mm^{-1}, $T = 20$ μm) than for the reflection relief grating system with the same *N*. The laser beam divergence was 3.5 mrad (at the threshold) and 4.5 mrad (10-fold over-threshold pumping) in the laser with the reflection relief grating against 2 and 2.5 mrad, respectively, in the laser with VHG (both resonators not involving telescope systems).

The combination of angular dispersion and selectivity in VHGs considerably increases the spectral selectivity of a laser resonator as a result of a smaller effect of the beam divergence upon the laser linewidth. For the gratings with equal dispersion ($N = 1200$ mm^{-1}), the laser linewidth for a resonator with VHG was approximately one-tenth of that for the resonator with a reflection relief grating. Use of a grating with $T = 100$ μm ($\Delta\theta \approx 0.5°$) allowed the laser linewidth to be reduced to 1.5 pm.

It should be noted that a high selectivity of the Bragg resonance in thick holographic gratings may allow the dispersive resonators to be completely excluded in a laser employing a configuration of two equivalent gratings with differential dispersion [7].

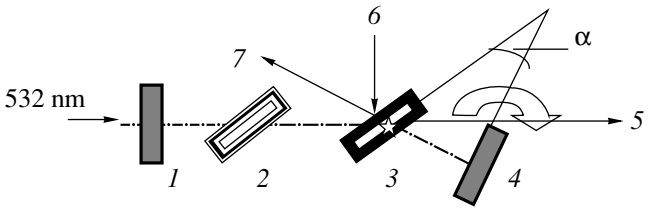

Fig. 1. The optical scheme of a tunable dye laser with a dispersive resonator employing VHG: (*1*) mirror M_1; (*2*) active element (AE); (*3*) VHG; (*4*) mirror M_2; (*5*) output 1; (*6*) rotation axis; (*7*) output 2.

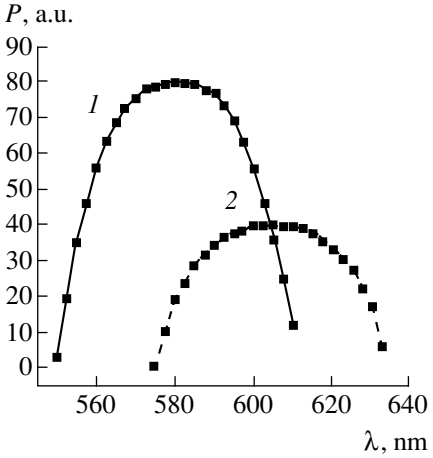

Fig. 2. The plots of laser output power (*P*) versus laser wavelength for (*1*) pyrometene-597 and (*2*) phenalinone-160.

REFERENCES

1. H. Kogelnik, Bell Syst. Tech. J. **48**, 2909 (1969).
2. E. A. Tikhonov, É. S. Gyul'nazarov, and T. N. Smirnova, Kvantovaya Élektron. (Kiev) **40**, 3 (1991).
3. E. A. Tikhonov, T. N. Smirnova, and T. A. Sarbaev, Proc. SPIE **1252**, 322 (1994).
4. O. V. Sakhno, T. N. Smirnova, and E. A. Tikhonov, Zh. Tekh. Fiz. **63** (12), 70 (1993) [Tech. Phys. **38**, 1071 (1993)].
5. F. J. Duarte, Opt. Commun. **117** (5), 480 (1995).
6. D. Lo, S. K. Lam, C. Ye, and K. S. Lam, Opt. Commun. **156** (4), 316 (1998).
7. I. A. Strelets and E. A. Tikhonov, Zh. Tekh. Fiz. **65** (12), 60 (1995) [Tech. Phys. **40**, 1236 (1995)].

Translated by P. Pozdeev

Technical Physics Letters, Vol. 27, No. 2, 2001, pp. 104–107. Translated from Pis'ma v Zhurnal Tekhnicheskoĭ Fiziki, Vol. 27, No. 3, 2001, pp. 36–44.

Nonlinear Response of the IVCT Band in the Absorption Spectra of Molybdenum Blue and Berlin Blue

A. A. Bugaev and S. E. Nikitin

Ioffe Physicotechnical Institute, Russian Academy of Sciences, St. Petersburg, 194021 Russia

Received August 16, 2000

Abstract—A mechanism of the nonlinear absorption response related to the charge transfer in mixed-valence compounds was studied by measuring their spectral and temporal characteristics. It is shown that a photoinduced variation of the absorption response is related to a longwave shift of the IVCT band. A qualitative description of the process is proposed that is based on the model of excitation of a three-band scheme where each level is capable of decaying to the continuum. © *2001 MAIK "Nauka/Interperiodica".*

The optical transitions related to excitation and the subsequent transfer of electrons from strongly to weakly reduced ions, called the intervalence charge transfer (IVCT), are observed in a broad class of compounds with ambivalent elements, including the transition metals (Mn^{+2}/Mn^{+3}, W^{+5}/W^{+6}, Mo^{+5}/Mo^{+6}, Ti^{+3}/Ti^{+4}), elements of Groups V and VIII (As^{+3}/As^{+5}, Sb^{+3}/Sb^{+5}, Fe^{+2}/Fe^{+3}), and their combinations such as (Fe^{+2},Ti^{+4})/(Fe^{+3},Ti^{+3}) and (Mn^{+2},Ti^{+4})/(Mn^{+3},Ti^{+3}). Extensive investigations were devoted to studying the optical properties, chemical bond nature, and energy level structure in these compounds and the dynamics of photoinduced charge transfer [1–9].

The interest in these objects is explained both by a fundamental character of the charge transfer problem [4] and by the unusual magnetic properties of these compounds (molecular magnetism) [10, 11]. An additional interest is stimulated by the recent results [12, 13] showing a considerable (~30%) change in the absorption coefficient upon a picosecond excitation of the IVCT band in Molybdenum Blue and the subsequent relaxation on the picosecond time scale.

Below, we report on the results of investigation of a mechanism of the nonlinear IVCT absorption band response in various compounds with ambivalent elements (Mo^{+5}/Mo^{+6}, Fe^{+2}/Fe^{+3}). It will be shown that a change in the absorption is related to a longwave shift of the IVCT band. A qualitative description of the process is proposed within the framework of a three-band excitation scheme.

The experiments were performed using a solid-state passive mode-locked YAG:Nd^{3+} laser with a single-pass amplifier, which generated single 30-ps pulses with an energy of 7–10 mJ at wavelength of 1.06 μm (pulse repetition rate, 1 Hz). For expanding the spectral range of the investigation, the main harmonic (1.17 eV) signal was converted into a second-harmonic (2.34 eV) pulse. This pulse excited via a transmission scheme an induced Raman scattering (IRS) pulse in a cell containing hydrogen at a pressure of 20 atm. The experiments were performed using both the fundamental frequency pulse (1.17 eV) and a picosecond IRS pulse of the first Stokes component (1.779 eV). The measurements were performed by the method of probing with preexcitation. According to this, a pulse was divided into two, and one of these pulses was transmitted via a channel with controlled delay and an attenuator (a halfwave plate and the Glan prism) that provided an intensity ratio of 1000 : 1 for the exciting and probing pulses. The two pulses were focused at a mutual angle of 10° within the volume of a 1-mm-thick cell containing the solution of a compound studied. The registration system was adjusted so that the data were taken only for a ratio of the second harmonic to the fundamental frequency energy within ±5% of the average value.

To provide for a general character of the results and make possible a comparison of the experimental data, we have used the compounds of two types possessing the IVCT transitions: Molybdenum Blue (an aqueous solution of ammonium heptamolybdate tetrahydrate $(NH_4)_6[Mo_7O_{24}] \cdot 4H_2O$ and citric acid $C_6H_8O_7$ with the concentrations 0.027 and 0.071 mol/dm^3, respectively) and Berlin Blue (an aqueous solution of the salts $K_4[Fe(CN_6)] \cdot 3H_2O$ and $FeCl_3$ with the concentrations 4.35×10^{-3} and 5.77×10^{-3} mol/dm^3, respectively, in an acid medium (HCl) at pH 2). The $[Mo_7O_{24}]^{6-}$ heptamolybdate solution was reduced (so as to obtain a blue color) by exposure to UV radiation with a wavelength of 365 nm. The exposure time was varied so as to obtain the absorption coefficient at the IVCT band close to the analogous value for Berlin Blue. Figure 1 shows typical absorption spectra in the region of the IVCT band for the solutions studied.

As is seen from Fig. 1, the charge-transfer transitions in Berlin Blue (BB) form an absorption band with a center of mass at 1.65 eV. A nonuniform character of the absorption decrease on the left wing of the band is clearly indicative of the presence of a certain substruc-

1063-7850/01/2702-0104$21.00 © 2001 MAIK "Nauka/Interperiodica"

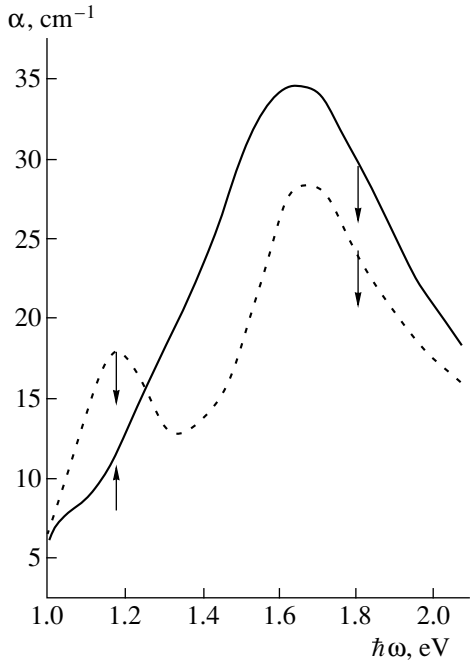

Fig. 1. Typical absorption spectra $\alpha = f(\hbar\omega)$ in the region of the IVCT band for Molybdenum Blue (dashed curve) and Berlin Blue (solid curve) solutions. The arrows indicate the wavelengths of excitation laser pulses; the arrow sense (up- vs. downward) indicates the direction of intensity variation (increase vs. decrease).

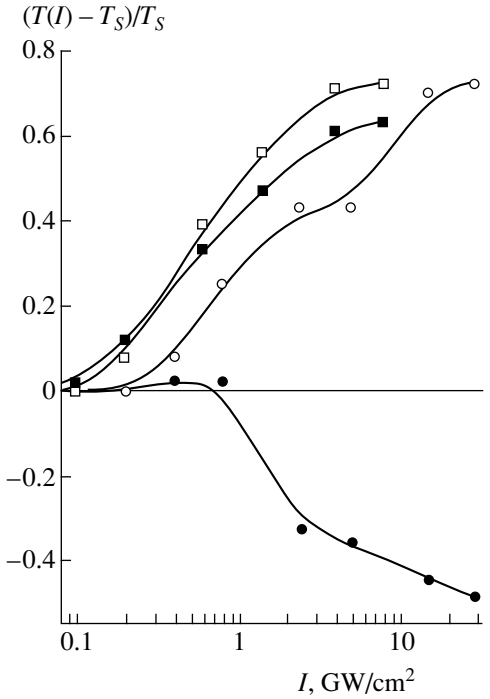

Fig. 2. The plots of the excitation pulse transmission $(T(I) - T_S)/T_S$ versus intensity for Molybdenum Blue (open symbols) and Berlin Blue (black symbols) solutions. The excitation quantum energy is $\hbar\omega_L$ = 1.779 (squares) and 1.17 eV (circles).

ture. In the spectrum of Molybdenum Blue (MB), the IVCT transitions form an absorption band with two peaks (1.65 and 1.18 eV). According to Fruchart *et al.* [14], these peaks represent two partly overlapping absorption bands, which are related to the charge-transfer transitions of two types between Mo^{5+} and Mo^{6+} ions differing by the character of terminal and angle Mo–O bonds in the Mo_6 octahedron.

The experiments with each solution included the measurements of two types. First, we measured the excitation pulse transmission as a function of its intensity. Second, we determined the probing pulse transmission as a function of the delay time relative to the excitation pulse at a constant amplitude of the latter pulse. Figure 2 shows the results of measurements of the photoinduced variation of the IVCT absorption band. These data reveal at least two features in the variation of excitation pulse transmission $(T(I) - T_S)/T_S$. First, the excitation with a laser pulse at a frequency occurring in the region of longer wavelengths ($\hbar\omega_L$ = 1.17 eV) with respect to the IVCT band center ($\hbar\omega_O$ = 1.65 eV) leads to a change in the solution absorption $\Delta\alpha$ that has a different sign for the MB ($\Delta\alpha < 0$) and BB ($\Delta\alpha > 0$) solutions, while excitation in the region of shorter wavelengths ($\hbar\omega_L$ = 1.779 eV, $\hbar\omega_L > \hbar\omega_O$) leads to a change of the same sign for both solutions ($\Delta\alpha < 0$).

The second feature, which was previously discussed in [12, 13], consists in a stepwise character of the $T(I)$ function observed for both solutions, which takes place in both media only in the case of excitation at $\hbar\omega_L$ = 1.17 eV. Moreover, the same behavior is observed for the excited state relaxation in both MB and BB solutions $T(\tau)$ on a picosecond time scale (Fig. 3).

We may state with high confidence that the experimental data represented in Fig. 2, which describe a change in the IVCT absorption band depending on the excitation intensity and wavelength in both media, correspond to a transformation of the spectra presented in Fig. 1. The transformation consists in a longwave shift of the IVCT band, probably with some change in the line shape. Using the results obtained in the previous work [12, 13] and in this study, we have established that a maximum possible change in the IVCT absorption intensity $\Delta\alpha_{max}$ obeys an approximate relationship $\Delta\alpha_{max} \simeq (0.3–0.35)\alpha_0$. From this it follows that the longwave shift of the IVCT band (Fig. 1) is approximately 150 meV. This behavior (red shift) is typical of the photoexcited complex polyatomic molecules (SiF_4, SF_6, CF_3Br, CF_3I) [15]. The spectrum of the excited state can be calculated upon determining the kinetic coefficients of the $D_{n, n+1}$ transition, the spectral dependence of which is controlled by the anharmonic frequency shift; the distribution of molecules over the

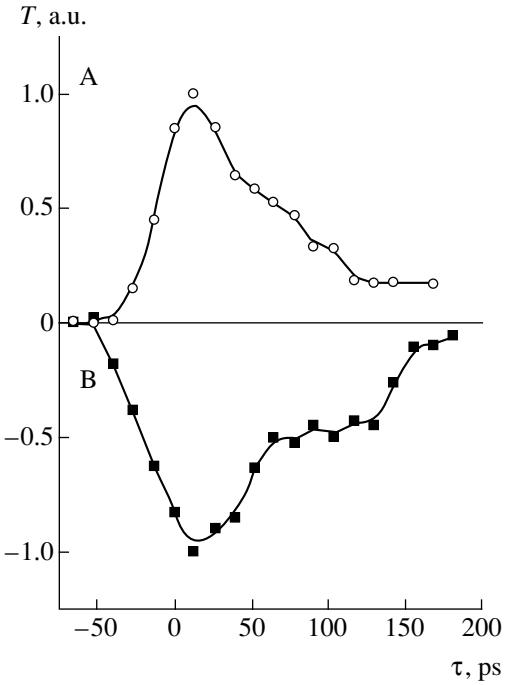

Fig. 3. The plots of the probing pulse transmission T versus the delay between probing and exciting pulses for Molybdenum Blue (A) and Berlin Blue (B) solutions; $\hbar\omega_L = 1.17$ eV.

whole phase volume; and the relationship between Δ, α, and β values:

$$D_{n,n+1} = \frac{\pi}{\hbar}E^2\mu_{01}^2\int I_1\delta_\omega \times \exp\left[-\frac{\hbar\omega}{kT}(I_1 + I_2 + I_3)\right]\left(\frac{\hbar\omega}{kT}\right)^3 dI_1 dI_2 dI_3, \quad (1)$$

where $\delta_\omega = \delta(2\alpha I_1 + \beta I_2 + \beta I_3 + \omega_O - \omega_L)$, α and β are the anharmonicity constants, $\Delta = \omega_L - \omega_O$ is the laser frequency detuning from the harmonic frequency, and I_i are the phase space occupancies.

Unfortunately, the calculation of the kinetic coefficients (1) in the general case possesses only a qualitative character because the function of the molecule distribution over the phase space, determining the fraction of this space corresponding to the vibrational motion, is usually not known with sufficient accuracy (while significantly differing from the distribution function in the state of thermal equilibrium) [15]. Let us consider the second feature of the transmission as a function of the pulse intensity, which consists in a stepwise character of the $T(I)$ function observed for both solutions. As noted above, this is observed only in the case of excitation at $\hbar\omega_L = 1.17$ eV. Previously [12, 13], we explained the stepwise shape of $T(I)$ using a scheme of three almost equidistant levels, in which a growth in the pulse intensity leads to a transition from single- to two-photon resonance with the occupation of all three levels. Taking into account the results obtained in this study, we must note that the model of a spectrum of a complicated molecule representing three discrete levels is a very strong idealization, since the interactions apparently involve large groups of levels occurring in the vicinity of the resonance.

We believe that a more realistic approach is provided by the model of excitation of a three-band system, in which every level in each band is related to the continuum. The latter relationship is manifested in that the mth level of the nth band ($n = 1, 2, 3$) may decay at a rate of $\gamma_{n,m}$ into the continuum, the density of the continuum states in the vicinity of the n, m level being $g_{n,m}$. A similar interaction was analyzed in [15] for the case of $\Gamma_3 \gg \Gamma_2 \gg \Gamma_1$ (Γ_i is the rate of decay for levels of the ith band averaged over the vicinity of the resonance). It was found that the excitation energy W transferred to the continuum is determined by the expression

$$W = \frac{D_1(D_2 + \Gamma_3)\Gamma_2 + 2D_1D_2\Gamma_3}{(D_1 + \Gamma_1)(D_1 + D_2 + \Gamma_2)(D_2 + \Gamma_3) - D_2^2(D_1 + \Gamma_1) - D_1^2(D_2 + \Gamma_3)}, \quad (2)$$

where $D_{1,(2)}$ are the kinetic coefficients of the transition from the first (second) to the second (third) band; $D = \pi g\mu^2 E_0^2/\hbar^2$.

Equation (2) shows that, as the pulse intensity E_0^2 increases, the absorbed energy initially grows, then (on reaching $D_1 > \Gamma_1$) exhibits saturation and remains approximately constant (for $D_1 > \Gamma_1$, $D_2 < \Gamma_2$), and eventually (for $D_2 > \Gamma_2$) increases again to reach a new saturation level for $D_2 > \Gamma_3$. Thus, the absorption exhibits sequential transition from transferring the band population to the continuum initially via the second and then via the third band. According to these notions, a relaxation of the excited state (Fig. 3) can be considered as the reverse process of trapping carriers from the continuum to the band levels. It is possible that this very situation is realized in our experiments on excitation of the IVCT absorption band.

Thus, we have studied the mixed-valence compounds of different types (Molybdenum Blue and Berlin Blue) and established general laws of a nonlinear response of the absorption band related to the charge transfer between ions of different valence. It is shown that the IVCT band excitation by picosecond pulses with frequencies higher or lower than the central frequency of this band leads to the wavelength shift of the IVCT band. The shift is explained by a spectral depen-

dence of the kinetic coefficients, which is determined by the anharmonic frequency shift and the distribution of molecules over the entire phase volume. It is demonstrated that the excitation of the nonlinear IVCT absorption response and its relaxation on a picosecond scale exhibit a stepwise character. These features are explained using a model of excitation of a three-band system in which every level of each band is capable of decaying into the continuum.

Acknowledgments. The authors are grateful to B.P. Zakharchenya for her interest and support of this work.

REFERENCES

1. M. T. Pope, *Heteropoly and Isopoly Oxometalates* (Springer-Verlag, Berlin, 1983).
2. M. T. Pope, in *Mixed-Valence Compounds*, Ed. by D. B. Brown (D. Reidel, Dordrecht, 1979); NATO Adv. Study Inst. Ser., Ser. C **58** (1979).
3. R. I. Buckley and R. J. H. Clark, Coord. Chem. Rev. **65** (2), 167 (1985).
4. M. B. Robin and P. Day, Adv. Inorg. Chem. Radiochem. **10** (3), 248 (1967).
5. M. D. Newton and N. Sutin, Annu. Rev. Phys. Chem. **35** (3), 437 (1984).
6. S. K. Doorn and J. T. Hupp, J. Am. Chem. Soc. **111** (2), 1142 (1989).
7. K. Tominaga, D. A. V. Kliner, A. I. Johnson, *et al.*, J. Chem. Phys. **98** (2), 1228 (1993).
8. G. C. Walker, P. F. Barbara, S. K. Doorn, *et al.*, J. Phys. Chem. **95** (4), 5712 (1991).
9. D. G. Evans, A. Nitzan, and M. A. Ratner, J. Chem. Phys. **108** (15), 6387 (1998).
10. O. Kahn, Nature **378** (4), 667 (1995).
11. S. Ferlay, T. Mallah, R. Quahés, *et al.*, Nature **378** (4), 701 (1995).
12. A. A. Bugayev and S. E. Nikitin, Opt. Commun. **180** (1–3), 69 (2000).
13. A. A. Bugaev and S. E. Nikitin, Pis'ma Zh. Tekh. Fiz. **26** (14), 91 (2000) [Tech. Phys. Lett. **26**, 634 (2000)].
14. J. M. Fruchart, G. Herve, J. P. Lannay, and R. Massart, J. Inorg. Nucl. Chem. **38** (11), 1627 (1976).
15. V. M. Akulin and N. V. Karlov, *Intense Resonance Interactions in Quantum Electronics* (Nauka, Moscow, 1987).

Translated by P. Pozdeev

Technical Physics Letters, Vol. 27, No. 2, 2001, pp. 108–109. Translated from Pis'ma v Zhurnal Tekhnicheskoĭ Fiziki, Vol. 27, No. 3, 2001, pp. 45–48.

The Localized Gas Discharge Etching of Materials

A. V. Abramov, E. A. Abramova, and I. S. Surovtsev

Voronezh State University, Voronezh, Russia

Received August 3, 2000

Abstract—It is demonstrated that a gas discharge can be localized between separate elements on the surface of electrodes with a preset geometry. The main characteristics of the localized discharge have been studied and the forms of this discharges are established. Using the localized discharge in a fluorine-containing gas medium, size-controlled etching of silicon and silicon dioxide with a resolution of 100 μm was performed without mask application. © *2001 MAIK "Nauka/Interperiodica".*

The existing methods of the "dry" etching of materials stipulate the plasma formation over a greater part of the working chamber volume. The size-controlled etching of materials under these conditions requires that the remaining part of the material surface would be protected from the plasma action by a mask. The etched area usually amounts to a very small fraction of the remaining (masked) surface in contact with the plasma, where the chemically active species are lost and the gas phase particles are deposited [1, 2], the characteristic time of this deposition process being ~10 s [3]. In order to maintain concentrations of the chemically active species and the gas pressure (P) on a constant level, the gas must be continuously supplied to the chamber. Thus, the gas and electric energy in these systems are low-efficient, while the power density (w) absorbed in the plasma usually does not exceed 1 W/cm^3.

The purpose of this work was to study the possibility of obtaining an RF gas discharge of a preset configuration, which can be used for the size-controlled etching of materials without mask application.

The discharge studied in this work was excited using a voltage with a frequency of f = 13.56 MHz. The plasma-forming gases were SF_6, CF_4, and air. For the plasma investigation by the actinometry method, 4–5 vol % Ar was added to the working gas mixture.

According to the approach to etching developed in this work, the gas discharge is generated only over the areas of the material surface that have to be processed. For this purpose, the surface of one electrode is engraved so as to form a negative image of the required etch pattern (Fig. 1). It was established that a necessary condition for the discharge localization at the protruding parts of the electrode surface is expressed by the following relationship: L, l, l_1, $l_2 \gg \lambda$, where λ is the electron mean free path in the plasma. For L, l, l_1, l_2 = 100 μm; $P = 10^4$ Pa; and the effective voltage drop across the discharge U_{RF} = 200 V, the w value amounts to several kW/cm^3. With this power density absorbed in the plasma, the concentration of F atoms (n_F) in the SF_6 discharge was several times greater than the initial concentration of molecules. In this plasma, the rate of simultaneous etching of five parallel grooves (50 mm long and 300 μm wide) in silicon was about 5 μm/s, which is two orders of magnitude greater than the value achieved in the conventional plasmachemical etching process. The isotropic character of etching in a localized discharge in SF_6 (observed for silicon etched with an aluminum mask) and the selective (sixfold) etching of silicon in comparison to SiO_2 are factors indicative of a predominantly chemical nature of this process.

During the localized discharge operation, the gas molecules are supplied to the discharge region from the working chamber volume as a result of diffusion driven by the partial gas pressure gradient and the temperature gradient. Since the localized discharge volume is much smaller than the chamber volume, the process can be effected in a closed system. The n_F value in the localized discharges in SF_6 and CF_4 remained constant for tens of minutes.

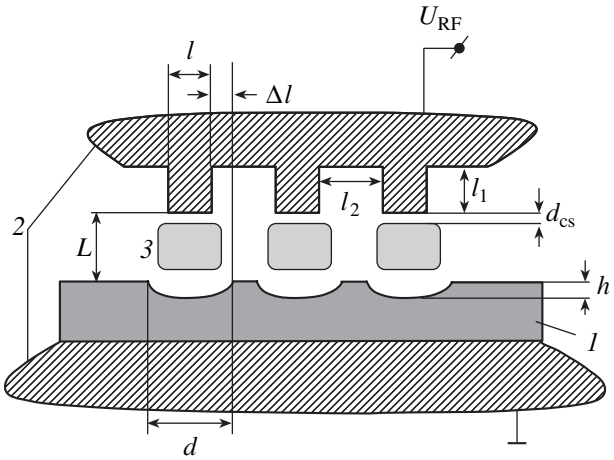

Fig. 1. A schematic diagram illustrating the localized discharge etching principle: (*1*) processed material; (*2*) profiled electrode; (*3*) plasma.

1063-7850/01/2702-0108$21.00 © 2001 MAIK "Nauka/Interperiodica"

In order to characterize the directionality of etching in a localized discharge, we introduce the etching anisotropy index (A) determined as a ratio of the etch depth h to the lateral groove etching Δl beyond the boundaries of projections of the protruding electrode element onto the initial material surface (Fig. 1). Figure 2 shows the etching profiles obtained using a single nickel electrode with a thickness of 100 μm and a length of 50 mm. As seen from these data, the A value increases with the gas pressure. The increase in A is probably explained by a decrease in the discharge region dimensions, since the electron concentration in the discharge is weakly dependent on the gas pressure, while the diffusion coefficient decreases in proportion to $\sim P^{-1}$. For L = const, an increase in the pressure was accompanied by a growth of the discharge onset voltage. This is undesirable for a number of reasons, the main of which is the risk of the discharge transformation from the glow to the arc regime. Therefore, the resolution of etching should be improved by simultaneously increasing P and decreasing L. However, this is usually hindered by the objective factor—a finite cathode space thickness (d_{cs}) corresponding to the discharge operation conditions employed. The d_{cs} value cannot exceed L (Fig. 1). The current–voltage characteristics of the localized discharge obtained in various gases and the corresponding values of current densities allowed us to classify the discharge as belonging to the normal glow type in the γ-form. The d_{cs} value for a discharge in the γ-form at $P \approx 10^4$ Pa amounts to ~100 μm [4].

In some cases, for a certain relationship between the L and P values, the RF discharge behaved as a glow discharge of the AC type. The transition from γ to AC discharge mode is characterized by a critical frequency $f_c \approx 330\ P^2$ Hz [4]. For $f < f_c$, the discharge operates in the AC pulse mode with the period between pulses increasing with the gals pressure (for L = const). This circumstance explained, in particular, a decrease in the rate of silicon etching with an increasing P observed under the central parts of the protruding electrode elements as well as some other effects that will be described in subsequent publications.

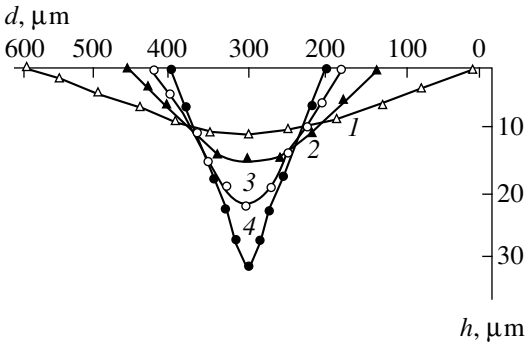

Fig. 2. The shapes of etch groove profiles observed in silicon etched by localized discharge in SF_6 at $P = 10^4$ (*1*), 2×10^4 (*2*), 3×10^4 (*3*), 4×10^4 Pa (*4*) and U_{RF} = 200 (*1*), 210 (*2*), 215 (*3*), 225 V (*4*); L = 50 μm, t = 20 s.

REFERENCES

1. G. K. Vinogradov, D. I. Slovetskiĭ, and T. V. Fedoseeva, Teplofiz. Vys. Temp. **22** (2), 225 (1984).
2. É. M. Vrublevskiĭ, I. S. Trubin, and A. V. Kholopov, Mikroélektronika **23** (4), 80 (1994).
3. A. V. Abramov, E. A. Abramova, and I. S. Surovtsev, in *Mathematical Modeling of Information Technology and Systems: Collection of Scientific Works* (Voronezh. Gos. Tekh. Akad., Voronezh, 2000), No. 1, pp. 268–272.
4. Yu. P. Raĭzer, M. N. Shneĭder, and R. A. Yatsenko, *High-Frequency Capacitive Discharge: Physics and Experimental Techniques* (Nauka, Moscow, 1995).

Translated by P. Pozdeev

Technical Physics Letters, Vol. 27, No. 2, 2001, pp. 110–111. Translated from Pis'ma v Zhurnal Tekhnicheskoĭ Fiziki, Vol. 27, No. 3, 2001, pp. 49–53.

Single-Crystal Iron Garnet Films with Increased Thermal Stability of Magnetization and Ferromagnetic Resonance Field

S. I. Yushchuk and P. S. Kostyuk

Lviv State Polytechnic University, Lviv, Ukraine

Received July 17, 2000

Abstract—A new method for selecting iron–yttrium garnet (IYG) film compositions is proposed and experimentally verified. Using this approach, it is possible to obtain thick IYG films with high magnetic characteristics. © *2001 MAIK "Nauka/Interperiodica".*

As reported previously [1], the films of gallium-substituted iron–yttrium garnet (IYG) exhibit a higher thermal stability of saturation magnetization and ferromagnetic resonance field when compared with pure IYG films. However, the gallium-doped films can be grown only with low degrees of substitution ($x \le 0.63$) and small thicknesses (not exceeding 5 μm) because of a considerable lattice mismatch between film and substrate.

In order to eliminate this drawback and obtain the IYG layers with thicknesses up to 70 μm, we used a modified process whereby (simultaneously with substituting gallium for iron) lanthanum ions were introduced into the IYG film composition to substitute for yttrium ions in dodecahedral positions. Possessing a greater ion radius (1.22 Å for La^{3+} versus 1.06 Å for Y^{3+}), lanthanum ions compensate for a decrease in the crystal lattice parameter in the IYG film caused by substituting small-size Ga^{3+} ions.

The epitaxial films of $Y_{3-y}La_yFe_{5-x}Ga_xO_{12}$ ($0.172 \le x \le 0.940$; $0.033 \le y \le 0.161$) were grown by liquid-phase epitaxy (LPE) on (111)-oriented gallium–gadolinium garnet (GGG) substrates. The LPE process was performed with a solution of garnet-forming oxides Y_2O_3, La_2O_3, Fe_2O_3, and Ga_2O_3 in a $PbO–B_2O_3$ solvent system. The charge composition was calculated using the Blank–Nielson R_1–R_5 molar ratios [2, 3] presented in the table with some other film parameters. The structures and compositions of the epitaxial films were studied on a scanning electron microscope with electron-probe microanalyzer of the CAMEBAX type.

A certain discrepancy between the calculated and experimentally measured values of the gallium (x) and lanthanum (y) content are apparently related to some features of the growth process and the mutual influence of substituting Ga^{3+} ions (and La^{3+}). The distribution coefficients for these ions were calculated using the following relationships [4]:

$$K_{Ga} = \frac{(X_{Ga}/X_{Ga} + X_{Fe})_f}{(X_{Ga}/X_{Ga} + X_{Fe})_m}; \quad K_{La} = \frac{(X_{La}/3)_f}{(X_{La}/X_{La} + X_Y)_m},$$

where X_{Ga}, X_{Fe}, X_Y, and X_{La} are the concentrations of

The compositions, molar ratios, lattice parameters, and dopant (Ga and La) distribution coefficients for IYG : (La,Ga) epitaxial films

Preset composition* (a.u.)		Molar ratios (a.u.)					Garnet composition (a.u.)		GGG substrate lattice parameter, Å	Film lattice parameter, Å	Distribution coefficient (a.u.)	
x	y	R_1	R_2	R_3	R_4	R_5	x	y	a_s	a_f	K_{Ga}^{3+}	K_{La}^{3+}
0.1	0.030	13	111	15.6	0.085	18	0.17	0.033	12.3826	12.3818	3.8	0.21
0.3	0.050	13	28	15.6	0.085	10.5	0.41	0.060	12.3821	12.3833	2.4	0.23
0.5	0.075	13	19	15.6	0.085	7.0	0.57	0.090	12.3826	12.3786	2.3	0.24
0.7	0.120	13	14	15.6	0.085	4.8	0.70	0.098	12.3822	12.3802	2.1	0.19
0.8	0.160	13	10.5	15.6	0.085	3.6	0.94	0.161	12.3822	12.3811	2.2	0.25

* Calculated for the gallium and lanthanum oxide content in the charge.

1063-7850/01/2702-0110$21.00 © 2001 MAIK "Nauka/Interperiodica"

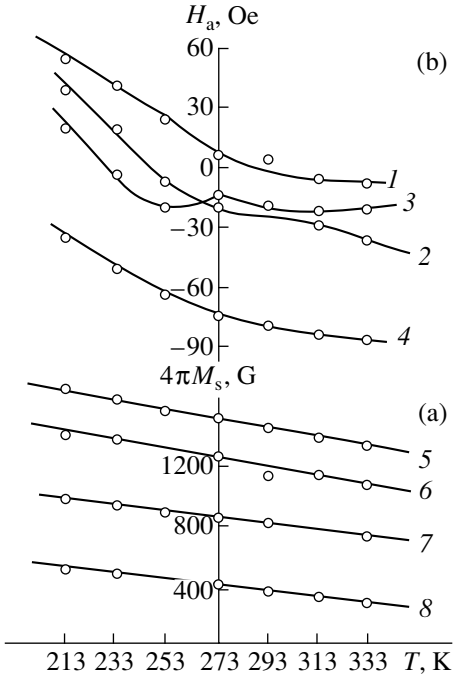

Fig. 1. Temperature variation of (a) the saturation magnetization $4\pi M_s$ and (b) the anisotropic field H_a for a series of epitaxial $Y_{3-y}La_yFe_{5-x}Ga_xO_{12}$ films: (*2*, *5*) $x = 0.17$, $y = 0.033$; (*3*, *6*) $x = 0.41$, $y = 0.060$; (*1*, *7*) $x = 0.57$, $y = 0.090$; (*4*, *8*) $x = 0.94$, $y = 0.161$.

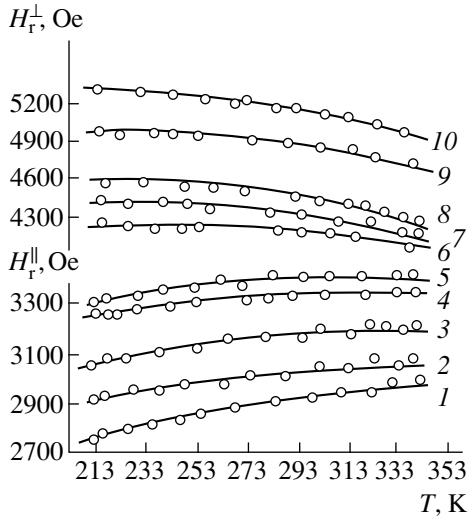

Fig. 2. The plots of resonance field values $H_r^\parallel$ and $H_r^\perp$ versus temperature for $Y_{3-y}La_yFe_{5-x}Ga_xO_{12}$ films: (*1*, *10*) $x = 0.17$, $y = 0.033$; (*2*, *9*) $x = 0.41$, $y = 0.060$; (*3*, *8*) $x = 0.57$, $y = 0.090$; (*4*, *7*) $x = 0.70$, $y = 0.098$; (*5*, *6*) $x = 0.94$, $y = 0.161$.

gallium, iron, yttrium, and lanthanum in the film (f) and solution melt (m), respectively. Note that the coefficient K_{La} only slightly depends on the charge composition and is close to a mean value of 0.22, while the K_{Ga} value for small x differs rather significantly (see table) from published data (1.6–2.0 [5]).

Figure 1 shows the temperature variation of the saturation magnetization $4\pi M_s$ and the anisotropic field H_a for a series of epitaxial $Y_{3-y}La_yFe_{5-x}Ga_xO_{12}$ films. As seen from Fig. 1a, an increase in the content of La^{3+} and Ga^{3+} ions in the substituted IYG films is accompanied by a decrease in the saturation magnetization value and by a change in the character of this variation: the slope decreases from 2.7 G/K for curve *5* ($x = 0.17$, $y = 0.033$) to 1.1 G/K for curve *8* ($x = 0.94$, $y = 0.161$).

As seen from Fig. 1b, the slope of the plots of H_a versus temperature also decreases with an increasing content of La^{3+} and Ga^{3+} ions in the entire temperature range studied. For sufficiently large degrees of substitution x and y, the H_a values become negative (curve *4*).

Figure 2 presents the plots of resonance field values versus temperature for the $Y_{3-x}La_yFe_{5-x}Ga_xO_{12}$ films measured under the parallel ($H_r^\parallel$) and perpendicular ($H_r^\perp$) resonance conditions, whereby the constant magnetic field is oriented tangentially or normally to the IYG film plane. As seen from Fig. 2, the slopes of $H_r^\parallel(T)$ and $H_r^\perp(T)$ decrease with increasing content of La^{3+} and Ga^{3+} ions. It should be noted that the IYG:(La,Ga) films exhibit a higher temperature stability of the resonance fields in comparison with the IYG:Ga films [1]. For the perpendicular resonance, a temperature drift of the resonance field is 3.2 Oe/K for pure IYG, 1.4 Oe/K for IYG:Ga ($x = 0.63$), and 0.7 Oe/K for IYG:(La,Ga) ($x = 0.94$, $y = 0.161$).

The IYG:(La,Ga) films with $x = 0.17$ and $y = 0.033$ showed a minimum value of the ferromagnetic resonance line width: $\Delta H = 0.4$ Oe. For the IYG:(La,Ga) film with $x = 0.94$ and $y = 0.161$, the resonance linewidth ($\Delta H = 0.5$ Oe) was the same as that for undoped IYG of an equal thickness. Therefore, introduction of the nonmagnetic La^{3+} and Ga^{3+} ions into the IYG film structure markedly increases thermal stability of the main characteristics of these epitaxial garnet films without significant increase in the ferromagnetic resonance line width.

REFERENCES

1. S. I. Yushchuk, P. S. Kostyuk, and I. E. Lopatinskiĭ, Zh. Tekh. Fiz. **68** (9), 46 (1998) [Tech. Phys. **43**, 1051 (1998)].
2. S. L. Blank and J. W. Nielson, J. Cryst. Growth **17**, 302 (1972).
3. S. I. Yushchuk, S. A. Yur'ev, and P. S. Kostyuk, Neorg. Mater. **33** (7), 881 (1997).
4. A. M. Balbashov and A. Ya. Chervonenkis, *Magnetic Materials for Microelectronics* (Énergiya, Moscow, 1979), p. 159.
5. A. H. Eschenferder, *Magnetic Bubble Technology* (Springer-Verlag, Berlin, 1980; Mir, Moscow, 1983).

Translated by P. Pozdeev

Technical Physics Letters, Vol. 27, No. 2, 2001, pp. 112–113. Translated from Pis'ma v Zhurnal Tekhnicheskoĭ Fiziki, Vol. 27, No. 3, 2001, pp. 54–58.

Measuring the Parameters of Photorefractive Crystals by an Electrooptical Compensation Method

A. V. Ilinskii* and E. B. Shadrin**

** Benemerita Universidad Autonoma de Puebla, México City, México*

*** Ioffe Physicotechnical Institute, Russian Academy of Sciences, St. Petersburg, 194021 Russia*

Received August 21, 2000

Abstract—A new compensation method, based on the longitudinal electrooptical effect in a modified Pockels cell accommodating two crystal plates instead of a single plate, is proposed for measuring the parameters of photorefractive crystals. The plates are oriented so that their surfaces are perpendicular to the optical axis and the long semiaxes of the electric-field-induced birefringence ellipsoids are rotated 90° relative to one another around this axis. The proposed method was used to measure the Maxwell relaxation time in the $Bi_{12}SiO_{20}$:Al crystal (0.2% Al) as a function of the photoexcitation intensity I_{ex} in the green-blue spectral region (λ = 5145 Å). For I_{ex} = 10 mW/cm^2, the Maxwell relaxation time decreases by 6 ± 1 s as compared to the dark value (80 ± 10 s). © *2001 MAIK "Nauka/Interperiodica".*

Study of the optical, electrical, and electrooptical properties of crystals is of large importance for their numerous applications [1]. The electrooptical crystals are used as active media in light modulators and deflectors; photorefractive crystals are employed in active elements of the spatial and temporal light intensity modulators, holographic recording media, etc. The mutually related electrical and optical properties of these materials depend on the method of crystal growth, degree of doping with controlled and uncontrolled impurities, and (even for the same material) on the experimental conditions (temperature, photoexcitation, etc.). An important (sometimes decisive) role belongs to the charge transfer phenomena. Using conventional electric techniques for the experimental investigation of these processes in photorefractive crystals is very difficult and sometimes even impossible because of extremely small values of currents passing in these systems.

New possibilities in this respect are offered by the electrooptical methods [1–3] based on the longitudinal or transverse electrooptical effect (Pockels effect). These measurements allow for the direct determination of the electric field and, hence, of the electric charge accumulated in a crystal studied for a long time as a result of the charge transfer by free carriers. Since the total time of the charge accumulation may be very large (from a few minutes to several hours), the electrooptical methods of charge transfer in crystals can be very effective.

We propose a new original compensation method for measuring the properties of photorefractive crystals. The technique is based on the longitudinal electrooptical effect in a modified Pockels cell accommodating two crystal plates instead of a single plate (see the figure). The plates are oriented so that their surfaces are perpendicular to the optical axis and the long semiaxes of the electric-field-induced birefringence ellipsoids are rotated 90° relative to one another around this axis. Thus, the idea is that the same crystal, appropriately oriented, is used as a compensator of the electric-field-induced birefringence instead of a quartz wedge or a mica plate employed for this purpose in the conventional compensation schemes [4].

Note that the magnitude of the longitudinal Pockels effect is proportional to the voltage applied to the sam-

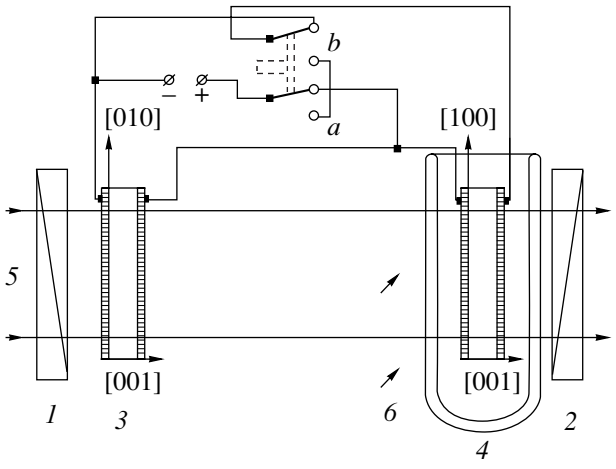

A schematic diagram of the modified Pockels cell with two spatially separated electrooptical plates of Al-doped $Bi_{12}SiO_{20}$: (*1*) polarizer; (*2*) analyzer; (*3*, *4*) oriented crystal plates; (*5*) probing light beam; (*6*) additional photoexcitation of one plate. The system can be operated in two variants, with an external voltage applied to the cell with (*a*) serial and (*b*) parallel connection of the plates.

1063-7850/01/2702-0112$21.00 © 2001 MAIK "Nauka/Interperiodica"

ple. Both this voltage and proportionality coefficient (i.e., electrooptical constants of the material) may vary under the action of external factors.

The proposed compensation method can be implemented in various modes, which in fact reduce to two principal schemes (see the figure: the switch in positions *a* or *b*). In variant *a*, the voltage is applied to the crystal plates of *equal* thicknesses connected in series. The phase difference between the ordinary and extraordinary rays, induced by the applied field, is compensated by the orthogonal orientation of the long semiaxis of the induced birefringence ellipsoid of the second plate relative to the first one. In variant *b*, the voltage is applied to the crystal plates of *arbitrary* thicknesses in parallel connection. Here, the phase difference between the two rays is compensated by applying the voltage in opposite polarity to the plates having the same orientation.

In the proposed scheme, the two crystal plates form an optical bridge with the longitudinal electrooptical effect in the first plate is compensated with high precision by the same effect (with opposite sign) in the second plate. This "zero," like any other compensation method [4], is highly sensitive to the measured value and allows both large and very small (fractions of a percent) differences between the electrooptical properties of the two pates (controlled by the different external conditions) to be reliably determined.

It should be emphasized that the spatial separation of shoulders in the optical bridge, with two spaced crystal plates placed between four transparent electrodes on the optical axis in the path of the probing light beam, allows one of the shoulders to be subjected to the action of some external factor. This can be heating or cooling of a sample crystal plate, additional photoexcitation, mechanical deformation, or any other factor capable of changing the electrooptical properties of the plate.

Now let us consider what types of physical information are provided by the electrooptical measurements in the two modes described above. In variant *a*, we measure small differences in *charge transfer parameters* between the two plates connected in series, which are revealed as a result of redistribution of the voltage drop across the plates with time. Should one of the plates differ in electric properties (due to the Maxwell relaxation time variation caused by doping, photoexcitation, temperature variation, etc.) from another, the difference can be detected with a high precision (exceeding the usual level). The gain is explained, as in any other bridge circuit [5], by a considerable decrease in the contribution of electric noise to the measured signal. In variant *b*, we determine small differences in *electrooptical coefficients* of the two crystal plates, which can be related to heating or cooling, additional doping of one plate, or the electric-field-induced variation of the electrooptical coefficient (related, e.g., to an inhomogeneous field distribution in the photoexcited sample).

The proposed method can be illustrated by the results of measurements of a small decrease ($\Delta\tau_M = 6 \pm 1$ s) in the Maxwell relaxation time ($\Delta\tau_M = 80 \pm 10$ s) of an aluminum-doped (0.2% Al) high-resistivity ($r = 2 \times 10^{13}$ Ω cm) $Bi_{12}SiO_{20}$ plate. This decrease in $\Delta\tau_M$ was related to an additional photoexcitation of the plate by light in the green-blue spectral region ($\lambda = 5145$ Å) at an intensity of $I_{ex} = 10$ mW/cm^2. The measurements were carried out using variant *a* (see figure). It should be noted that this small (about 7%) change in the parameter M, which is intrinsically measured at an accuracy not better than 12%, clearly illustrates an advantage of the compensation technique described above.

The proposed "zero" method is applicable to all cases of the induced birefringence. Indeed, the electrooptical effect under consideration leads to the appearance of a phase difference between the ordinary and extraordinary rays, caused by the action of some external factor (e.g., applied electric field). This implies the possibility of compensating for this phase shift using an identical sample with the orthogonal orientation. An additional factor (illumination, heating, pressure, etc.) acting upon the compensator introduces a disbalance into the optical bridge, which allows us to measure the response signal, thus monitoring fine details in the evolution of optical parameters of the crystals studied.

REFERENCES

1. M. P. Petrov, S. I. Stepanov, and A. V. Khomenko, *Photorefractive Crystals in Coherent Optical Systems* (Springer-Verlag, Berlin, 1991).
2. V. N. Astratov, A. S. Furman, and A. V. Ilinski, in *Semiconductors and Insulators: Optical and Spectroscopic Research*, Ed. by Yu. I. Koptev (New York, 1992), p. 271.
3. A. V. Ilinskii, I. Velázquez-Cruz, T. A. Prutskij, *et al.*, in *Proceedings of the II International Workshop "Optoelectronic Materials and Their Applications (Including Solar Cells)," La Habana, Cuba, 1998*, p. 314.
4. M. Born and E. Wolf, *Principles of Optics* (Pergamon, Oxford, 1969; Nauka, Moscow 1973).
5. G. Ya. Mirskiĭ, *Radioelectronic Measurements* (Moscow, 1975).

Translated by P. Pozdeev

Technical Physics Letters, Vol. 27, No. 2, 2001, pp. 114–117. Translated from Pis'ma v Zhurnal Tekhnicheskoĭ Fiziki, Vol. 27, No. 3, 2001, pp. 59–66.

Subnanometer Resolution in Depth Profiling Using Glancing Auger Electrons

M. N. Drozdov, V. M. Danil'tsev, Yu. N. Drozdov, O. I. Khrykin, and V. I. Shashkin

Institute of Microstructure Physics, Russian Academy of Sciences, Nizhni Novgorod, Russia

Received July 20, 2000

Abstract—A new method for Auger depth profiling, employing a difference in the escape depth of the Auger electrons emitted at nearly normal and glancing angles, is proposed and verified. The depth profiles obtained under optimum ion sputtering conditions with registration of the glancing Auger electrons exhibit a subnanometer (0.8 nm) depth resolution. This technique was successfully applied to the study of high-quality $In_xGa_{1-x}As/GaAs$ heterostructures with quantum wells grown by the method of metalorganic chemical vapor deposition. *© 2001 MAIK "Nauka/Interperiodica".*

Introduction. Since the beginning of the 1990s, specialists in the depth profiling analysis by means of Auger electron spectroscopy (AES) have been using the concept of "high-resolution Auger depth profiling" [1]. Quantitatively, this concept implies the obtaining of stable profiles with a depth resolution of 1–2 nm. However, some results on this resolution level were obtained even in the 1980s and late 1970s [1–4]. In our opinion, it is very important to develop a clear systematization of the different types of errors determining the depth resolution in profile analysis and provide for their clear identification under particular experimental conditions. This would allow reaching a depth resolution determined only by fundamental limitations—the information yield (electron escape) depth L_e and the artifacts of interaction between sputtering ions and solid surface in the ion collision cascade L_i—but free of the instrumental errors and uncertainties related to the sample properties.

Considerable success was reached in minimizing the ion sputtering artifacts, which was provided by reducing the energy of sputtering ions (to several hundreds of eV), by varying the angle of ion incidence onto the surface and by using ions with different masses. In some cases, the depth resolution reached a level of 1–1.2 nm, where the contributions of L_e and L_i are difficult to separate [1, 2]. This uncertainty can be resolved to a certain extent in the case of elements possessing both low- and high-energy Auger electron transitions by depth profiling using signals due the Auger transitions of both types [5–8]. However, many practically important elements possess either a single sufficiently intensive Auger line or several such lines with rather close energies.

At the same time, the information yield depth L_e can be varied by changing the take-off angle α of the Auger electrons escaping from the sample:

$$L_e = \lambda_e \cos\alpha, \quad (1)$$

where λ_e is the mean free path of electrons determined by the inelastic scattering and the electron escape angle α is measured from the normal to the sample surface. In this way, a nondestructive depth profiling can be performed using a special spectrometer with rotating energy analyzer [4]. However, since the depth of analysis in this case is very small (being restricted to a sample layer with a thickness of a few λ_e), this technique did not find wide application. However, the concept of varying the information yield depth by this means can be used in combination with the usual depth profile analysis employing ion sputtering. To our knowledge, this variant of depth profiling was not previously considered.

The possibility of controlled variation of the L_e in the course of depth profiling and the use of several different λ_e values for any element may increase the amount of information concerning the depth resolution function. Using glancing Auger electrons for the analysis, we may additionally increase the depth resolution and even reach a level below 1 nm, provided that the optimum ion sputtering conditions are selected. The purpose of this investigation was to implement the method of depth profiling described above and use this technique for studying the elemental composition of $In_xGa_{1-x}As/GaAs$ heterostructures.

Experiment. The experiments were performed on $GaAs/In_xGa_{1-x}As/GaAs$ heterostructures grown by the method of metalorganic chemical vapor deposition (MOCVD). The thickness of pseudoamorphous $In_xGa_{1-x}As$ layers varied from 5 to 10 nm and the x value, from 0.06 to 0.12. The 50- to 100-nm-thick GaAs films grown above the $In_xGa_{1-x}As$ layers allowed the photoluminescence of separate quantum

1063-7850/01/2702-0114$21.00 © 2001 MAIK "Nauka/Interperiodica"

wells in $In_xGa_{1-x}As$ to be studied. The sample surface roughness (by data of the atomic force microscopy) did not exceed 1–1.5 nm; the same roughness level was retained in the etch crater over the entire depth range up to 0.1 μm.

The depth profiling was performed in an ESO-3 Auger electron spectrometer with a single-path energy analyzer of the cylindrical mirror type (CMA). The depth profiling procedure is described in detail elsewhere [9, 10]. The sputtering velocity and the elemental sensitivity factors were evaluated using specially prepared multilayer $In_xGa_{1-x}As/GaAs$ heterostructures preliminarily tested by X-ray diffraction (DRON-4 diffractometer) and by conventional AES depth profiling [9]. The depth resolution for In was 1.2–1.4 nm and was retained up to a depth of 0.1 μm.

The electron take-off angle diagram of the CMA represents a ring confined between two cones with a vertex at the CMA focus and the sold angle between the side surface and the axis $\theta = \theta_0 \pm 6°$, where $\theta_0 = 42.3°$ (Fig. 1). The escape angle of Auger electrons relative to the sample surface normal **n**, which is different in various regions of the take-off angle diagram, is conveniently characterized by an average value $\langle\cos\alpha\rangle$ for each particular angular region. Of curse, this value provides only a rough estimate for L_e because the distribution function of the Auger electron emission strongly depends on the angle. We have employed the most widely used 60° holder, for which the CMA axis makes an angle of 30° with the sample surface. As was demonstrated in [4], the maximum ratio $\cos\alpha_{min}/\cos\alpha_{max}$ for this configuration with a narrow rotating slit CMA diaphragm exceeds 3.

The experiments with angle-resolved Auger electron analysis were performed on a standard Auger spectrometer with some special modifications. The two half-ring diaphragms, mounted directly on the sample holder, covered either the upper or lower half of the entire take-off region not interfering with the incident ion beam. This is possible due to a high-precision sample positioning in the spectrometer chamber, whereby the point of analysis was matched with the CMA focus by measuring the peak of elastically scattered electrons [11]. It can readily be shown that the upper half of the Auger electron take-off region (normal escape) is characterized by $\langle\cos\alpha\rangle \approx 0.85$, while the lower half (glancing escape) has $\langle\cos\alpha\rangle \approx 0.43$. For the whole take-off angle diagram, $\langle\cos\alpha\rangle = 0.64$ in agreement with [4]. Thus, by separately using these parts of the take-off angle diagram we may vary the information yield depth L_e by a factor of 2. In contrast to case of using several Auger electron lines for one element, the angular-dispersive depth profiling was carried out by repeating the measurements several times with each diaphragm.

Results. Figure 2 shows the results of the AES depth profiling of a typical $In_xGa_{1-x}As/GaAs$ (H128) heterostructure. In this sample, the $In_xGa_{1-x}As$ layer with

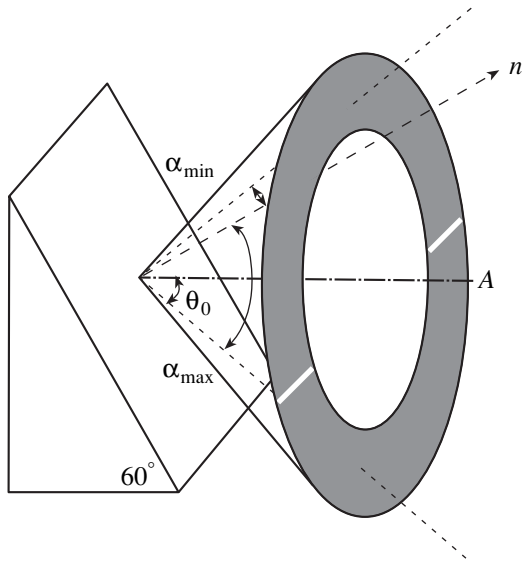

Fig. 1. The electron take-off angle geometry (relative to the sample surface) for a cylindrical mirror analyzer (CMA) in a 60°-holder (*A* is the CMA axis).

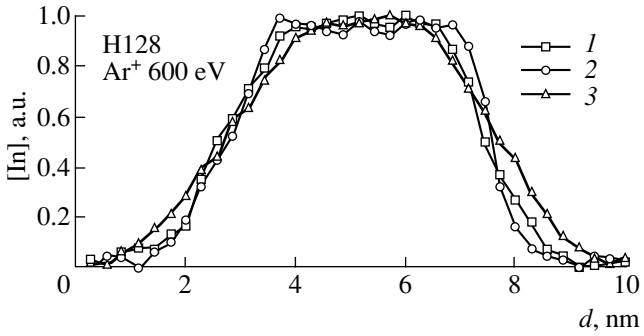

Fig. 2. Normalized depth profiles of In for a typical $In_xGa_{1-x}As/GaAs$ (H128) heterostructure measured using three different electron take-off modes: (*1*) total take-off (360°); (*2*) "glancing" electrons; (*3*) "normal" electrons.

$x \approx 0.08$ and a thickness of 5 nm occurred at a depth of about 90 nm. According to the method described in [9], the layer analysis down to a depth of 82–85 nm was performed at a high sputtering rate ($S_1 = 3.5$ nm/min) using an Ar^+ beam energy of $E_1 = 2$ keV. The region of the quantum well was analyzed using Ar^+ ions of lower energy $E_2 = 0.6$ keV at a much lower sputtering rate of $S_2 = 0.4$ nm/min. The latter part of the profile is presented in Fig. 2. For convenience, curves *1–3* are normalized to unity (in fact, the signal intensity in the upper region is about two times that in the lower region, in accordance with the angular distribution function of the Auger electron emission).

The values of the transition widths (on the 0.2–0.8 maximum height level) for the leading edge (ΔZ_1) and the trailing edge (ΔZ_2) for all three profiles depicted in

The widths of transition regions on the (0.2–0.8)I_{max} level in the Auger depth profiles of the $In_xGa_{1-x}As/GaAs$ heterostructure measured in three different electron take-off modes

Transition width at (0.2–0.8)I_{max}	1 Total take-off (360°)	2 "Glancing" electrons	3 "Normal" electrons
ΔZ_1, nm	1.4	1.2–1.4	1.6
ΔZ_2, nm	1.1–1.2	0.8	1.4

Fig. 2 are given in the table. As seen, variation of the L_e value leads to a significant difference in curves *1–3* (Fig. 2), which is analogous to the behavior observed for the Si and Al profiles measured using the high- and low-energy Auger electrons [6–8]. Note, however, that our depth profiles, which were obtained separately for each diaphragm, reflect only a broadening of the individual profiles; a shift of the profiles related to different yield depths L_e of the Auger electrons [6–8] was not determined for our structure with a deep-lying $In_xGa_{1-x}As$ layer.

Discussion. First, it should be noted that the trailing edge of the depth profiles varies depending on the electron take-off conditions more significantly than the leading edge. For the glancing electrons, the trailing edge width is 0.8 nm. To our knowledge, this resolution in depth profiling of the $In_xGa_{1-x}As$ structures has now been obtained for the first time. Naturally, the asymmetry of the profile shape is more pronounced for the glancing Auger electrons that are capable of a higher depth resolution. In contrast to the "high-resolution" Auger depth profiles exhibiting extended trailing edge, we observe the opposite situation, with an ultimately narrow trailing edge and broader leading edge. This shape of the depth profile, at such a high resolution level, is also reported for the first time.

At present, we cannot provide a final explanation for the observed profile asymmetry. In our opinion, this shape can be related either to some special features of In segregation in the course of epitaxial growth of the $In_xGa_{1-x}As$ heterostructures (an analogous effect was reported in [12]) or to some ion-sputter depth-profiling artifacts. The latter are related to a combination of the ion-induced segregation, diffusion, and preferential sputtering of In [13, 14]. We are planning additional investigations in order to elucidate this question.

An analysis of the $\Delta Z_2^{(1-3)}$ values provides sufficient information that allows us to judge on the physical mechanism determining the depth resolution in the trailing edge of the Auger depth profile. According to [15], we may use λ_e = 1 nm for the inelastic mean free path of Auger electrons corresponding to the In (408 eV) line. Assuming a Gaussian shape of the resolution function and the independent contributions of various broadening factors to the resulting profile, we obtain an estimate L_i = 0.6–0.7 nm. This value is close to the projected range of Ar^+ ions with an energy of 0.6 keV but is markedly smaller than the characteristic length of the ion-stimulated diffusion (L_D > 2 nm) observed in AlGaAs heterostructures [7, 8]. Therefore, we may ascertain that, in the ion sputtering regime employed, the trailing front of the In depth profile is determined by the mechanism of ion mixing in the atomic collision cascade.

Conclusion. Thus, we have proposed and implemented a new method of the Auger depth profiling, which makes it possible to obtain the elemental profiles for different information yield depths using a single Auger line. The depth profiling with the glancing Auger electrons allowed a subnanometer depth resolution (0.8 nm) to be reached for a $In_xGa_{1-x}As/GaAs$ heterostructure. This resolution level is determined by the ion mixing in the atomic collision cascades. For the glancing Auger electrons corresponding to low-energy transitions, the information yield depth during the Auger profiling does not exceed 0.5 nm, which is close to the level offered by the low-energy ion scattering (LEIS) spectroscopy.

Additional information about the depth resolution function, obtained using several L_e values, can be used for identification of the depth profiling errors. At the same time, these data fully conform to the mathematical apparatus developed [5] for the restoration of true profiles from the results of AES measurements using different Auger lines for the same element. We have realized the case of the information yield depths differing by a factor of 2, although this ratio can be readily increased to 3 by using narrower electron take-off sectors (at the expense of some decrease in sensitivity).

Acknowledgments. This study was supported by the Russian Foundation for Basic Research (project nos. 99-02-18037 and 00-02-16141) and by the Federal Program "Surface Atomic Structures."

REFERENCES

1. S. Hofmann, J. Vac. Sci. Technol. A **9** (3), 1466 (1991).
2. H. J. Mathieu, in *Topics in Current Physics*, Vol. 37: *Thin Film and Depth Profile Analysis* (Springer-Verlag, Berlin, 1984).
3. S. Hofmann and J. M. Sanz, in *Topics in Current Physics*, Vol. 37: *Thin Film and Depth Profile Analysis* (Springer-Verlag, Berlin, 1984).
4. S. Hofmann, in *Practical Surface Analysis by Auger and X-ray Photoelectron Spectroscopy*, Ed. by D. Briggs and M. P. Seah (Wiley, New York, 1983; Mir, Moscow, 1987), Chap. 4.
5. E. A. Vinogradov, I. V. Karpov, S. V. Kuchaev, and A. F. Plotnikov, Application for Invention No. 4447564/25(82816) (1988).

6. K. Wittmaack, in *Topics in Applied Physics*, Vol. 64: *Sputtering by Particle Bombardment III*, Ed. by R. Bahrisch and K. Wittmaack (Springer-Verlag, Berlin, 1991).
7. S. Hofmann, Sufr. Interface Anal. **21**, 673 (1994).
8. H.-I. Lee, R. Shimizu, M. Inoue, *et al.*, Jpn. J. Appl. Phys., Part 1 **35** (4A), 2271 (1996).
9. M. N. Drozdov, V. M. Danil'tsev, Yu. N. Drozdov, *et al.*, Pis'ma Zh. Tekh. Fiz. **22** (18), 61 (1996) [Tech. Phys. Lett. **22**, 761 (1996)].
10. M. N. Drozdov, V. M. Danil'tsev, N. N. Salashchenko, *et al.*, Pis'ma Zh. Tekh. Fiz. **21** (18), 1 (1995) [Tech. Phys. Lett. **21**, 725 (1995)].
11. M. T. Anthony, in *Practical Surface Analysis by Auger and X-ray Photoelectron Spectroscopy*, Ed. by D. Briggs and M. P. Seah (Wiley, New York, 1983; Mir, Moscow, 1987), Suppl. 1.
12. D. Y. Lin, Y. S. Huang, K. K. Tiong, *et al.*, Semicond. Sci. Technol. **14**, 103 (1999).
13. N. Q. Lam, Surf. Interface Anal. **12**, 65 (1988).
14. R. Kelly, Surf. Interface Anal. **7** (1), 1 (1985).
15. M. P. Seah, in *Practical Surface Analysis by Auger and X-ray Photoelectron Spectroscopy*, Ed. by D. Briggs and M. P. Seah (Wiley, New York, 1983; Mir, Moscow, 1987).

Translated by P. Pozdeev

Technical Physics Letters, Vol. 27, No. 2, 2001, pp. 118–120. Translated from Pis'ma v Zhurnal Tekhnicheskoĭ Fiziki, Vol. 27, No. 3, 2001, pp. 67–73.

The Spherical Stratification of Discharge in High-Molecular-Mass Gases

O. A. Nerushev, S. A. Novopashin, V. V. Radchenko, and G. I. Sukhinin

Institute of Thermal Physics, Siberian Division, Russian Academy of Sciences, Novosibirsk, Russia

Received August 2, 2000

Abstract—It is experimentally demonstrated that the spherical stratification of an electric discharge may take place in a gas phase containing high-molecular-mass additives. The process of a dissociative decomposition of the high-molecular-mass species in the course of discharge leads to the degradation of strata. © *2001 MAIK "Nauka/Interperiodica".*

The effect of stratification of a positive plasma column in a "linear" gas discharge (a typical example is offered by a discharge tube) is a well-known phenomenon. This kind of instability, observed in atomic and molecular media, may lead to the development of both running and immobile strata [1]. Previously [2], we reported on the spherical stratification of a low-pressure gas discharge, whereby stable immobile luminescent shells imbedded into each other appear around a small, positively charged central electrode. In contrast to the patterns observed in discharge tubes, the spherical system exhibited only immobile strata. In addition, the discharge passed into the stratified mode only for certain compositions of the gas phase. This work was devoted to studying the formation of spherical strata in a self-sustained gas discharge in various gases.

The experiments were performed in a steel cylindrical vacuum chamber with a height of 60 cm and a diameter of 50 cm. A steel ball electrode with a radius of 0.5 cm was situated at the center of the chamber. A positive voltage U_0 = 0–2000 V from a high-voltage source could be applied to the ball via a 24 kΩ ballast resistor. The grounded chamber walls served the second electrode (cathode). Prior to experiments, the chamber was evacuated to a residual pressure of ~1 Pa and then filled with a working gas. The chamber was also connected to a special reservoir from which the vapor of a high-molecular-mass substance could be added to the working gas. The gas pressure in the chamber was measured by a membrane pressure transducer. The experiments were conducted predominantly at pressures in the range from p = 10 to 50 Pa in pure atomic (He, Ar, Kr) and molecular (air, N_2, CO_2) gases, as well as in their mixtures with vapors of high-molecular-mass additives such as acetone (C_3H_6O), ethyl alcohol (C_2H_5OH), dimethylformamide (C_2H_7ON), and benzene (C_6H_6).

The discharge chamber was provided with windows for visually observing and photographing the discharge and taking the spectra of emission from the discharge plasma in the visible range (λ = 360–660 nm).

The discharge was initiated by applying a positive constant voltage, exceeding the breakdown threshold, to the central electrode. Upon the discharge formation, a characteristic potential difference (U_d = 500 V) was established between the central electrode and chamber walls. This voltage drop remained virtually unchanged in a broad range of variation of the discharge current (J_d = 5–80 mA); the J_d value could be controlled by changing the power supply voltage U_0.

Under certain conditions, including the gas phase composition and pressure and the discharge current, the discharge exhibited stratification. The number of strata observed in our experiments varied from one to more than ten. No stratification took place in pure inert gases in the entire range of pressures and currents studied. In the low-molecular-mass gases listed above, the positive discharge "column" could exhibit stratification, but the boundaries of the strata were strongly smeared and nonstationary. Immobile strata with sharp boundaries were observed only upon adding the vapor of some high-molecular-mass additive (of those listed above) to the gas phase. The main experimental results were obtained in a mixture of nitrogen with acetone.

The number and dimensions of strata depended on the high-molecular-mass additive content ξ, total gas pressure p, and discharge current J. A growth in the initial fraction of the additive increased the number of strata and decreased their relative radius; at the same time, the region occupied by the strata expanded. Pressure variations also affected the dimensions of strata: as the total pressure p decreased, the radius of strata increased in the inverse proportion. A decrease in the discharge current reduced both the number and the size of strata until their complete disappearance at a certain critical current J_c (this value was close to the discharge switch-off current). For a nitrogen–acetone mixture with the total pressure p = 25 Pa and the acetone fraction ξ ≈ 25%, the critical current was J_c ~ 5 mA. The radius R_e of the outermost stratum varied with the cur-

1063-7850/01/2702-0118$21.00

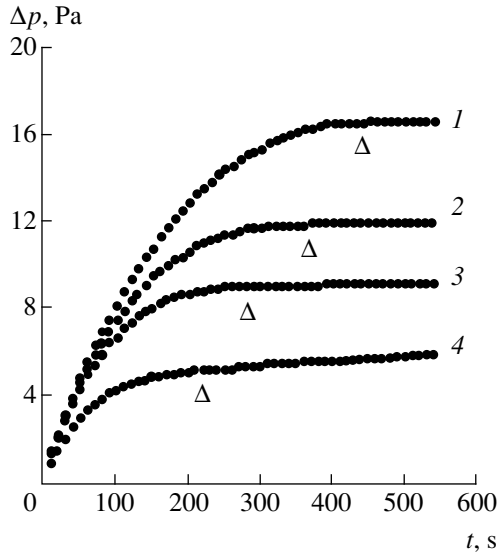

Fig. 1. The kinetics of pressure change $\Delta p = p - p_0$ in the discharge chamber for various acetone concentrations ξ in the mixture with nitrogen (p_0 = 15 Pa): ξ = 66 (*1*), 49 (*2*), 41 (*3*), 24% (*4*). Symbol Δ indicates the moment when the strata disappear.

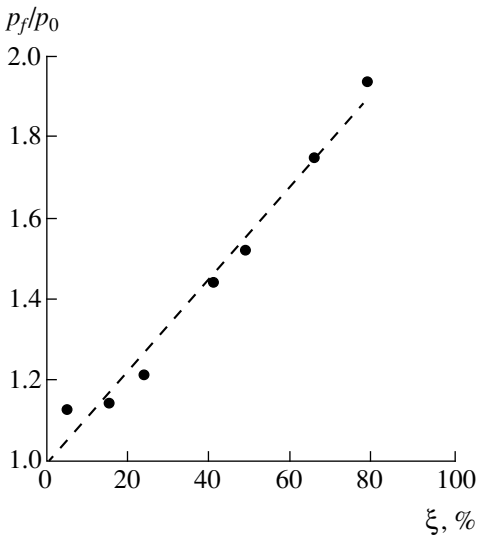

Fig. 2. The plot of relative pressure p_f/p_0 at t = 500 s versus initial acetone content ξ in the mixture with nitrogen for the initial total pressure p_0 = 15 Pa and the discharge current J = 30 mA. Points present the experimental data and the dashed line shows a linear approximation.

rent as $J_d^{1/2}$, from which it follows that the current density on this stratum is $j_e = J_d/4\pi R_e^2$ = const. For the same mixture at p = 25 Pa and $\xi \approx 50\%$, the j_e value was constant ($j_e \sim 4 \times 10^{-5}$ A/cm^2) in a broad range of the discharge current (J_d = 5–60 mA).

The gas mixtures with additives exhibited a monotonic increase in the pressure with time from the initial value p_0 to certain limiting value p_f. The pressure difference $\Delta p_f = p_f - p_0$ was proportional to the initial concentration of the high-molecular-mass component (Fig. 1). Estimates showed that this pressure variation cannot be explained by the resistive (Joule's) heating of the gas because the heat is effectively transferred to the chamber walls. Apparently, the increase in the pressure is related to a dissociative decomposition of the high-molecular-mass species as a result of the plasmachemical processes.

Figure 2 shows a plot of the relative pressure variation p_f/p_0 versus acetone content ξ in the mixture with nitrogen. As is seen from the data, the acetone molecules predominantly dissociate into two fragments. In the course of dissociation, the number of strata decreased until their complete disappearance. The moment when the discharge stratification ceases is indicated by the symbol Δ in Fig. 1.

The pressure variation was accompanied by changes in the spectrum of emission from the discharge region. Figure 3 shows the spectra of integral emission for the discharge in a nitrogen–acetone mixture measured at various time instants. As seen from Fig. 3a, the main spectral components at the initial instant are related to the vibrational transitions in N_2 molecules corresponding to the first and second positive systems ($B^3\Pi_g - A^3\Sigma_u^+$ and $C^3\Pi_u - B^3\Pi_g$, respectively) and the first negative (N_2^+) ion system ($B^2\Sigma_u^+ - X^2\Sigma_g^+$ transition). Upon

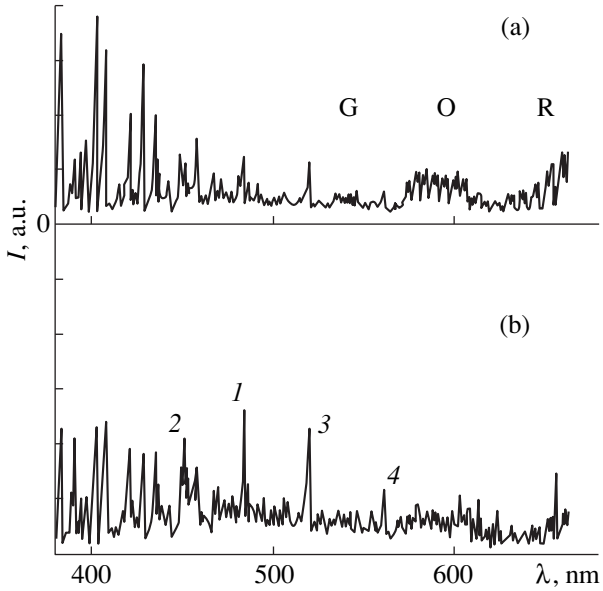

Fig. 3. The spectra of total emission from the region of discharge in a nitrogen–acetone mixture measured at t = 0 (a) and 500 s (b). The initial total pressure p_0 = 15 Pa; the discharge current J = 30 mA. Numbers at the peaks indicate the spectral lines of emission from carbon monoxide with λ = 483.6 (*1*); 451.1 (*2*); 561.0 (*3*); 608.0 nm (*4*).

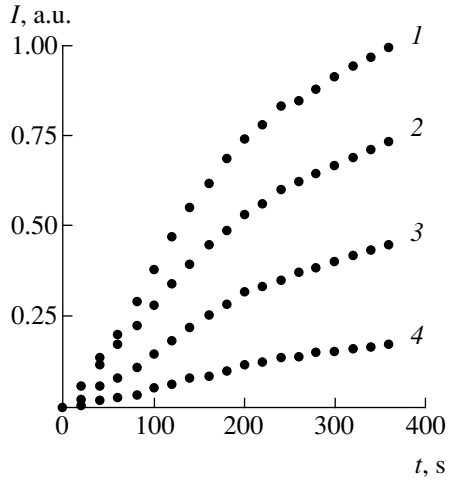

Fig. 4. Time variation of the intensity if spectral lines corresponding to the emission from carbon monoxide with λ = 483.6 (*1*); 451.1 (*2*); 561.0 (*3*); 608.0 nm (*4*). The initial total pressure p_0 = 15 Pa; the discharge current J = 30 mA; the initial acetone content in the mixture with nitrogen ξ ≈ 50%.

the elapse of $t \sim 500$ s (which corresponds to the time when the pressure reaches a plateau), the emission spectrum (Fig. 3b) has markedly changed: the nitrogen emission bands are smeared and some new bands appear. The latter correspond to the Ångström system of emission from carbon monoxide ($B^1\Sigma^+ - A^1\Pi$ transition), which was not present in the initial gas mixture. A comparison of these spectra with the barometric data suggests that carbon monoxide may form as a result of the dissociative detachment of CO groups from acetone molecules as a result of the electron impact. This is confirmed by the fact that the general character of the increase in intensity of the spectral lines of CO over the time interval under consideration (Fig. 4) is analogous to the pattern of pressure variation.

An analysis of the above data allowed us to conclude that the presence of high-molecular-mass additives is a necessary condition for the stable stratification pattern, whereas the absence or decomposition of such components (e.g., as a result of the dissociative decay induced by electron impact) implies the absence or degradation of the strata. Under experimental conditions involving the gas flow, whereby the gas medium was pertly evacuated from the discharge gap and an equivalent amount of a fresh nitrogen–acetone mixture was supplied, stable stratification could be observed for an infinitely long time. This behavior also confirms the above conclusions.

Apparently, the electron kinetics in gases containing high-molecular-mass components markedly differs from the analogous kinetics in the low-molecular-mass media. The most important processes affecting the transport characteristics of electron motions in the former case include the dissociative recombination, electron sticking, brad spectrum of energy losses, multistage processes, etc. All these effects may lead to a significant change in the macroscopic parameters of the plasma such as the electron mobility and temperature. The question as to which of these effects are decisive in the formation of spherical strata is still open and requires additional investigation.

Acknowledgments. The work was supported in parts by the Russian Foundation for Basic Research (project nos. 00-03-32428), by the "Higher Education–Fundamental Science Integration" Program of the Ministry of Education of the Russian Federation (project no. 274), and by the International Scientific-Technological Center (project no. 1425).

REFERENCES

1. P. S. Landa, N. A. Maksimova, and Yu. V. Ponomarev, Usp. Fiz. Nauk **132** (12), 601 (1980) [Sov. Phys. Usp. **23**, 813 (1980)].
2. O. A. Nerushev, S. A. Novopashin, V. V. Radchenko, *et al.*, Pis'ma Zh. Éksp. Teor. Fiz. **66** (11), 679 (1997) [JETP Lett. **66**, 711 (1997)].

Translated by P. Pozdeev

Technical Physics Letters, Vol. 27, No. 2, 2001, pp. 121–123. Translated from Pis'ma v Zhurnal Tekhnicheskoĭ Fiziki, Vol. 27, No. 3, 2001, pp. 74–78.

A Strong Electromagnetic Field Generated by a Dipole

K. A. Zheltov

Institute of Pulse Techniques, Moscow, Russia

Received July 12, 2000

Abstract—A strong electromagnetic field generated by a steep current pulse passing in a conductor dipole was measured. The current was created by an ultrashort voltage pulse formed in a coaxial transmitting line of a high-current picosecond electron accelerator. © *2001 MAIK "Nauka/Interperiodica".*

As is known [1], the dipole radiation is related to a second time derivative of the dipole momentum. By dipole, we mean a linear conductor with a length l markedly shorter than the wavelength λ of the generated electric field. Then, the second derivative of the dipole moment ql (where q is the electric charge) is essentially the first derivative (slope) of the current I flowing in the conductor:

$$d^2(ql)/dt^2 = l(dI/dt). \quad (1)$$

Accordingly, the strength E of the electric field in the direction perpendicular to the dipole at a sufficiently large distance r from it ($r \gg l$) is also described by a relationship depending on the current slope in the dipole:

$$E = \frac{\mu_0}{4\pi}\frac{l}{r}\frac{dI}{dr}, \quad (2)$$

where $\mu_0 = 4\pi \times 10^{-7}$ H/m is the magnetic permittivity of vacuum (in SI units), l [m] is the dipole length, I [A] is the current flowing in the dipole, and r [m] is the distance from dipole to the point of observation.

Using expression (1), we may estimate the current slope that is necessary to provide for a maximum electric field strength in a radiated video pulse. As a criterion, we may use the electric strength of air near the dipole (that is, the field strength at which the medium exhibits breakdown). The electric strength of an insulator strongly depends on the duration of the voltage pulse (field pulse) acting upon this insulator. A minimum duration is usually determined by the operation time of a discharge gap used in the pulse-forming device. For devices operating at megavolt potentials (e.g., transmitting lines of high-current picosecond electron accelerators [2]), an attainable pulse duration is $\sim 10^{-10}$ s, which corresponds [3] to an electric strength of air $\sim 10^7$ V/m. Assuming this value to be the admissible electric strength of air near the dipole (for $r \approx l$) and neglecting the electric field strength components proportional to r^{-2} and r^{-3}, we may estimate the necessary slope of the excitation current. According to (2), this value is $(dI/dt)_{max} \sim 10^{14}$ A/s. It is this slope of the current pulse that would provide for the generation of a strong electromagnetic field with the strength near the dipole reaching a threshold electric strength of air.

Figure 1 shows a schematic diagram of the device generating a dipole radiation. An incident voltage pulse U_{inc} with a duration of $\sim 10^{-10}$ s propagates in the coaxial line. Reaching the end of the line, where a linear conductor (i.e., the dipole, connecting the line conductors) with a length of 1.5 cm is situated, the U_{inc} pulse exhibits reflection with a change in the polarity. The voltage pulse induces an excitation (short-circuit) current I in the dipole, which is accompanied by the radiation of an electromagnetic video pulse. The excitation current is determined by the relationship

$$I = (U_{inc} - U_{ref})/Z_L, \quad (3)$$

where U_{inc} and U_{ref} are the incident and reflected voltage pulse amplitudes and Z_L is the wave resistance of the coaxial line.

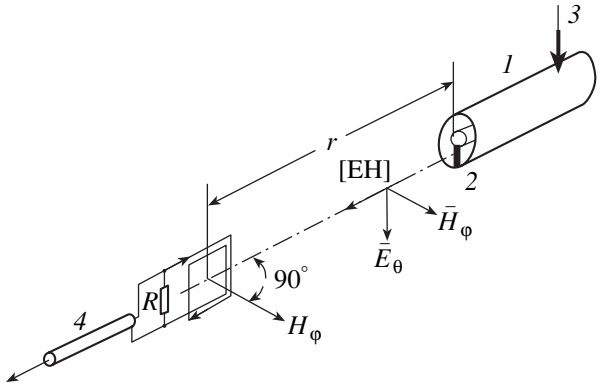

Fig. 1. A diagram showing the dipole radiator and the scheme of measurements of the electromagnetic field of a video pulse: (*1*) coaxial line; (*2*) conducting dipole; (*3*) voltage divider; (*4*) RF cable; (*R*) shunting resistor of the loop detector.

1063-7850/01/2702-0121$21.00 © 2001 MAIK "Nauka/Interperiodica"

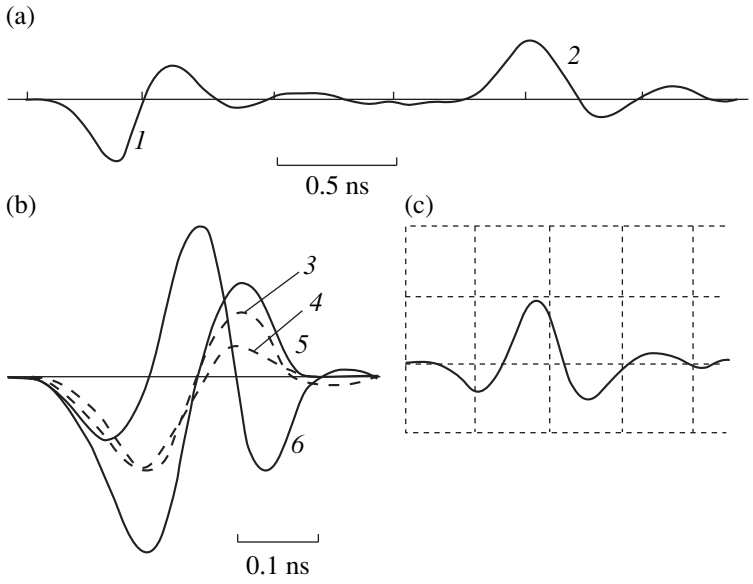

Fig. 2. Pulse shapes: (a) voltage shape in the coaxial line showing (*1*) incident and (*2*) reflected pulses; (b) current shape in the line showing (*3*) incident and (*4*) reflected pulses, (*5*) dipole current, and (*6*) current derivative; (c) radiation (video) pulse measured with the loop detector (time marks, 0.5 ns).

The electromagnetic video pulse radiated by the dipole can be registered, in principle, by two methods. First, it can be done by measuring the excitation current flowing in the dipole (and the derivative of this current). These measurements are performed with the aid of a capacitive divider *3* (Fig. 1), identical to that described in [4], which is situated near the dipole (at a distance corresponding to a distance traveled by the electromagnetic wave for ~1 ns). The incident and reflected voltage pulses, registered in the same oscillogram, determine the corresponding current pulses.

The second method consists in directly measuring the magnetic field strength H_φ near the dipole ($r \sim \lambda$) and at a sufficiently large distance from it ($r \gg \lambda$). The magnetic field was detected with a two-turn "loop" shunted by a resistor R converting the electromagnetic radiation into a voltage pulse. The loop, representing a square induction coil was oriented in the dipole plane. The loop size (~1 cm) was selected so as to be much smaller than the characteristic wavelength of the video pulse (quasistationary case). A signal measured by the loop was transmitted to an oscilloscope by an RF cable.

The shape of the electric field strength E_θ within the wave zone ($r \gg \lambda$) is identical to that of the magnetic field H_φ, the two quantities being related through the free space resistance (120π):

$$E_\theta = 120\pi H_\varphi. \quad (4)$$

Figure 2a shows the shapes of the incident and reflected voltage pulses in the coaxial line. The alternating pulse polarity is determined by features of the pulse-forming device. The maximum amplitude of the first peaks is ~350 kV. The incident and reflected current pulses of the same polarity (Fig. 2b) are superimposed in the dipole to form the excitation current pulse with an amplitude of ~13 kA. A derivative of this current shows the pulse of the radiated video pulse.

Figure 2c shows the results of direct measurements of the electromagnetic field with the aid of the loop at a distance of 2 m from the dipole. These measurements confirm the identical shapes of the video pulse and the excitation current derivative in the dipole. A somewhat longer video pulse duration is explained by a strong signal attenuation in the measuring channel The signal was transmitted via a "thin" (~1.2 mm) RF cable with a length of ~10 m and a pulse characteristic halfwidth of ~0.5 ns (comparable to the excitation current pulse duration) [5].

According to estimates, the signal attenuation in the cable is accompanied by an approximately twofold decrease in the amplitude and some increase in the pulse duration. The amplitude of the second peak in the video pulse, taking into account attenuation in the cable, is ~50 kV/m. Recalculating this value for the short-range zone (e.g., $r \approx 0.1$ m) using formula (2) yields a field strength of ≈1 MV/cm. A characteristic wavelength determined from the quasiperiod of current oscillations in the dipole is ~15 cm.

The experimental values of the current slope in the dipole and the field strength approximately correspond to the limiting values. However, we do not exclude the possibility of obtaining even higher values, since the transmitting lines of high-current picosecond electron

accelerators may in fact provide for a greater current pulse slope. This can be achieved both by increasing the incident voltage pulse amplitude and by decreasing the wave resistance of the coaxial line.

REFERENCES

1. L. D. Landau and E. M. Lifshitz, *The Classical Theory of Fields* (Fizmatiz, Moscow, 1962; Pergamon, Oxford, 1975).
2. K. A. Zheltov, *Picosecond High-Current Electron Accelerators* (Énergoatomizdat, Moscow, 1991), p. 115.
3. V. G. Shpak, M. I. Yalandin, *et al.*, Dokl. Akad. Nauk **365** (1), 50 (1999) [Dokl. Phys. **44**, 143 (1999)].
4. K. A. Zheltov, I. G. Turundaevskaya, and V. F. Shalimanov, Prib. Tekh. Éksp., No. 6, 89 (1999).
5. G. V. Glebovich and I. P. Kovalev, *Broadband Transmission Lines of Pulse Signals* (Sov. Radio, Moscow, 1973), pp. 16–21.

Translated by P. Pozdeev

Technical Physics Letters, Vol. 27, No. 2, 2001, pp. 124–126. Translated from Pis'ma v Zhurnal Tekhnicheskoĭ Fiziki, Vol. 27, No. 3, 2001, pp. 79–84.

Interferometric Study of an Elongated Element Model with Axisymmetric Streamlining for Two Mach Numbers (M = 3 and 4)

A. N. Mikhalev, A. B. Podlaskin, and V. A. Shiryaev

Ioffe Physicotechnical Institute, Russian Academy of Sciences, St. Petersburg, 194021 Russia

Received September 26, 2000

Abstract—The streamlining density fields for elongated models of explosion-formed projectiles were studied by the interference method. The character of the density profiles and their variation upon increasing the Mach number from M = 3 to 4 are considered. The analysis reveals some special features in the stabilization shock wave formation. It is shown that the proposed model shape is admissible from the standpoint of moderate aerodynamic resistance and sufficiently high stability. *© 2001 MAIK "Nauka/Interperiodica".*

Previously, we performed an interferometric investigation of the pattern of supersonic streamlining for a medium elongation model of the explosion-formed projectile (EFP) with M = 4 at the ballistic track of the Ioffe Physicotechnical Institute. The streamlining density fields were studied in the cross sections at the side generating contour, at the stabilizer skirt, and behind the bottom section of the model. An analysis of data for 7 cross sections in these zones of streamlining provided a clear pattern of the density variation in both radial and axial directions. A considerable density (pressure) jump was observed in the stabilizing shock wave. A sharp drop in the density (pressure) was observed in the depression fan behind the skirt section in the bottom part of the model. At the given Mach number, the density in the bottom region, which is constant in the radial direction and along the axis (over a certain distance), exhibits a low value. Small attack angles allowed data interpretation using the axisymmetric model because deviations were comparable with the error of measurements [1].

In this paper, we report on the EFP model with L/d = 4.4, where d is the head part diameter. The images of admissible axisymmetric character were obtained for M = 3 and 4. The data were measured and processed for a series of cross sections at a step of 0.2D (D is the skirt diameter) in the directions both toward (0.2D,0.4D, 0.6D, 0.8D, 1.0D) and away from the head in the bottom region (–0.2D, –0.4D, –0.6D). During the interferometer adjustment (with bands perpendicular to the stream axis) for ~70 bands, the cross section was divided into 30–40 zones. A hypothetical dispersion of the phase shift was taken equal to 0.07 of the band width.

Let us first consider the behavior of the streamlining density in the transverse cross sections (radial profiles) of the elongated EFP model for the Mach number M = 3. In our models, the bottom region behind the skirt with a large semiangle (~34°) is rather short, as evidenced by an increment of the paraxial bottom density values already in the –0.6D cross section below the bottom (indicative of a trace neck proximity). Another feature is the early appearance of the stabilization jump in the axial direction, which is also related to a large value of the skirt angle (Fig. 1).

A quantitative analysis of the network of radial profiles (and isolines) of the density showed a complicated flow structure. The radial density profiles in the EFP model cross sections reflected the density behavior cor-

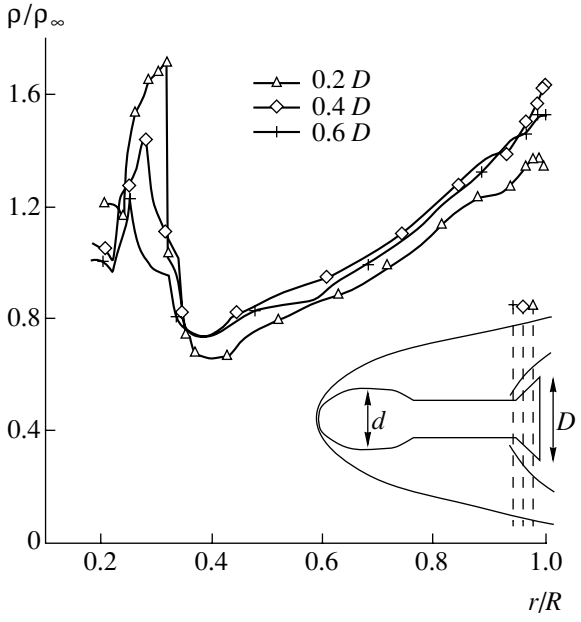

Fig. 1. Radial density profiles ρ/ρ_∞ versus r/R in the transverse cross sections of the streamlining field at the stabilizer skirt of the EFP model for M = 3.

responding to a shock-wave-streamlining character. The cross sections at the distances 1.0*D* and 0.8*D* from the bottom section toward the head part exhibited a smooth radial decrease in the density following the jump (~1.45ρ_∞) in the head shock wave. This decrease was followed by a rather sharp increase in the zone behind the moderate separation jump (essentially a weak perturbation) propagating from the break immediately behind the frontal thickening. This moderate increase in the density (~0.3) changed for a real jumplike increase in the density observed in the cross sections at 0.4*D*, 0.2*D*, and 0.0*D* crossing the region of formation of the stabilization shock wave. This is quite natural because the calculated cross sections pass through the forming (0.4*D*) and formed (0.2*D*, 0.0*D*) stabilization shock wave. The magnitude of this jump (from ρ/ρ_∞ = 0.8 to 1.70) shows its intensity to exceed that of the head shock wave in the same cross section. The coordinates and intensity of the stabilization shock wave determined the aerodynamic behavior of the elongated EFP models under consideration (Fig. 1).

The cross sections behind the bottom section of the elongated EFP models did not show significant differences from the patterns observed for the medium elongation model (L/d = 3). However, there is one feature that is worth noting. The density drop in the extended zone between the head wave and the stabilization shock wave (behind the skirt) was followed by a jumplike increase in the density in the latter shock wave. Then the density exhibited a sharp drop in the depression fan to reach a bottom value tat was virtually constant down to the axis. However, as was noted in the preliminary analysis, this bottom density value ρ/ρ_∞ markedly increased away from the head (from ρ/ρ_∞ = 0.1 at –0.2*D* to ρ/ρ_∞ = 0.3 at –0.6*D*). This is evidently explained by the formation of a short stagnation zone behind the skirt with a 34° semiangle. This stagnation zone is followed by the region of the tail shock wave formation, which is accompanied by the flow contraction in the trace neck. It is this neck contraction onset that was observed in the bottom density behavior at the –0.6*D* cross section.

The interference measurements for the elongated EFP model were performed for two values of the Mach number. The results of processing of the interferogram obtained for M = 4 revealed no principal qualitative differences in the profiles. The stabilization shock wave at the skirt becomes more pronounced and is observed near the bottom section at a relative radius of r/R = 0.35. For M = 3, the shock wave was observed n the same cross sections (0.0*D* and 0.2*D* toward the head part) at r/R = 0.25–0.30. Taking into account the convex shape of this wave, we must note that the shock wave observed for M = 4 is displaced by the stabilizer skirt to a somewhat greater relative radius r/R. However, the shock wave intensity did not increase with the Mach number, while the head wave for M = 3 is markedly less intense than that for M = 4. In the cross sections near the bottom section, ρ/ρ_∞ = 1.30 in the head wave for M = 3 and ρ/ρ_∞ = 1.55 for M = 4 (Fig. 2).

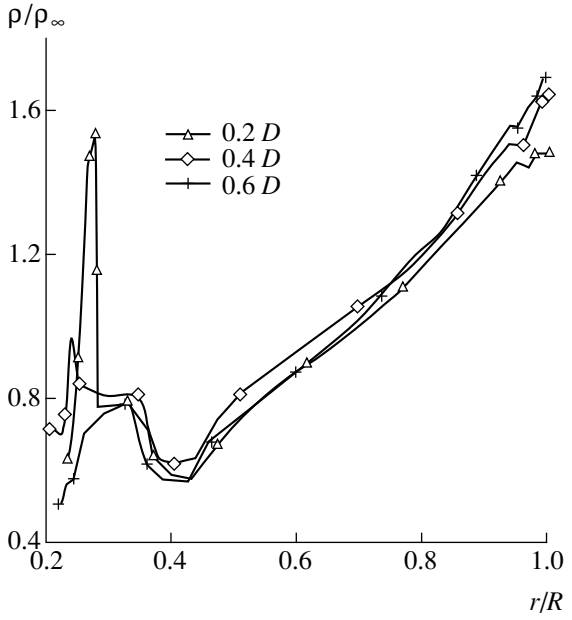

Fig. 2. Radial density profiles ρ/ρ_∞ versus r/R in the transverse cross sections of the streamlining field at the stabilizer skirt of the EFP model for M = 4.

For M = 4, the gas compressed in front of the stabilizer skirt shifted the onset of the stabilization shock wave along the axis toward the middle of the model. As a result, the stabilizing effect of the skirt was less pronounced because of a smaller shoulder of the returning force. From the standpoint of stabilization, the shock wave would better occur immediately at the skirt.

The bottom parameters observed for M = 4 exhibit no significant difference from the values obtained for the EFP model at M = 3. For M = 4, the density increased along the axis from 0.15 to 0.23ρ_∞ at –0.6*D*. This agrees with the behavior for M = 3; a relatively smaller axial growth reflects a greater size of the bottom region.

In order to obtain comparative data and exclude the random error, we have measured and processed the interferograms for the model streamlining at a small attack angle. For the maximum experimentally possible attack angle of ~5°, there was some difference in the stabilization shock wave position on the windward and leeward sides, at a very small difference in intensity. These differences leveled in the vicinity of the bottom section. In this study, the density values upon averaging between the windward and leeward sides coincided with the parameters calculated for the axisymmetric pattern.

The density profiles obtained at the side surface and behind the bottom section of the elongated EFP models qualitatively explain the features of aerodynamics observed for these forms [2]. The density distribution

during the shock wave formation and upon reaching its maximum intensity, as well as the position of the stabilization shock wave confirm correct selection of this aerodynamic shape of the element.

The presence of a short stagnation zone with a very low density (pressure) level indicates that it might be useful to increase the bottom pressure, which would reduce the total resistance. This increase can be achieved by making special cuts in the stabilizer skirt.

As estimated by comparing the series of radial profiles, the increase in the Mach number from $M = 3$ to 4 did not principally change the flow structure. However, a shift of the stabilization shock wave and the onset of this shock wave formation closer to the center of mass of the model did not lead to an increase in the stabilization. Nevertheless, the model retained its stability and resistance characteristics at the considered Mach numbers. Owing to a small diameter of the weakly blunted head part, the resistance of the model is on a moderate level. This is confirmed by the relatively small intensity of the head shock wave ($\rho/\rho_\infty = 1.60$).

The data obtained on the density of the base EFP model may be used for comparison with the results of numerical calculations of the streamlining patterns for bodies of the same class, first of all, based on the system of nonviscous Euler's equations. This is also valid for simplified calculation methods such as the Newton approach and the potential flow model.

REFERENCES

1. P. I. Kovalev, A. N. Mikhalev, A. B. Podlaskin, *et al.*, Zh. Tekh. Fiz. **69** (12), 6 (1999) [Tech. Phys. **44**, 1402 (1999)].
2. K. P. Petrov, *Aerodynamics of Rockets* (Mashinostroenie, Moscow, 1977).

Translated by P. Pozdeev

Technical Physics Letters, Vol. 27, No. 2, 2001, pp. 127–128. Translated from Pis'ma v Zhurnal Tekhnicheskoĭ Fiziki, Vol. 27, No. 3, 2001, pp. 85–88.

Foam Stabilization by Surfactants: A Fractal-Percolation Fracture Model

Yu. V. Pakharukov and T. E. Shevnina

Tyumen State University of Oil and Gas, Tyumen, Russia

Received May 15, 2000

Abstract—A theoretical model is proposed that describes the dependence of foam stability on the surfactant concentration in a foam-forming solution. The model is based on the parameters reflecting a fractal structure and percolation properties of the foam. It is established that a time corresponding to the onset of the liquid outflow from a foam column sharply increases in a certain narrow surfactant concentration interval. © *2001 MAIK "Nauka/Interperiodica".*

Foams employed in various technologies must be sufficiently stable. The strength and lifetime of a foam are determined by the properties of its skeleton, which depend on a number of conditions, in particular, on the nature and amount of surfactant. An increase in the surfactant content in a foam-forming solution leads to a decrease in the rate of descending liquid flow and an increase in the liquid efflux time. This is conventionally explained by the enhanced interaction between adsorption layers, growing mechanical strength of the walls, and increasing viscosity [1–3].

Babak *et al.* [2] studied the isotherms of the foam stability and observed an increase in the characteristic time τ^* (for which the foam column height decreased by 63%) within a certain narrow interval of the surfactant concentration. However, a change in the film strength and an increase in the viscosity were observed in a markedly wider surfactant concentration interval. This circumstance requires a more thorough investigation of the effect of a surfactant, present in the foam-forming solution, upon the foam stability.

We believe that a model describing the foam stability as depending on the surfactant concentration must be formulated so as to take into account processes reflecting the state of the whole system, rather than employing a large number of various parameters. The proposed approach can be realized within the framework of a fractal-percolation foam fracture model developed in [4], where the foam fracture process was considered using a polyhedral foam structure model. The structure represents a branched system of channels separated by nodes, with two edges (film boundaries) entering each node so as to form an angle of $\Theta = 120°$. There are 2^n edges on the nth level, the height of which is determined by the recurrent formula $h_n = h_1/2^{n-1}$, where h_1 is the first level height.

According to this model, the foam fracture develops by a scale-invariant mechanism of the load transfer by the pressure of a liquid, which breaks through the nth level to transfer the load to the adjacent $(n-1)$th level. In this case, the process of liquid percolation is conveniently represented as the walk-through nodes of a hierarchical fractal tree with the column height $H = \sum_{n=1}^{\infty} h_n = 2h_1$. In the absence of fracture, the load due to the liquid pressure on each node is P_{on}. The scatter of edge lengths, channel shapes, and film thicknesses leads to a statistical redistribution of the values of breaking loads for the nth level nodes.

Adding a surfactant results in the appearance of a certain fraction α of especially strong edges in the fractal tree. The probability ρ_n that the load exceeds the breaking level is described by the Weibull distribution [5]:

$$\rho_n = (1-\alpha)\left\{1 - \exp\left[-\left(\frac{P_n}{P_{on}}\right)^m\right]\right\} + \alpha\left\{1 - \exp\left[-\left(\frac{P_n}{\gamma P_{on}}\right)^m\right]\right\}, \quad (1)$$

where γ is the ratio of the characteristic loads of strong and weak edges, $P_n = P\cos(\Theta/2)/2^n$ is the average load on each edge of the nth level, P is the vertical load applied to the zeroth level ($n = 0$), and m is the distribution order.

Previously [4], we derived a formula for calculating the critical height (percolation threshold) of the nth level of the fractal tree. With an allowance for a change in the surfactant concentration, this formula can be written in the following form:

$$h_n = \frac{k_1\sigma(c)}{2.5 r_0 \rho g}\sqrt{K_{n+1}} - \frac{2\sigma(c)}{r_0\rho g}\left[1 - \frac{\gamma\cos\frac{\Theta}{2}}{0.48\times 2^n}\right], \quad (2)$$

where r_0 is the radius of an equivalent bubble, σ is the coefficient of surface tension, c is the surfactant con-

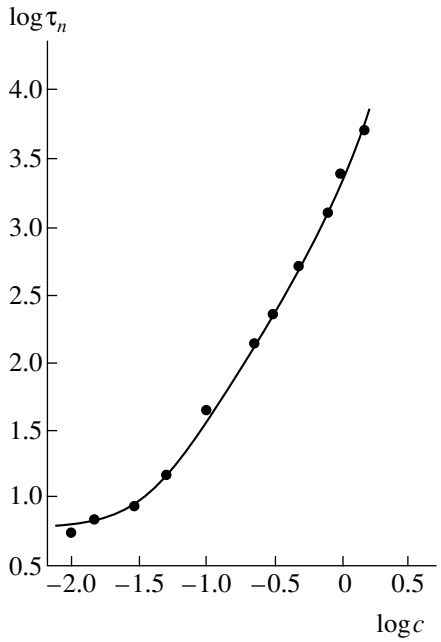

The isotherm of stability for a foam obtained from an aqueous DS–RAS solution.

centration in the foam-forming solution, k_1 is a coefficient determined by the foam structure model (for a pentagon-dodecahedral model, $k_1 = 1.53$), K_{n+1} is the foam multiplicity on the $(n + 1)$th level, ρ is the liquid density, and g is the acceleration of gravity. Some of the parameters entering into formula (2) vary with the surfactant concentration. As the surfactant concentration increases, the surface tension sharply drops until reaching a minimum level and then remains virtually constant [3]. This is accompanied by a change in the foam-forming solution viscosity and some increase in the bubble size and multiplicity. We will assume that the value of γ is proportional to a change in the solution viscosity. The results of our calculations show that a critical height of the foam column markedly increases beginning with certain critical surfactant concentration. At this critical point, the rate of increase in the γ value is higher than the rate of change in the surface tension σ.

The calculated isotherm of the foam stability (i.e., a plot of the accumulation time $\tau_n \sim \frac{1}{\rho_n}$ versus surfactant concentration c) presented in the figure corresponds to the case when all edges of the fractal tree are equally strong ($\alpha = 1$). A special feature of this isotherm is a sharp increase in the accumulation time within a rather narrow surfactant concentration region.

Thus, dependence of the foam stability on the surfactant concentration in the foam-forming solution can be studied within the framework of the proposed fractal-percolation model.

REFERENCES

1. K. B. Kann, Kolloidn. Zh. **41** (4), 667 (1979).
2. V. G. Babak, G. A. Vikhoreva, I. G. Lukina, *et al.*, Kolloidn. Zh. **59** (2), 49 (1997).
3. V. N. Izmaĭlova, S. R. Derkach, G. P. Yampol'skaya, *et al.*, Kolloidn. Zh. **59** (5), 654 (1997).
4. Yu. V. Pakharukov and T. E. Shevnina, Pis'ma Zh. Éksp. Teor. Fiz. **69** (12), 900 (1999) [JETP Lett. **69**, 954 (1999)].
5. S. Solla, in *Fractals in Physics*, Ed. by L. Pietronero and E. Tosatti (North-Holland, Amsterdam, 1986; Mir, Moscow, 1988).

Translated by P. Pozdeev

Technical Physics Letters, Vol. 27, No. 2, 2001, pp. 129–131. Translated from Pis'ma v Zhurnal Tekhnicheskoĭ Fiziki, Vol. 27, No. 3, 2001, pp. 89–94.

Electric Field Affects the Charge State in Ion-Implanted Si–SiO_2 Structures

A. P. Baraban, L. V. Miloglyadova, and V. I. Ter-Nersesyants

Institute of Physics, St. Petersburg State University, St. Petersburg, Russia

Received September 19, 2000

Abstract—Using the method of depth profiling based on the measurement of high-frequency voltage–capacitance characteristics in an electrolyte–insulator–semiconductor structure in combination with the insulator layer etching, it was found that Ar ion implantation into the oxide film of a Si–SiO_2 structure (oxide thickness, 250 nm) leads to the formation of positively charged (outer) and negatively charged (inner) layers in the SiO_2 film beginning with an implanted ion dose of 10^{14} cm^{-2}. The effect of an external electric field upon the charge state in these ion-implanted structures was studied. It was established that the negatively charged centers represent hole traps, which are recharged by the applied field to a neutral state. It is suggested that these centers are related to the appearance of nonbridging oxygen atoms as a result of the silicon oxide film reconstruction induced by the ion implantation to a dose exceeding 10^{14} cm^{-2}. © *2001 MAIK "Nauka/Interperiodica".*

Ion implantation modifies the properties of targets, including the composition of affected layers (due to the implant incorporation) and their structure (due to dissipation of the energy of ions stopped by the substance). Investigation of the effect of subsequent, less energetic actions upon the implanted structures reveals the properties of the implantation-induced defects and provides information explaining the nature of these defects and the mechanisms of their formation.

The purpose of this work was to study the properties and nature of defects formed in the course and/or as a result of the ion implantation, which are responsible for the negatively charged layer formation in the oxide film of a Si–SiO_2 structure, in the vicinity of the oxide–silicon interface.

We have studied the Si–SiO_2 structures obtained by thermal oxidation of (100)-oriented KEF-5 silicon wafers at 950°C in a wet oxygen atmosphere. The oxide film thickness was 250 nm. The oxidized silicon samples were implanted with argon ions to doses in the 10^{13}–10^{16} cm^{-2} range. The treatment was performed in an Eaton Nova Model 4206 setup on cooling the samples and using a low-density ion beam in order to avoid overheating of the targets. The ion energy (130 keV) was selected so as to provide that a maximum density of implanted ions would occur in the middle of the oxide film. The ion implantation was followed by the fast thermal annealing at a temperature of 500 or 700°C, for which purpose the samples were exposed for 10 s to radiation of a halogen lamp under nitrogen atmosphere.

The ion-implanted and annealed samples were subjected to the action of electric field in an electrolyte–insulator–semiconductor structure (with plus on silicon) at voltages below the threshold for the degradation breakdown in the structures studied. The charged state of the ion-implanted Si–SiO_2 structures was studied by a method of depth profiling that yielded the curves of flat-band potential (V_{fb}) versus oxide thickness d_{ox} (Fig. 1). These profiles contained information about the

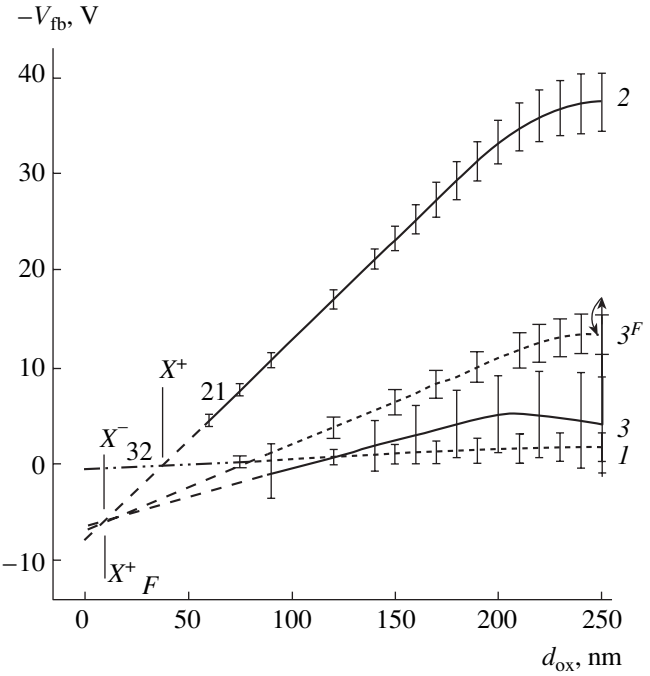

Fig. 1. The plots of flat band potential V_{fb} versus oxide layer thickness d_{ox} for the (*1*) initial and (*2*, *3*) Ar-ion-implanted Si–SiO_2 structures (oxide thickness, 250 nm): (*2*) implantation dose $D = 10^{13}$ cm^{-2}; (*3*) $D = 10^{14}$ cm^{-2}; (3^F) sample implanted to $D = 10^{14}$ cm^{-2} and exposed to the field.

1063-7850/01/2702-0129$21.00 © 2001 MAIK "Nauka/Interperiodica"

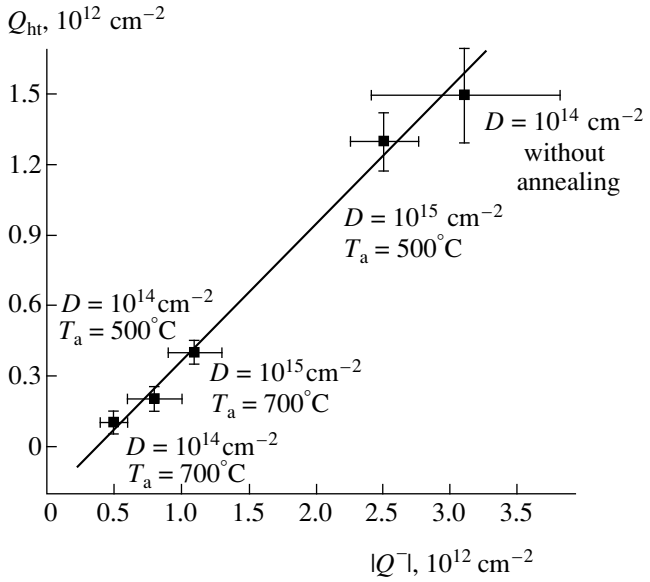

Fig. 2. The plot of positive charge, formed in the oxide film of ion-implanted Si–SiO_2 structures (oxide thickness, 250 nm) near the boundary with silicon under the electric field action, versus the negative charge formed in the same oxide region upon the ion implantation. Figures at the experimental points indicate the implanted doses D and fast thermal annealing temperatures T_a.

amount and distribution of charge implanted into the oxide film. The positions (X) of centroids of the charge localized in the oxide were determined as the depths corresponding to intersection of the $V_{fb}(d_{ox})$ plots, obtained before and after the field application, extrapolated to the zero oxide thickness. The true charge values were determined from the slopes of these profiles [1]. All measurements were performed at 293 K.

Previously [2, 3], we established that the ion implantation to a dose of $D = 10^{13}$ cm^{-2} in this system leads to the formation of a positively charged layer (with a centroid at $X = 35 \pm 5$ nm) in the oxide near the boundary with silicon. The amount of this charge did not change on increasing the implantation doze. Beginning with $D = 10^{14}$ cm^{-2}, a negatively charged layer (with a centroid at $X = 8 \pm 7$ nm) formed in addition to the positively charged one (Fig. 1). The negative charge increased with the further increase in the implantation dose [2].

The electric field action upon the unimplanted Si–SiO_2 structures and those implanted to $D = 10^{13}$ cm^{-2} did not significantly modify the charge state in the oxide at the boundary with silicon. In contrast, the exposure of the structures implanted to $D \geq 10^{14}$ cm^{-2} led to the formation of a considerable positive charge n SiO_2 at the boundary with silicon. The centroid of this positive charge always coincided with that of the negative charge observed upon ion implantation (Fig. 1). The amount of the positive charge appearing due to the field action was proportional to the initial negative charge (observed upon implantation) at all ion doses and both temperatures of the postimplantation fast thermal annealing (Fig. 2). The positive charge accumulated in the field rapidly vanished during a low-temperature annealing (T = 200°C, 30 min). The subsequent field application led again to the positive charge accumulation, which could be removed by low-temperature annealing and so on.

The coincidence of centroids of the negative charge produced in SiO_2 by the ion implantation and the positive charge induced by the field application, as well as the fact that the latter positive charge was proportional to the initial negative charge for all implantation doses and fast thermal annealing temperatures, suggested that the centers responsible for this negative charge are (in the negatively charged state) Coulomb hole traps. In the electric field, these traps are filled due to the injection of holes from Si into SiO_2.

Interaction of the energetic argon ions with the atomic subsystem of the SiO_2 matrix during the ion implantation leads to the formation of two nonstoichiometric (SiO_x) layers in the oxide film with $x > 2$ and $x < 2$ [2]. The layer enriched with oxygen ($x > 2$) is situated closer to the silicon surface because oxygen atoms exhibit greater displacements than silicon atoms as a result of interaction with the bombarding argon ions. It is the formation of these nonstoichiometric layers and the corresponding defects that are responsible for the appearance of electrically active centers during the ion implantation. In the region enriched with oxygen, where the negative charge is accumulated, the defects formed in the course and/or as a result of the ion implantation most probably have the form of nonbridging oxygen atoms ($O_3{\equiv}Si–O$). The energy levels of these defects both in the negatively charged ($O_3{\equiv}Si–O^-$) and neutral ($O_3{\equiv}Si–O^0$) states occur in the forbidden band of SiO_2 below the top of the valence band of silicon (the energy level of the $O_3{\equiv}Si–O^0$ state is 1.9 eV above the top of the valence band of SiO_2, while the $O_3{\equiv}Si–O^-$ level lies slightly above the $O_3{\equiv}Si–O^0$ level [4]).

In the negatively charged state, these defects may act as the Coulomb hole traps. Under the field action, these centers are filled by holes injected with silicon and exhibit recharge to the neutral state. Upon switching off the field and low-temperature annealing, these defects return to the negatively charged state. This recharge is apparently related to the charge exchange either with the silicon substrate (tunneling and/or hopping conductivity) or with the valence band of SiO_2. The aforementioned mutual arrangement of the energy levels of defects of the nonbridging oxygen type make these processes highly probable.

The appearance of such defects in the oxide film of the ion-implanted Si–SiO_2 structures beginning with a dose of $D = 10^{14}$ cm^{-2} can be related to certain reconstruction of the oxide layer (involving changes in the bond angles and lengths in the SiO_2 matrix) that is known to start in this very dose range.

Thus, an analysis of changes in the charge state under the field action suggests that defects responsible for the negatively charged layer formation in the ion-implanted Si–SiO_2 structures are defects of the type of nonbridging oxygen atoms.

REFERENCES

1. A. P. Baraban, V. V. Bulavinov, and P. P. Konorov, *Electronics of SiO_2 Layers on Silicon* (Leningrad. Gos. Univ., Leningrad, 1988).
2. A. P. Baraban, A. A. Kuznetsova, L. V. Malyavka, and A. V. Shishlova, Izv. Vyssh. Uchebn. Zaved., Élektron., No. 4, 17 (1998).
3. A. P. Baraban and L. V. Malyavka, Pis'ma Zh. Tekh. Fiz. **26** (4), 53 (2000) [Tech. Phys. Lett. **26**, 159 (2000)].
4. E. P. O'Reilly and J. Robertson, Phys. Rev. B **27** (6), 3780 (1983).

Translated by P. Pozdeev

Technical Physics Letters, Vol. 27, No. 2, 2001, pp. 132–133. Translated from Pis'ma v Zhurnal Tekhnicheskoĭ Fiziki, Vol. 27, No. 4, 2001, pp. 1–3.

Thermostimulated Exoelectron Emission during the Structural Transition in $Ca_{10}(PO_4)_6(OH)_2$

N. A. Zakharov, V. A. Klyuev, and V. P. Orlovskiĭ

Kurnakov Institute of General and Inorganic Chemistry, Russian Academy of Sciences, Moscow, 117907 Russia

Received July 11, 2000

Abstract—Thermostimulated exoelectron emission (TSEE) from a biocompatible calcium hydroxyapatite $Ca_{10}(PO_4)_6(OH)_2$ (CHA) was studied in a temperature range from 20 to 400°C. It was established that the structural transition in CHA is manifested by a sharp increase in the exoelectron emission intensity beginning at 200°C, followed by a peak in the TSEE spectrum. © *2001 MAIK "Nauka/Interperiodica".*

Calcium hydroxyapatite $Ca_{10}(PO_4)_6(OH)_2$ (CHA) is close in composition to the inorganic components found in the bone tissues of both animals and humans and is used as an implant material in medicine (in particular, in dentistry) [1]. The problem of the biocompatibility of the CHA based materials is interdisciplinary and requires a systematic investigation of the entire set of physicochemical properties of this compound. The purpose of this work was to study the thermostimulated exoelectron emission (TSEE) of CHA in a broad (20–400°C) temperature range.

The experiments were performed with CHA synthesized as described previously [2, 3]. The initial material was characterized by a Ca/P ratio of 1.67 and contained not less than 98% of the main compound. The CHA samples in the form of tablets for the TSEE measurements were prepared by pressing, followed by annealing at 1000°C. The TSEE properties of these samples were studied as described elsewhere [4].

The experimental results are presented in the figure. For all CHA samples in the series studied, irrespective of the conditions of synthesis, preparation (pressing and annealing), and storage, the TSEE spectra exhibited a pronounced peak with a maximum at about T_m = 300°C (curve *1*). Because of a relaxation nature of the TSEE phenomenon, a decrease in the rate q of the CHA sample heating was accompanied by a shift in position of the TSEE peak toward lower temperatures (curve *3*). A characteristic feature of the compound studied is the sharp growth in the exoelectron emission intensity at temperatures above 200°C, which was observed in all samples irrespective of the heating rate.

This characteristic feature in the TSEE behavior of the samples studied can be related to a structural phase transition in CHA at 200°C, whereby the compound structure transforms from a monoclinic ($P2_1/b$) to hexagonal ($P6_3/m$) modification. The structural transition is accompanied by anomalous variation of the thermal [5] and X-ray diffraction (curve *2*) [6] characteristics. According to [7], the transition from monoclinic to hexagonal crystal modification involves a shift of the OH groups relative to the 6_3 axis, which results in doubling of the unit cell parameter along the *b*-axis ($b = 2a$; $\gamma = 120°$; space group $P2_1/b$).

A source for the exoelectron emission can be provided, for example, by the oxoapatite vacancies $Ca_{10}(PO_4)_6O$ formed in a considerable amount as a result of the reaction [8]

$$Ca_{10}(PO_4)_6(OH)_2 = Ca_{10}(PO_4)_6O\square + H_2O$$

(□ denotes vacancies) accompanying the thermal synthesis and annealing of the CHA samples.

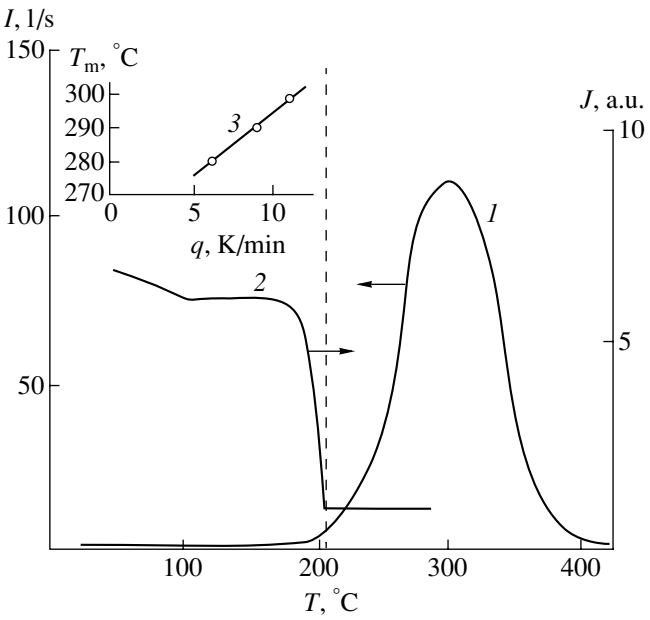

Exoelectron emission characteristics of calcium hydroxyapatite $Ca_{10}(PO_4)_6(OH)_2$: (*1*) plot of the TSEE intensity I versus temperature measured at a sample heating rate of q = 11 K/min; (*2*) plot of the X-ray diffraction intensity J at 2Θ = 35.7–37.0° versus temperature [6]; (*3*) plot of the TSEE peak temperature T_m (corresponding to the $P2_1/b \longrightarrow P6_3/m$ transition) versus the sample hating rate q.

1063-7850/01/2702-0132$21.00 © 2001 MAIK "Nauka/Interperiodica"

We believe that, owing to a high sensitivity, the above-described TSEE-based method of detecting the phase transition in CHA may be more effective in some cases as compared to the alternative methods involving thermal or X-ray diffraction measurements.

REFERENCES

1. L. L. Hench, J. Am. Ceram. Soc. **74** (7), 1487 (1991).
2. V. P. Orlovskiĭ, N. A. Zakharov, and S. M. Speranskiĭ, Zh. Neorg. Khim. **42** (9), 1273 (1997).
3. V. P. Orlovskiĭ, Zh. A. Ezhova, G. V. Rodicheva, *et al.*, Zh. Neorg. Khim. **37** (4), 881 (1992).
4. N. A. Zakharov, Yu. P. Toporov, and V. A. Klyuev, Zh. Fiz. Khim. **73** (5), 716 (1999).
5. G. A. Sharpataya, A. D. Fedoseev, V. V. Bogacheva, *et al.*, Zh. Neorg. Khim. **40** (4), 612 (1995).
6. H. Suda, M. Yashima, M. Kakihama, *et al.*, J. Phys. Chem. **99**, 6752 (1995).
7. A. M. Smolegovskiĭ, *History of the Crystal Chemistry of Phosphates* (Nauka, Moscow, 1986), pp. 49–98.
8. J. Zhahn, X. Zhang, J. Chen, *et al.*, J. Mater. Sci.: Mater. Med. **4**, 83 (1993).

Translated by P. Pozdeev

Technical Physics Letters, Vol. 27, No. 2, 2001, pp. 134–137. Translated from Pis'ma v Zhurnal Tekhnicheskoĭ Fiziki, Vol. 27, No. 4, 2001, pp. 4–11.

The Effect of Adsorption Complexes on the Electron Spectrum and Luminescence of Porous Silicon

A. A. Lisachenko and A. M. Aprelev

Institute of Physics, St. Petersburg State University, St. Petersburg, 199164 Russia

e-mail: liana@alisa.samson.spb.su

Received October 3, 2000

Abstract—Effects of the surface atomic structures on the electron spectrum and luminescent properties of porous silicon (por-Si) were studied by methods of photoluminescence spectroscopy, UV photoelectron spectroscopy, and Fourier-transform IR spectroscopy. An analysis of evolution of the por-Si characteristics in the course of thermal treatment in vacuum revealed a correlation between the photoluminescence spectrum and intensity, on the one hand, and the electron spectrum and surface atomic structure, on the other hand. The thermodesorption of adsorbate from por-Si leads to atomic rearrangements on the sample surface, which is accompanied by changes in the electron structure and, hence, in the luminescent properties of the material. © *2001 MAIK "Nauka/Interperiodica"*.

The permanent interest of researchers in investigating the luminescent properties of porous silicon (por-Si) is related to wide prospects for the application of this material. There are three active regions involved in the production of luminescence from por-Si: (a) bulk layers; (b) surface (interface) layers; and (c) oxide film covering silicon nanocrystals. At the moment, the question as to the relative contributions of these regions to the total emission yield and, hence, the problem of determining the principal emission mechanism are under discussion [1–8].

However, it is now undoubtedly established that a considerable role belongs to the surface adsorbate structures including hydride, oxyhydride, and oxide groups, molecules and radicals of the etchant decomposition products, and molecules adsorbed from the gas phase. Indeed, the thermodesorption of adsorbate from a sample surface in vacuum is accompanied by irreversible quenching of the photoluminescence (PL) from por-Si [9] and by a change in the optical properties of this material [10]. The heat treatment or illumination of a por-Si sample in oxygen also strongly modifies both the macroscopic (thermo- and photoelectron work function, surface band bending) and microscopic (spectrum of surface states near the Fermi level) physical properties [11]. However, no simple correlations between the electrical and luminescent properties of por-Si were found. This can be explained, in particular, by the insufficiently detailed characterization of this system, in particular, by the lack of data on the amount and composition of adsorbate.

The purpose of this work was to study the effect of adsorbate on the PL from por-Si and characterize the electron spectrum and atomic structure of luminescent centers on the por-Si surface by methods of photoluminescence (PL), UV photoelectron spectroscopy (UPS), and Fourier transform IR (FTIR) spectroscopy.

Experimental procedure. The samples were prepared by etching (100)-oriented *n*-Si plates with a resistivity of 100 Ω cm in various etchants. Samples of the first batch (PS1) were obtained by etching in a water–ethanol–hydrofluoric acid (1 : 2 : 1) mixture; the second batch (PS2) was prepared using an alcohol-free aqueous hydrofluoric acid (1 : 1) solution. Each sample was anodized for 5 min at 30 mA/cm^2 under continuous illumination. Then the sample was rinsed in distilled water and rapidly (within a few seconds) transferred into a spectrometer (PL, UPS, or FTIR) chamber, where ultrahigh vacuum (UHV) conditions were reached after pumping and heating the sample to 200°C. Thus, the probability of the sample surface oxidation in direct contact with the atmosphere was reduced to a minimum.

The sample luminescence was excited with the aid of a double monochromator (background scattering level, not exceeding 10^{-4}) and registered with a high-transmission monochromator of the MDR-2 type. The PL spectra were corrected for the instrument transmission function. The photoelectron (UPS) spectra were measured in an original high-transmission spectrometer (aperture angle, 34°; energy resolution $\Delta E \le 0.1$ eV) specially suited for measurements in a spectral region near the Fermi level. The IR spectra were recorded with a FTIR spectrometer. All measurements were performed *in situ* under UHV conditions at room temperature or on heating the sample to a preset stabilized temperature in the $80 < T < 450$°C interval. The experimental data were collected and processed with the aid of a Pentium II PC with an ACL8112 data interface.

1063-7850/01/2702-0134$21.00

Results and discussion. Figure 1 shows the PL spectra of por-Si samples from both PS1 and PS2 batches. The emission from freshly prepared PS1 samples (Fig. 1, dash-dot curve) can be represented as a superposition of two bands. The first component has a peak at 1.81 eV, a halfwidth of 0.4 eV, and a total area of 860 arb. units; the second component parameters are 2.27 eV, 0.34 eV, and 65 arb. units, respectively. Upon exposure of the sample to the atmosphere, the first component disappears and the second component shifts toward shorter wavelengths. The PL spectra of PS2 samples exhibit a single emission band with a peak at 1.88 eV and a halfwidth of 0.37 eV.

The UPS spectra of por-Si samples of the PS1 type display two clearly pronounced peaks at E = 4.35 and 4.05 eV and two additional features at 3.5 and 0.5 eV (Fig. 2, curve *1*). The region of filled states extends up to the Fermi level (E_F). The thermoelectron work function was φ_{th} = 3.7 eV. It should be noted that this spectrum is close to that reported previously [11]. Also in agreement with [11], the intensity and shape of the UPS spectrum changes as a result of the sample treatment at 200–450°C in vacuum or in oxygen. However, we failed to find any correlation between the PL and UPS spectra. This is probably related to the fact that the PS1 sample surface is covered by hydrocarbons (ethanol decomposition products).

In this respect, the surface of por-Si samples of the PS2 type can be considered as better characterized. Indeed, their UPS spectra (Fig. 2, curve *2*) show a single feature at E = 3.6 eV. The region of filled states extends up to E_F and the thermoelectron work function is φ_{th} = 4.0 eV. We have performed parallel measurements of the PL and UPS spectra on the same PS2 sample heated to 200, 325, 395, and 445°C in vacuum. The luminescence spectra were measured upon a 5-min heating of the sample at each preset temperature and cooling down to room temperature.

The results of these PL measurements are presented in Fig. 1. As the temperature increases, the total PL intensity drops by a factor of 1.1, 1.78, 3.45, and 45 against the initial (untreated sample) level. On the background of this drop in intensity, the PL peak slightly shifts from 1.89 to 1.88 (upon heating with pumping at 200°C) and to 1.91 eV (upon heating with pumping at 395°C). An analysis of the difference PL spectrum (obtained by subtracting the spectra measured at different temperatures) allowed the initial spectrum to be represented as a sum of two components peaked at 1.95 and 1.81 eV. As the heat-treatment temperature increases to $T \sim 325$°C, the peak at 1.95 eV decreases more rapidly than does the peak at 1.81 eV, while, at $T > 325$°C, the latter peak drops faster than the former. It is this difference in the rate of the component intensity decrease that accounts for the aforementioned shifts of the total PL peak position.

The weakly pronounced desorption-induced changes in the UPS spectra of PS2 samples were

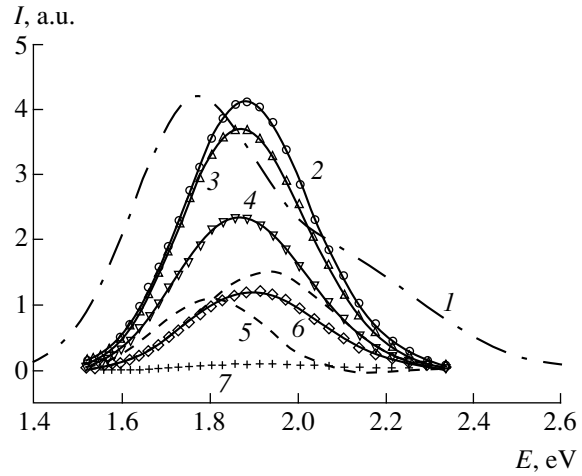

Fig. 1. Experimental photoluminescence spectra of various por-Si samples excited at λ = 337 nm (3.66 eV): (*1*) PS1; (*2*) initial PS2; (*3*) PS2 heated to 200°C; (*4*) PS2 heated to 325°C [dashed curves *5* show deconvolution of spectrum (*4*) into two Gaussian lines]; (*6*) PS2 heated to 395°C; (*7*) PS2 heated to 445°C. Symbols represent the experimental points; solid curves show the approximation of experimental plots by a sum of two Gaussian components.

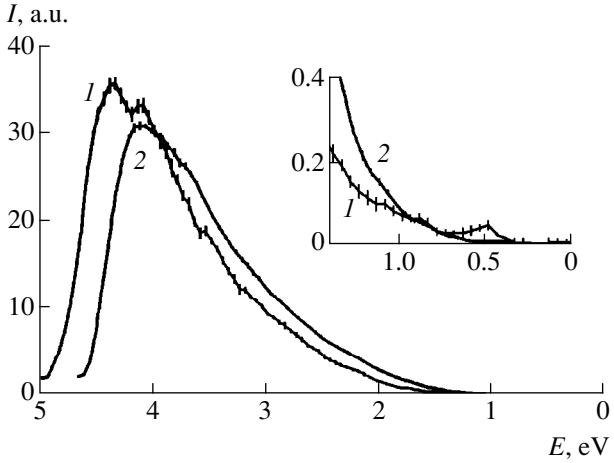

Fig. 2. UPS spectra ($h\nu$ = 8.43 eV) of (*1*) PS1 and (*2*) PS2 por-Si samples. The binding energy E is measured from the Fermi level (E_F). The inset shows the portions of spectra *1* and *2* in the region of binding energies 0–1.5 eV on a greater scale.

revealed using the following procedure. A sample was heated *in situ* under UHV conditions to T = 325, 395, and 445°C at a rate of 0.5 K/s and then cooled at the same rate. The UPS spectra were measured at the same temperatures during both heating and cooling periods. In order to eliminate the temperature-induced variations in the UPS spectra and retain only the changes related to desorption of the surface species, we determined the difference spectra $\Delta_i = \mathrm{UPS}'_{T_i} - \mathrm{UPS}_{T_i}$, where UPS'_{T_i} and UPS_{T_i} are the spectra measured at $T = T_i$ during the sample heating and cooling, respec-

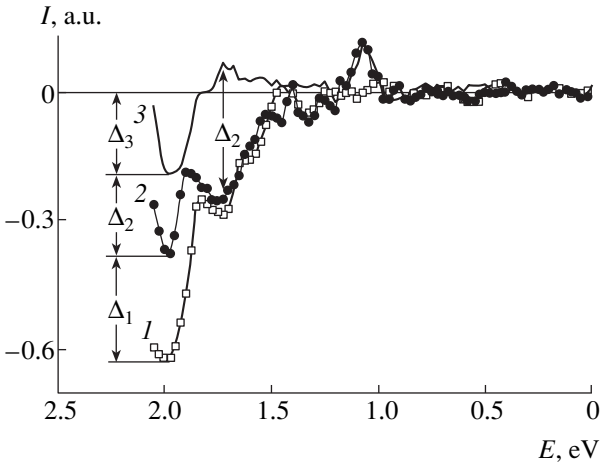

Fig. 3. Difference UPS spectra of PS2 por-Si samples measured *in situ* at the same temperature T_i in the course of heating (UPS_{T_i}) and cooling (UPS'_{T_i}) under the UHV conditions: (*1*) $UPS'_{200} - UPS_{200} = \Delta_1 + \Delta_2 + \Delta_3$; (*2*) $UPS'_{325} - UPS_{325} = \Delta_2 + \Delta_3$; (*3*) $UPS'_{395} - UPS_{395} = \Delta_3$.

tively. These difference spectra can be presented in the form of $UPS'_{200} - UPS_{200} = \Delta_1 + \Delta_2 + \Delta_3$, $UPS'_{325} - UPS_{325} = \Delta_2 + \Delta_3$, and $UPS'_{395} - UPS_{395} = \Delta_3$, where Δ_1, Δ_2, and Δ_3 are the changes in the UPS spectra related to desorption in the temperature intervals 200–325, 325–395, and 395–445°C, respectively.

Figure 3 shows the differential spectra in the binding energy range $E < 2.2$ eV. The total desorption-induced change (curve *1*) reflects the drop in intensity of the two peaks ($E = 2.0$ and 1.75 eV) and the appearance of a new peak at 1.0 eV. The peak at 2.0 eV decreases monotonically when the sample is heated from 200 to 445°C. The peak at 1.75 eV starts decreasing at a higher temperature, but at $T > 400$°C the peak intensity even slightly exceeds the initial value. The peak at $E = 1.0$ eV appears only on heating the sample up to $T > 395$°C. Note that the UPS peak energies (2.0 and 1.75 eV) coincide to within the experimental error with the PL maxima (1.95 and 1.81 eV).

The atomic structure of the surface emitting centers was studied by the FTIR method in the 700–4000 cm^{-1} wavenumber range. The IR spectrum of the initial sample exhibits a series of absorption bands in the region of 800–1000 cm^{-1}, attributed to the bending vibrations of SiH_n groups ($n = 1$–3), and the corresponding group of absorption bands in the region of stretching vibrations 2070–2170 cm^{-1} [12]. In addition, there is an additional structureless band in the region of 1000–1200 cm^{-1} with a maximum at 1125 cm^{-1} and a shoulder at 1087 cm^{-1}, which are assigned to stretching vibrations of the Si–O–Si bonds [4, 13]. Also detected was a weak absorption in the region of 2250 cm^{-1} which is related to the vibration of hydrogen bonds in a structure of the O_3Si–H type [4]. Note also that we failed to observe the absorption of either CH_n ($n = 1$–3) groups in the 2865–2975 cm^{-1} interval or C=O groups in the region of 1720 cm^{-1}. These bands were observed for the por-Si samples prepared using the etching solutions containing ethyl alcohol [4].

By measuring the PL, UPS, and FTIR spectra *in situ* for the same sample heated in vacuum, it was possible to reveal correlations between the corresponding characteristics. It was established that the intensity of the absorption band at 914 cm^{-1} and a series of bands at 2100 cm^{-1} (assigned to SiH_n structures) drops in phase with the PL intensity and the 2-eV UPS peak height. The absorption bands at 783 and 1030 cm^{-1}, which are not observed in the FTIR spectrum of the initial sample, appear at $T > 325$°C and vary in counterphase with the 1.75-eV UPS peak. The absorption bands at 783 and 1030 cm^{-1} are assigned to the O_3Si–H and Si–O–Si structures [13]. The 1-eV UPS peak, judging by the conditions of its appearance, can be brought into correspondence with the absorption band at 865 cm^{-1} assigned to the Si–O structures [4]. The formation of these structures is accompanied by the appearance of a high density of dangling bonds playing the role of nonradiative recombination centers.

Thus, the por-Si preparation using an ethanol-free etchant markedly simplified the interpretation of the electron and luminescent spectra of these samples, which is explained by the absence of CH_n and CO_n groups on the material surface.

An analysis of the whole body of experimental data obtained in this study allows us to suggest the following model of the system of electron transitions involved in the luminescence from porous silicon. The light quanta either excite electrons from the surface energy levels lying 1.75 and 2.0 eV below the Fermi level or generate holes in the bulk, followed by their localization on these energy levels. The emission takes place upon the radiative recombination of electrons from the Fermi level with the hole centers formed with participation of the SiH_n hydrides. As the sample is heated in vacuum, the latter centers are destroyed, which results in a decrease in the concentration of photogenerated holes and the intensity of recombination luminescence. This is accompanied by oxidation of the silicon surface with the formation of various O_xSi–H and Si–O–Si structures, leading to the formation of nonradiative recombination centers of the dangling bond type corresponding to a peak at $E = 1$ eV in the UPS spectra. Both thermoactivated processes in vacuum lead to attenuation or a virtually complete quenching (at $T \geq 445$°C) of the photoluminescence from por-Si.

Conclusions. (i) The luminescence spectra of porous silicon samples free from carbon-containing contaminants exhibit two emission bands ($h\nu_{max} = 1.81$ and 1.95 eV) formed with the participation of the surface atomic structures (silicon hydride, oxyhydride,

and oxide groups). (ii) The surface hydrides in por-Si correspond to the energy levels lying 1.75 and 2.0 eV below the Fermi level (E_F), the photoionization of which leads to the appearance of radiative recombination centers. Heating the samples in vacuum at $200 \leq T \leq 445$°C results in the hydrides being gradually replaced by new oxyhydride structures. The latter structures lead to the formation of nonradiative recombination centers of the dangling bond type, which correspond to the energy level lying 1.0 eV below E_F.

Acknowledgments. The authors are grateful to N.P. Petrov, R.V. Mikhaĭlov, and P.Yu. Storozhev for their help in conducting experiments.

The work was supported in parts by the Russian Federal Program Surface Atomic Structures (project no. 3.3.99) and by the Ministry of Education of the Russian Federation (St. Petersburg State University, project no. 97-0-7.2-65).

REFERENCES

1. Y. Kanemitsu, Phys. Rep. **263** (1), 1 (1995).
2. L. Tsubeskov, K. L. Moore, D. G. Hall, and P. M. Fauchet, Phys. Rev. B **54** (12), 8361 (1996).
3. P. Maly, F. Trojanek, J. Kudra, *et al.*, Phys. Rev. B **54** (11), 7929 (1996).
4. Y. Fukuda, K. Furuya, N. Ishikawa, and T. Saito, J. Appl. Phys. **82** (11), 5718 (1997).
5. Y. Kanemitsu and Sh. Okamoto, Phys. Rev. B **56** (4), 1696 (1997).
6. J. L. Gole, F. P. Dudel, D. Grantier, and D. A. Dixon, Phys. Rev. B **56** (4), 2137 (1997).
7. F. Bentosela, P. Exner, and V. A. Zagrebnow, Phys. Rev. B **57**, 1382 (1998).
8. T. Arigane, K. Yoshida, T. Wadayama, and A. Hatta, Surf. Sci. **427-428**, 304 (1999).
9. K. N. El'tsov, V. A. Karavanskiĭ, and V. V. Martynov, Pis'ma Zh. Éksp. Teor. Fiz. **63** (2), 106 (1996) [JETP Lett. **63**, 119 (1996)].
10. R. Kumar, Y. Kitoh, and K. Hara, Appl. Phys. Lett. **63** (22), 3032 (1993).
11. A. M. Aprelev, A. A. Lisachenko, R. Laiho, *et al.*, Thin Solid Films **297**, 142 (1997).
12. M. Niwano, Surf. Sci. **427-428**, 199 (1999).
13. W. N. Huang, K. Y. Tong, and P. W. Chan, Semicond. Sci. Technol. **12**, 228 (1997).

Translated by P. Pozdeev

Technical Physics Letters, Vol. 27, No. 2, 2001, pp. 138–140. Translated from Pis'ma v Zhurnal Tekhnicheskoĭ Fiziki, Vol. 27, No. 4, 2001, pp. 12–18.

Instantaneous Emission Brightness Kinetics of Zinc Sulfide Based Electroluminescent Thin-Film Emitters

N. T. Gurin, O. Yu. Sabitov, A. V. Shlyapin, and A. V. Yudenkov

Ul'yanovsk State University, Ul'yanovsk, Russia

Received August 8, 2000

Abstract—Excited with triangular voltage pulses, electroluminescent thin-film emitters based on manganese-doped zinc sulfide exhibit a two-stage buildup and decay of the instantaneous emission brightness. The fast decay stage corresponds to the Mn^{2+} ion relaxation in zinc sulfide at a time constant of 1.4 ms. Preceding the fast stage, the slow decay stage has a time constant ten times greater and accounts for a markedly increased afterglow (phosphorescence) duration. The luminance level corresponding to the transition from the first to second stage is virtually independent of the applied voltage and the charge passed through the luminophor.

The main feature of electroluminescent thin-film (ELTF) emitters is the presence of a saturation portion on their voltage–luminance diagrams presenting the average (apparent) emission brightness as a function of the amplitude of an (alternating-sign) excitation voltage [1]. The average luminance is determined by time averaging of the instantaneous emission brightness pulses (called the brightness waves), the shape of which depends on the form of the excitation voltage.

The instantaneous luminance decay constant determined for various forms of the excitation voltage characterizes the lifetime τ^* of excited centers (e.g., Mn^{2+} in ZnS). In ZnS with a small Mn content, τ^* is about 1.3 ms and decreases with increasing Mn concentration [1]. As the Mn content increases above 1–2 wt %, the luminance decay curve may exhibit up to four stages with decreasing lifetimes τ^*, either corresponding to single, double, and triple excited Mn centers [2] or related to different mechanisms of the excitation energy transfer to the emitting center [3]. However, the available data do not provide for a unique relationship between the voltage–luminance curve saturation and the shape of the brightness wave.

The purpose of this work was to study the phenomenon of ELTF emitter brightness saturation with increasing applied voltage by measuring the instantaneous luminance kinetics and the time variation of a charge passed through the luminophor in an ELTF emitter excited by linearly increasing voltage in the low-frequency range where the shape of the brightness waves is well known.

The experiments were performed on ELTF emitters with a MISIM-type structure, where M layers represent the lower transparent 0.2-μm-thick SnO_2-based electrode deposited onto a glass substrate and the upper nontransparent thin-film Al electrode with a thickness of 0.15 μm and a diameter of 1.5 mm, S is the 0.54-μm-thick electroluminescent ZnS:Mn (0.5 wt %) layer, and I is the 0.15-μm-thick insulating $ZrO_2 \times Y_2O_3$ (13 wt %) layer. The ZnS:Mn luminophor layer was deposited by thermal evaporation in a quasi-closed volume in vacuum, followed by the annealing for 1 h at 250°C. The nontransparent metal electrode was obtained by vacuum deposition, and thin insulating layers were prepared using the electron-beam deposition technique.

We have experimentally measured the time variation of the instantaneous luminance L and current I_e of ELTF emitters excited with alternating-sign voltage pulses of a triangular shape. The excitation signal was supplied from a G6-34 generator with an additional shaping amplifier, controlled by a G5-89 master generator. The pulse amplitude was 160–170 V at a nonlinearity coefficient not exceeding 2%. A single excitation cycle represented a train of two-period triangular pulses with a repetition rate of 10, 50, 200, 500, or 1000 Hz. The time interval T_s between single excitation cycles could be varied from 0.1 to 100 s. In a continuous excitation mode, the pulse repetition frequency was varied from 10 to 1000 Hz. The I_e value was measured in a 100 Ω–10 kΩ resistor connected in series with the ELTF emitter structure (the voltage drop on this resistor did not exceed 1 V). The instantaneous luminance was measured with a photoelectron multiplier tube FEU-84-3.

The patterns of excitation voltage, ELTF emitter current, and instantaneous emission brightness variation were registered with a two-channel storage oscillograph of the S9-16 type linked via an interface to a personal computer. The system provided the measurement and storage of 2048 experimental points at a preset discretization period in each channel with an error not exceeding 2%. The data were mathematically and graphically processed using the application program

1063-7850/01/2702-0138$21.00 © 2001 MAIK "Nauka/Interperiodica"

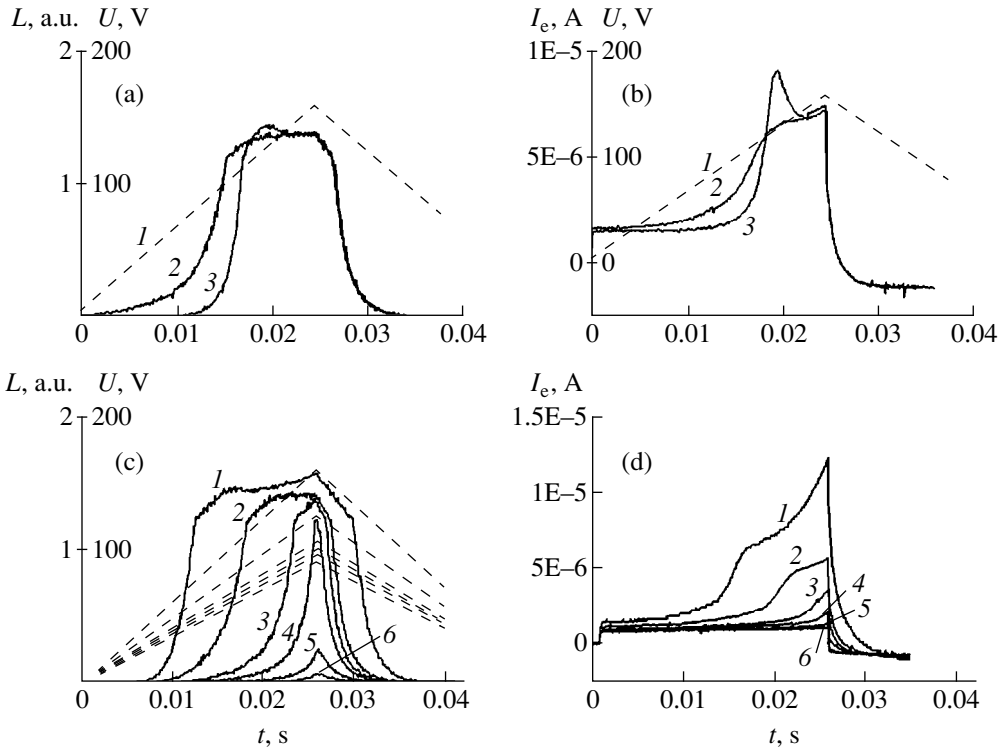

Fig. 1. Time variation of the (a, c) instantaneous luminance L and (b, d) emitter current I_e measured at an excitation frequency of 10 Hz. Sample no. 1 (a, b): (*1*) excitation pulse shape; (*2*) continuous excitation mode; (*3*) single excitation cycle mode (T_s = 100 s). Sample no. 5 (c, d) was excited in the single cycle mode (T_s = 1 s) at an excitation pulse amplitude (*1*) 160, (*2*) 125, (*3*) 105, (*4*) 100, (*5*) 95, and (*6*) 90 V.

packages MAPLE V (Release 4, Version 4.00b) and GRAPHER (Version 1.06, 2-D Graphing System).

The charge transferred through a luminophor layer is equal, in the absence of recombination losses and carrier trapping, to the charge Q_p accumulated in the active regime on the states at the interface. This charge is related to the charge Q_e passed in the external circuit by the following equation [4]:

$$Q_p(t) = \frac{C_i + C_p}{C_i}[Q_e(t) - C_e V(t)] + Q_{pol}, \qquad (1)$$

where

$$Q_e(t) = \int_0^t I_e(t)dt. \qquad (2)$$

Q_{pol} is the residual polarization charge, and C_i and C_p are the capacitances of the capacitors formed by two insulating layers separating electrodes and the luminophor.

The results of our previous investigation of the instantaneous emission brightness kinetics [5] showed that, beginning with the second period of the excitation voltage in a single excitation cycle mode with any T_s, the $L(t)$ and $I_e(t)$ curves are identical to the corresponding curves obtained in the continuous excitation mode. This fact indicates that the transition to a quasistationary (continuous) operation regime is completed within the first cycle of the excitation voltage variation. This circumstance was used to determine the initial conditions for the $Q_p(t)$ charge calculation by Eqs. (1) and (2), which correspond to the residual polarization charge Q_{pol} accumulated by the time of arrival of the next train of the excitation voltage pulses.

The experimental $L(t)$ and $I_e(t)$ curves and the $L(Q_p)$ relationship exhibit the following characteristic features:

(i) An additional peak in the I_e current pulse (analogous to that observed in [4]) appears in the single excitation cycle mode in the first half-period of the excitation voltage. The amplitude of this peak increases with T_s. The corresponding peak in the instantaneous luminance curve $L(t)$ (Figs. 1a, 1b) is explained by an increase in probability of the emitting center excitation, which is proportional to the current density I_p [6].

(ii) The instantaneous luminance L increases with time up to a certain level more rapidly than does the current I_e. This stage is followed by a slower stage, after which the $L(t)$ curve reaches a saturation level (Figs. 1a, 1c). The slow stage obeys the law $1 - \exp(-t/\tau)$ with $\tau = 1.5 \pm 0.3$ ms, which corresponds to the lifetime of the excited Mn^{2+} centers [1].

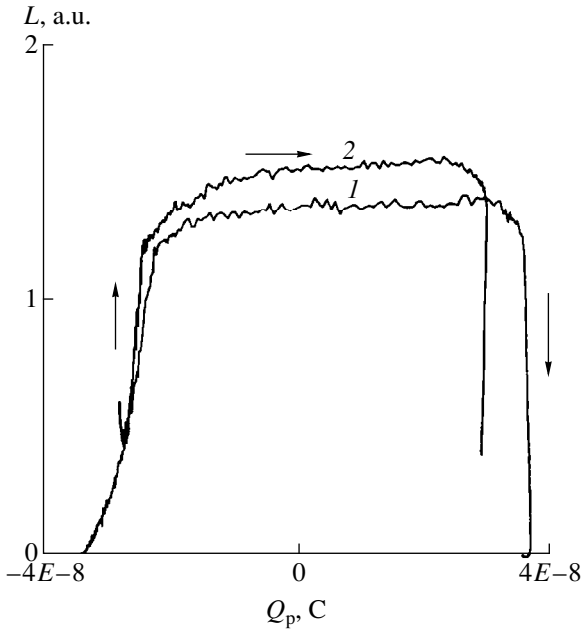

Fig. 2. The plots of instantaneous luminance (L) versus charge Q_p passed through the luminophor measured in the continuous excitation mode (sample no. 1) for f = 10 (*1*) and 50 Hz (*2*).

(iii) The decay of the $L(t)$ curve (Figs. 1a, 1d) measured at 10 and 50 Hz exhibits two clearly pronounced exponential stages with different time constants: $\tau_1 = 14 \pm 4$ ms and $\tau_2 = 1.5 \pm 0.2$ ms, the latter corresponding to the lifetime of the single excited Mn^{2+} centers. To our knowledge, no data on the first decay stage are available in the literature.

(iv) The emission brightness level L corresponding to a transition from first to second stage is (to within the experimental accuracy) the same for the luminance buildup and decay periods. Moreover, this level depends neither on the frequency f (in the 10–1000 Hz range) nor on the Q_p charge passed through the luminophor.

(v) The plots of instantaneous luminance L versus charge Q_p passed through the luminophor (for the same time period t) reveal (Fig. 2) two portions. The first portion reflects a sharp increase in the emission brightness L upon a small change in Q_p, while the second portion is characterized by a weak dependence of L on Q_p.

The above features can be explained as follows. As is known [1, 6], the instantaneous ELTF emitter luminance $L(t)$ is related to the concentration of excited emitting centers $N^*(t)$ by the formula

$$L(t) = \frac{AN_1P_rN^*(t)}{\tau^*}, \qquad (3)$$

where A is a constant factor, N_1 is the number of emitting centers excited by a single electron passing through the luminophor layer, $P_r = \tau^*/\tau_r$ is the probability of a radiative relaxation of the emitting center, τ^* is the lifetime of the emitting center in the excited state, and τ_r is the lifetime of the emitting centers capable of the radiative relaxation. As seen from formula (3), the appearance of saturation in the $L(t)$ and $L(Q_p)$ curves is most simply explained by the corresponding decrease in N_1 (after which even a considerable growth in Q_p or in the number of charge carriers passing through the luminophor leads to no significant increase in the emission brightness). This is evidence of the saturation of the concentration of excited emission centers. Under these conditions, there may appear a resonance interaction of these centers with each other and/or with the environment in the ZnS lattice upon termination of the excitation pulse. It is this interaction that may lead to an increase in τ^* in the first ("slow") luminance decay stage (e.g., at the expense of a change in the probability of radiative and nonradiative transitions). As the concentration of excited centers decreases to a certain level, the resonance interaction ceases and the subsequent relaxation proceeds via single Mn^{2+} centers.

It should be noted that the appearance of the first (slow) stage in the luminance decay kinetics $L(t)$ markedly increases the duration of afterglow (i.e., the average ELTF emitter brightness) observed at low frequencies of the excitation voltage (10 and 50 Hz).

REFERENCES

1. *Electroluminescent Light Sources*, Ed. by I. K. Vereshchagin (Énergoatomizdat, Moscow, 1990).
2. N. A. Vlasenko, Yu. V. Kopytko, and V. S. Pekar, Phys. Status Solidi A **81** (10), 661 (1984).
3. A. A. Zhigal'skiĭ, E. V. Nefedtsev, and P. E. Troyan, Izv. Vyssh. Uchebn. Zaved., Fiz., No. 2, 37 (1995).
4. N. T. Gurin, A. V. Shlyapin, and O. Yu. Sabitov, Zh. Tekh. Fiz. **71** (3), 72 (2001) [Tech. Phys. **46**, 342 (2001)].
5. N. T. Gurin, A. V. Shlyapin, and O. Yu. Sabitov, in *Proceedings of the International Conference "Optics of Semiconductors"* (Ul'yanovsk. Gos. Univ., Ul'yanovsk, 2000), pp. 80–81.
6. N. T. Gurin and O. Yu. Sabitov, Zh. Tekh. Fiz. **69** (5), 65 (1999) [Tech. Phys. **44**, 537 (1999)].

Translated by P. Pozdeev

Technical Physics Letters, Vol. 27, No. 2, 2001, pp. 141–143. Translated from Pis'ma v Zhurnal Tekhnicheskoĭ Fiziki, Vol. 27, No. 4, 2001, pp. 19–25.

The Velocity and Attenuation of Outgoing Surface Acoustic Waves Measured Using an Ultrasonic Microscope with Two Focusing Transducers

S. A. Titov, R. G. Maev, and A. N. Bogachenkov

Emanuel Institute of Biochemical Physics, Russian Academy of Sciences, Moscow, 117977 Russia

Received October 2, 2000

Abstract—A new method for measuring the local parameters of outgoing surface acoustic waves (OSAWs) is proposed. The technique employs a system of two focusing transducers, with the output signal taken from one of these scanning over the sample surface. In comparison with the conventional method with a single transducer moving in the direction normal to the sample surface, the proposed technique is capable of conducting measurements in a greater range of OSAW velocities and is less sensitive to parameters of the immersion liquid. The new method was experimentally verified by measuring systems with known properties. © *2001 MAIK "Nauka/Interperiodica".*

Among the quantitative acoustic microscopy methods capable of measuring the local parameters of outgoing surface acoustic waves (OSAWs), the most widely used is the so-called $V(z)$ technique [1].

Let us consider the principle of this method in the ray approximation. A focusing transducer *1* (Fig. 1a) excited by an electric signal $P(t)$ radiates an ultrasonic wave. The wave propagates in an immersion medium, reflects from a sample *2*, and is detected by the same transducer. If the sample shifts out of the focal plane ($z < 0$) toward the transducer, the main contribution to the output transducer signal V is due to the acoustic rays d and $r_1 - r_2$ (Fig. 1). Indeed, ray d traveling along the normal to the sample surface is incident perpendicularly onto the transducer surface and, hence, is effectively detected. Ray r_1 is incident onto the sample surface at a critical angle with respect to excitation of the outgoing surface acoustic wave θ_R. Traveling over the sample surface, this OSAW is continuously reemitted into the immersion liquid. Among the reemitted rays, only r_2 is incident perpendicularly onto the transducer surface to give an effective contribution to the output signal V.

In the case of a narrowband excitation of the transducer, the received signal features a beat of response signals corresponding to the d and $r_1 - r_2$ rays, whereby the modulus $|V(z)|$ exhibits characteristic oscillations. By determining the period and the amplitude decay rate of these oscillations, it is possible to measure the velocity and attenuation of OSAWs [2]. For a wideband excitation of the transducer, the d and $r_1 - r_2$ response components in the output signal $V(z, t)$ can be separated in time (provided that the sample displacement from the focus is sufficiently large). A relative delay t_R of these components is given by the expression [3]

$$t_R = \frac{2z(1 - \cos\theta_R)}{C}; \quad \cos\theta_R = \sqrt{1 - \frac{C^2}{C_R^2}}, \qquad (1)$$

where $C \approx 1500$ m/s is the ultrasonic signal speed in the immersion liquid (water) and C_R is the OSAW velocity. Note that the results of the C_R measurements depend not only on the delay time t_R, but on the ultrasonic signal velocity C as well. The latter value may significantly change depending on the immersion liquid parameters, in particular, on the temperature.

As is seen from Fig. 1, the measuring system under consideration does not allow the excitement of OSAWs for which the critical angle is greater than maximum aperture angle of the transducer ($\theta_R > \theta_m$). Thus, the $V(z)$ method described above is inapplicable in the

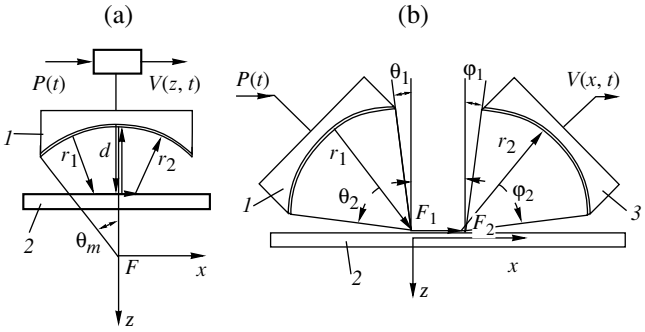

Fig. 1. Schematic diagrams showing the geometry of measurements with (a) a single transducer moving perpendicularly to the sample surface and (b) two transducers one of which is scanning along the sample surface: (*1*, *3*) focusing transducers; (*2*) sample.

1063-7850/01/2702-0141$21.00 © 2001 MAIK "Nauka/Interperiodica"

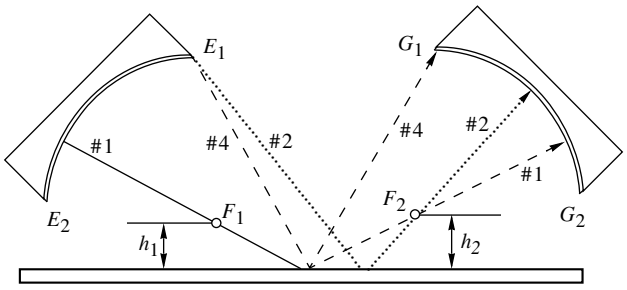

Fig. 2. A schematic diagram showing various rays (wave modes) propagating in the measuring system employing two transducers (see the text for explanations).

range of small velocities $C_R < C/\sin\theta_m$. Note that the θ_m value cannot be arbitrarily selected because the interval of scanning along the *z* coordinate must be as large as possible in order to provide for a sufficiently high accuracy of measurements. For this reason, the θ_m angle usually does not exceed 40°; accordingly, the velocities $C_R < 2400$ m/s cannot be measured using water as the immersion liquid.

We propose to use a system employing two tilted transducers (Fig. 1b), with the output signal taken from one of these as it scans over the sample surface. In a measuring system of this configuration, the transmitting transducer *1* may excite OSAWs with critical angles within a certain range (θ_1, θ_2). Accordingly, the receiving transducer *2* may detect OSAWs in the angular interval (φ_1, φ_2). Since transducer *2* scans along the *x* axis, the gap between transducers and the sample surface can be small and the angles θ_2 and φ_2 may close to 90°. This implies that the interval of measurable OSAW velocities can be extended up to a level approaching the velocity of ultrasonic signal in the immersion liquid (for water, $C = 1500$ m/s).

As can be readily seen, a change in the delay time Δt_R of the OSAW response is proportional to the corresponding focal shift Δx of the mobile transducer:

$$\Delta t_R = \frac{\Delta x}{C_R}. \qquad (2)$$

Thus, the results of determination of the OSAW velocity C_R by this method are independent of the immersion liquid parameters, including the temperature.

In order to experimentally verify the proposed method, we have constructed a measuring system implementing two cylindrical focusing transducers made of a piezoelectric poly(vinylidene fluoride) (PVDF) film. The metal-coated PVDF film was glued to a concave surface of a monolithic epoxy block. The outer film surface was in direct contact with the immersion liquid (water). This system possesses a good wideband characteristic and a small reverberation noise level because of the absence of an acoustic lens [3]. The transducer width along the generating line was 12 mm and the focal distance was $R = 9$ mm; the aperture angles were $\theta_1 = 90°$, $\theta_2 = 10°$, $\varphi_1 = 80°$, and $\varphi_2 = 10°$ (Fig. 1b). The foci of both transducers (F_1 and F_2) were at a distance of $h_1 = h_2 = 1.2$ mm over the sample surface (Fig. 2). The transmitting transducer was excited by single pulses with an amplitude of 150 V and a duration of 30 ns; the sample response was detected in a 1–30 MHz frequency band with a central frequency of 12 MHz; the signal to noise ratio was not less than 40 dB.

Figure 3 shows the results of measurements of the $V(x, t)$ signal for various materials, presented in the form of half-tone images. Positive values of the output signal correspond to the bright regions, the negative values are imaged by the dark field, and the zero signal corresponds to the gray color. The presence and behavior of the acoustic response can be interpreted within the framework of the ray approximation. Response #1 (Fig. 2) is generated by a ray passing through the F_1 and F_2 foci and reflected from the sample surface. The responses of other types are obtained from the transducer edges E_1, E_2, G_1, and G_2 that may serve as sources and receivers of the cylindrical edge waves. Ray #2 is radiated by edge E_1 and detected upon reflection from the sample and passage through the F_2 focus. By the same token, response #3 (not shown in Fig. 2) corresponds to a ray passing through F_1 and detected by edge G_1. Finally, responses #4 (5) are detected upon traveling by the paths $E_{1(2)}$–sample–$G_{1(2)}$, respectively. As can be seen from simple geometric considerations, the distances traveled by these rays can be determined by following formulas:

$$d_1 = \sqrt{h^2 + x^2} + 2R; \qquad (3)$$

$$d_2 = \sqrt{(R\sin\theta_1 + h)^2 + (R\cos\theta_1 + x)^2} + R; \qquad (4)$$

$$d_3 = \sqrt{(R\sin\varphi_1 + h)^2 + (R\cos\varphi_1 + x)^2} + R; \qquad (5)$$

$$d_{4(5)} = \sqrt{(R\cos\theta_{1(2)} + R\cos\varphi_{1(2)} + x)^2 + (R\sin\theta_{1(2)} + R\sin\varphi_{1(2)} + h)^2}, \qquad (6)$$

where $h = h_1 + h_2$ and *x* is the distance between foci. The results of calculations of the relative delay values for the waves traveling by the distances $d_1 - d_5$ are plotted in Fig. 3b, where the curve numbers correspond to the numbers of rays (#1–#5) considered above. A comparison of the results of calculations with the experimentally measured patterns (Figs. 3a, 3c, and 3d) shows that the maximum amplitude corresponds to ray #1 passing through both foci. Rays #2 and #3 passing through foci and edges of the transducers are less

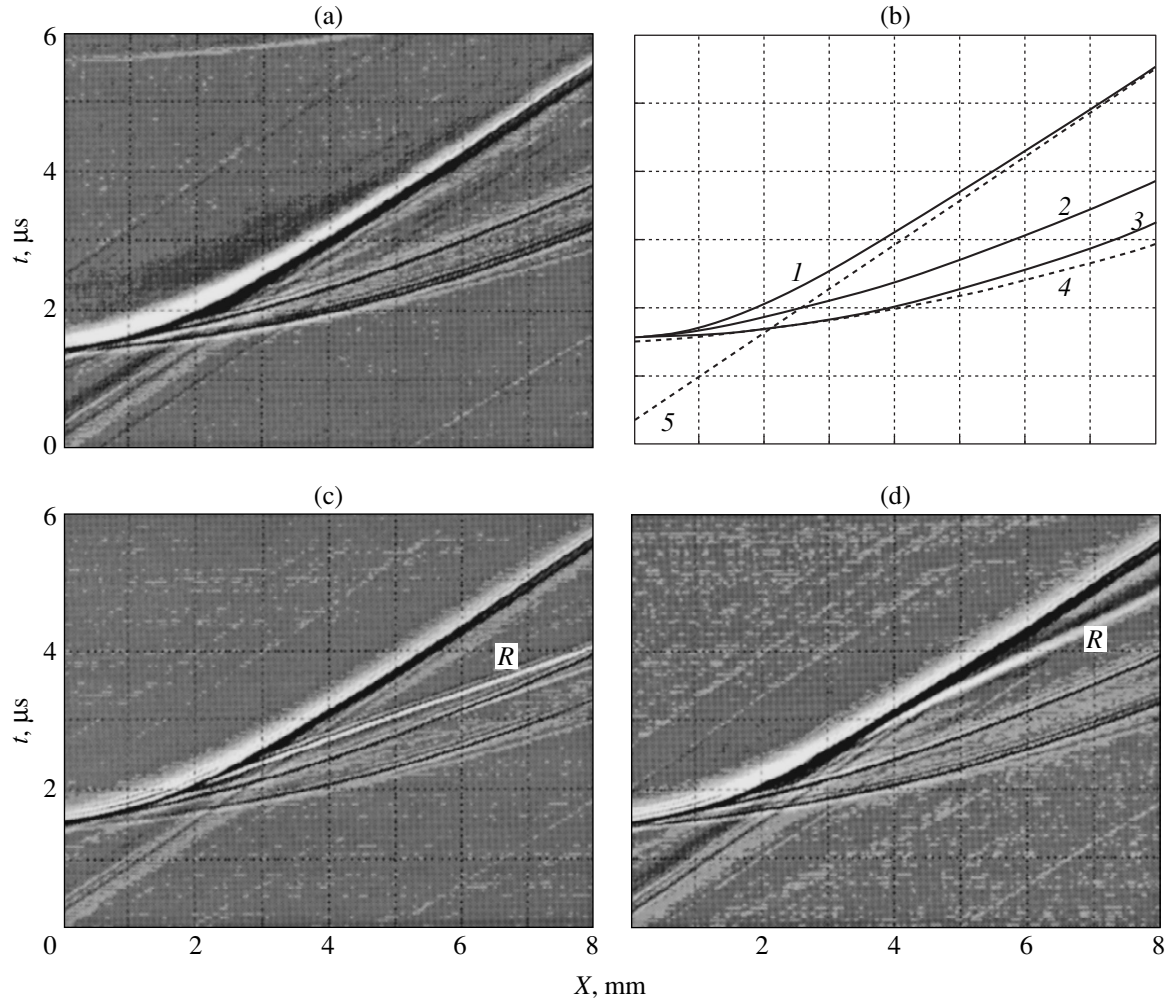

Fig. 3. The patterns of acoustic response $V(x, t)$ measured for (a) lead, (c) carbon steel, and (d) copper and (b) the results of calculation of the relative delay values for various wave modes (the curve numbers correspond to the numbers of rays; see the text for explanations).

intense, while rays #4 and #5 (emitted and detected at the transducer edges) partly overlap with rays #3 and #1, respectively. The shapes of calculated curves are consistent with the relative delays of the measured signals $V(x, t)$, which confirms the validity of the ray approximation employed.

The experimental data obtained for steel and copper samples (Fig. 3c and 3d) show, in addition to the set of rays considered above, responses R corresponding to the outgoing Rayleigh surface waves. In lead (Fig. 3a), where the Rayleigh wave velocity is smaller than the sound velocity in the immersion liquid used, this OSAW cannot be excited and the corresponding response is not observed. For the observed responses R, the delay varies linearly with the distance x. Using formula (2), we obtain C_{steel} = 3024 m/s and C_{copper} = 2147 m/s for the steel and copper samples, respectively. Calculations using the known acoustic parameters of these metals yield C_{steel} = 3015 m/s and C_{copper} = 2115 m/s. The OSAW attenuation coefficients determined using experimental data on the decay rate of the detected response pulses are $\alpha_{steel} = 0.26$ mm^{-1} and $\alpha_{copper} = 0.6$ mm^{-1}, to be compared with the calculated values of $\alpha_{steel} = 0.28$ mm^{-1} and $\alpha_{copper} = 0.53$ mm^{-1}. As can be seen, there is satisfactory agreement between the experimental and calculated values, which can be considered as experimental verification of the proposed method.

REFERENCES

1. A. Briggs, *Acoustic Microscopy* (Clarendon Press, Oxford, 1992).
2. J. Kushibiki and N. Chubachi, IEEE Trans. Sonics Ultrason. **SU-32** (2), 189 (1985).
3. D. Xiang, N. N. Hsu, and G. V. Blessing, Ultrasonics **34**, 641 (1996).

Translated by P. Pozdeev

Technical Physics Letters, Vol. 27, No. 2, 2001, pp. 144–146. Translated from Pis'ma v Zhurnal Tekhnicheskoĭ Fiziki, Vol. 27, No. 4, 2001, pp. 26–32.

Beam–Plasma Discharge Dynamics in an Adiabatic Magnetic Trap

Yu. Ya. Volokolupov and M. A. Krasnogolovets

Kharkov Physicotechnical Institute, Kharkov, Ukraine

Received October 6, 2000

Abstract—The rate of plasma expansion in the direction perpendicular to the magnetic field lines was determined and the turbulent plasma diffusion coefficient was calculated using data obtained by methods of X-ray diagnostics. A correlation between the plasma diffusion coefficient and the amplitude of the RF oscillations in the system was established. This correlation leads to an increase in the electron temperature and the expansion of plasma in the radial direction. The transfer processes in the plasma are markedly influenced by the magnetic field: for example, the relationship $D_\tau \sim \frac{1}{B^2}$ was observed in the range of magnetic field strengths $B < 2$ kG. © *2001 MAIK "Nauka/Interperiodica".*

An electron beam injected into a cold plasma initiates a beam–plasma discharge and gives rise to high-power RF oscillations [1]. These phenomena result in the heating of a certain fraction of electrons, the energy of which is several times that of the electron beam energy. A characteristic feature of the beam–plasma discharge is the considerable increase in the cross section beyond that of the primary electron beam. This expansion of the plasma in the radial direction is related to diffusion of the hot and cold plasma components.

The experiments were performed in an axisymmetric vacuum system exposed to an inhomogeneous magnetic field having the configuration of a magnetic trap with magnetic mirrors. At the trap center, the magnetic field strength reached the value of $B = 1.5$ kG for a mirror ratio of $R = 4$. The internal diameter of the vacuum chamber in the region of magnetic mirrors was 14 cm, the distance between the mirrors was $l = 80$ cm, and the working gas pressure in the chamber was $p = 10^{-4}$ Torr.

A pulsed electron beam injected into the magnetic trap volume had a pulse duration of $\tau = 500$ μs, an acceleration voltage of $U = 25$ kV, and a beam current of $I = 40$ A. The electron injector (gun) cathode was placed in front of the magnetic mirror, at a point with $B_m/B_a = 4$ (where B_m and B_a are the magnetic field strengths in the mirror and at the system axis in the region of the injector, respectively).

The electron beam cross section was monitored using a thermal probe operating in a high vacuum ($p = 10^{-7}$ Torr), that is, in the absence of the beam–plasma interaction. The beam diameter at the magnetic trap center was $d = 1.2$ cm. Passing through the magnetic trap, the electron beam was accepted with a grounded electron collector representing a Faraday cylinder. In the initial stage of the beam–plasma discharge formation, the residual gas molecules were ionized by direct collision with electrons of the beam.

As the plasma density increased to a level equal to the electron beam density ($n_0 \approx n_{\text{beam}}$), the beam–plasma system was excited to give rise to RF oscillations and the beam instability development. The electron beam energy was virtually completely dissipated within a region with dimensions equal to those of the magnetic trap. As a result, the electron density (n_e) and temperature (T_e) in the plasma markedly increased [2]. The electron component of the plasma comprised two groups of electrons possessing markedly different temperatures: "superhot" electrons with $kT_e > eU$ and "cold" electrons with $kT_e \ll eU$ (where k and e are the Boltzmann constant and the electron charge, respectively); the hot and cold electrons also possessed different velocities in the radial direction.

For a cold plasma, the expansion velocity was determined by measuring the delay time between the appearance of light emission from the plasma region and the leading front of a pulse accelerating the electron beam. A collimated light beam emitted from a small ($r = 0.3$ cm) plasma region was detected with a photoelectron multiplier tube. The measuring system was capable of simultaneously detecting the light emitted from plasma regions at various distances from the axis. The velocity of the hot-electron plasma boundary motion was determined by measuring the delay time between the signal from an X-ray transducer (occurring at a certain distance from the system axis) and the onset of intense light emission from the axial plasma region.

Figure 1 shows typical oscillograms of the X-ray radiation (upper pulses) generated due to the hot electron stopping on the probe; the lower oscillograms show envelopes of the total optical emission pulses.

The results of processing the oscillographic data are presented in Fig. 2, showing a plot of the outer boundary velocity V of the hot-plasma region versus the X-ray probe distance r from the system axis. As seen, the outer hot-plasma boundary velocity sharply drops with increasing distance from the beam axis. Another probe was used for simultaneously measuring the amplitude of the RF oscillations [3]. The results of these measurements showed that the RF amplitude increased on approaching the electron beam boundary. This observation suggests that more intense RF oscillations in the paraxial beam region are a factor responsible for the greater velocity of the plasma boundary moving out of the beam region.

The most important characteristics of the plasma are its total thermal energy and the energy distribution over the volume. Study of the energy distribution in the cross section of a hot-electron plasma encounters certain difficulties. The relative energy density variation along the radius of the plasma column was measured with the aid of a miniature thermal probe. The results of these experiments showed that a measurable thermo emf appeared only when the probe contacted with a hot-electron plasma region while being negligibly small in contact with a cold plasma.

The pattern obtained with the aid of the thermal probe is well correlated with the variation of signals from the X-ray probe [4]. This correlation indicates that the main fraction of the plasma energy is contained in hot electrons. The nT versus magnetic field strength curve obtained using the thermal probe exhibits a dome shape with the nT maximum reached at $B = 0.9$ kG in the magnetic trap center, which is consistent with the data on the gasokinetic plasma pressure variation measured with the aid of a diamagnetic probe. The results of these investigations showed that the plasma energy distribution in the column cross section is characterized by a maximum at $r = 4$ cm rather than at the axis. This pattern can be explained as follows.

The first key factor is a considerable decrease in the outer hot-plasma boundary velocity on approaching the conducting walls of the vacuum chamber. A set of miniature thermal probes arranged at a certain distance from each other allowed the RF field to be measured and provided data on the time variation and spatial distribution of plasma pulsations. An analysis of these data showed that the plasma features large-scale oscillations with a range on the order of the magnetic trap dimensions. Interaction of the plasma with these oscillations determines the observed velocity of the plasma boundary motion in the direction perpendicular to the magnetic field lines.

The second factor is the energy gained by hot electrons from the RF oscillations, which is proportional to the distance from the system axis. However, for a plasma column radius $r > R_0$, the electron beam energy is insufficient to maintain the efficiency of heating plasma electrons in this large volume on a high constant

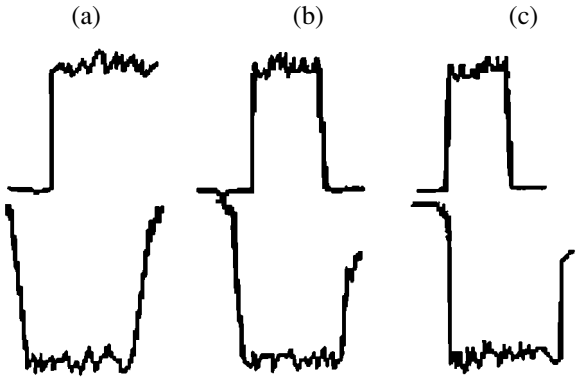

Fig. 1. Typical oscillograms showing (top row) the X-ray radiation pulses (detected by solid-target probes) and (bottom row) the integral light pulses from small plasma regions (detected by a collimated radial transducer). The transducers were arranged at various distances from the system axis $r = 3.8$ (a); 2.8 (b); 2.2 cm (c).

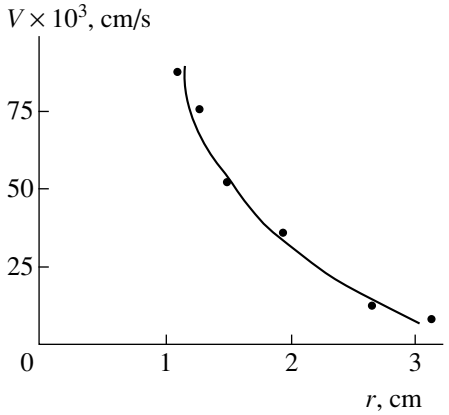

Fig. 2. A plot of the hot-electron plasma boundary velocity V versus distance r from the system axis ($U = 25$ kV; $I = 5$ A; $P = 1 \times 10^{-4}$ Torr; $B = 1.3$ kG).

level. Beginning with a certain r value, the gasokinetic pressure decreases and tends to zero as the plasma expands toward the chamber walls.

As could be readily seen, the outer hot-plasma boundary velocity depended on the magnetic field strength. By measuring the delay time τ of the hot-electron pulse arrival to the probe situated at a given distance r from the system axis, it was possible to estimate the diffusion coefficient using the well-known relationship $r = \sqrt{D_\tau \tau}$.

The motion of hot electrons in the radial direction (i.e., perpendicular to the magnetic field lines) is due to their scattering on RF oscillations. The corresponding drift coefficient D_τ will be referred to as the turbulent diffusion coefficient. As indicated above, the hot-electron plasma expansion velocity depends on the distance from the system axis: $D_\tau = D_\tau(r)$. Therefore, the turbulent diffusion coefficient presents a rather conditional

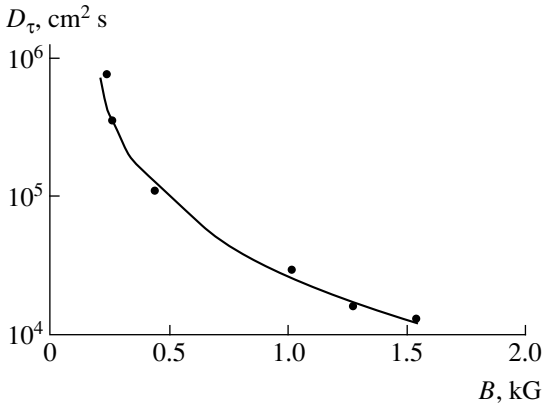

Fig. 3. A plot of the turbulent plasma diffusion coefficient D_τ versus magnetic field strength B (U = 25 kV; I = 5 A; $P = 1 \times 10^{-4}$ Torr; B = 1.3 kG).

characteristic and we prefer to use the D_τ value averaged over the radius r.

Using the method described above, we studied the turbulent diffusion coefficient as a function of the magnetic field strength: $D_\tau = D_\tau(B)$. Based on these data, it was established that, within a certain interval of experimental conditions, dependence of the D_τ value on the magnetic field strength B is close to A/B^2 (Fig. 3). Note, however, that the D_τ value is markedly greater than the classical diffusion coefficient determined by the formula

$$D_c = \frac{8\sqrt{2}\pi e^2 c^2 m^{1/2}\lambda N}{B^2(kT_e)},$$

where e and m are the electron charge and mass, respectively; c is the speed of light; λ is the Coulomb logarithm; T_e is the electron temperature; and N is the mean plasma density. On the other hand, the experimentally determined D_τ value is markedly smaller as compared to that calculated by the Bohm formula

$$D_B = \frac{ckT_e}{16eB}.$$

A relationship between the three quantities is as follows: $D_c : D_\tau : D_B = 1 : (1.5 \times 10^3) : 10^6$. Simultaneous determination of the velocities of the hot and cold plasma boundaries showed the mean velocity of the cold plasma boundary to be 2–3 times that of the hot component boundary.

The plasma photographs in the X-ray beams, together with the data obtained using thermal probes, showed that the plasma column retained axial symmetry during the whole time of the electron beam injection and the plasma expansion. The plasma column exhibited a well-defined external boundary and occupied a volume that was considerably smaller compared to that of the magnetic trap.

Thus, it was experimentally established that the radius of the hot-electron plasma region decreases with increasing magnetic field strength, in agreement with conclusions following from the diffusion model of plasma heating [3, 5]. The study of macroscopic characteristics of the beam–plasma discharge in the stage of plasma expansion together with investigation of the RF beam parameters by the probe techniques allowed us to explain an increase in the radial plasma expansion velocity by its relationship to the turbulent diffusion coefficient.

REFERENCES

1. B. B. Kadomtsev, *Collective Phenomena in Plasmas* (Nauka, Moscow, 1976), p. 238.
2. M. A. Krasnogolovets, Yu. Ya. Volokolupov, and I. Yu. Galushko, in *Proceedings of the 3rd International Scientific and Technical Conference "Methods of Visualization and Processing of Random Signals and Fields," Kharkov, 1993*, pp. 155–158.
3. Yu. Ya. Volokolupov, M. A. Krasnogolovets, and A. A. Khar'kovskaya, in *Proceedings of the 2nd International Conference "Theory and Techniques of the Information Transfer, Receiving, and Processing," Tuapse, 1996*, pp. 234–235.
4. M. A. Krasnogolovets, Radiotekhnika, No. 105, 195 (1998).
5. D. D. Ryutov, Zh. Éksp. Teor. Fiz. **57**, 232 (1969) [Sov. Phys. JETP **30**, 131 (1970)].

Translated by P. Pozdeev

Technical Physics Letters, Vol. 27, No. 2, 2001, pp. 147–149. Translated from Pis'ma v Zhurnal Tekhnicheskoĭ Fiziki, Vol. 27, No. 4, 2001, pp. 33–38.

Effect of the Spin Wave Decay in the Pinning Layer on the Spin Wave Resonance Band Intensity

A. M. Zyuzin, S. N. Sabaev, A. G. Bazhanov, and V. V. Radaĭkin

Mordvinian State University, Saransk, Mordvinia, Russia

Received February 2, 2000; in final form, October 12, 2000

Abstract—The spin wave resonance band intensity in two-layer film structures exhibits an anomalous variation. The experimental data and the results of model calculations indicate that a mechanism responsible for the resonance band intensity increase with the mode number is related to the presence of a spin wave decay region in the pinning layer. © *2001 MAIK "Nauka/Interperiodica".*

According to the spin wave resonance (SWR) theory [1–3] the absorption band intensity I_n of the spin wave (SW) modes must decrease with increasing mode number n. In a system featuring the complete spin pinning, this decrease proceeds by the law $I_n \sim n^{-2}$ [2]. Deviations from the regular mode intensity distribution may be caused by asymmetry in the boundary conditions and by dependence of the degree of pinning on the SW mode number, which results in the excitation of intermediate modes [4]. In the latter case, the deviation from regularity must exhibit a periodic character.

We have observed the "anomalous" behavior of the SW mode absorption intensity within a certain interval of wavenumbers, whereby an increase in the mode number was accompanied by a monotonic increase (rather than decrease) in the absorption band intensity. The experiments were performed with two-layer single crystal garnet ferrite films, in which the spin pining is known to proceed predominantly by the dynamic mechanism [5]. The films were prepared by liquid-phase epitaxy (LPE) from various solution melts on (111)-oriented gadolinium–gallium garnet substrates. The first LPE-grown layer had the composition $(BiSmTm)_3(FeGa)_5O_{12}$ with a magnetization of $4\pi M$ = 600 G, a Gilbert decay parameter of $\alpha = 0.013$, and an effective uniaxial anisotropy field strength of H_k = –270 Oe. The second epitaxial layer had the composition $(YSm)_3Fe_5O_{12}$ and the parameters $4\pi M$ = 1720 G, $\alpha = 0.003$, and H_k = –1680 Oe.

Figure 1 shows the SWR spectra measured for various angles Θ_H between the constant magnetic field **H** and the normal to the sample surface. At $\Theta_H \approx 33°$, the spectrum degenerates into a single mode. The degeneracy is related to the fact that the homogeneous resonance fields H_{01} and H_{02} for this angle are equal and the dynamic spin pinning mechanism becomes inoperative.

A remarkable feature was that the SWR spectra measured for a perpendicular orientation ($\Theta_H = 0°$) exhibited a single group of absorption peaks (Fig. 1, series II), while the spectra measured for the parallel orientation ($\Theta_H = 90°$) displayed two groups of peaks (series I and II). For both orientations, series II corresponds to the SW modes excited in the second layer. This is confirmed by virtually the same slope of the dispersion curves observed for both orientations (see the inset in Fig. 2) and by the results of experiments with gradual etching of the samples. The distribution of peak intensities observed in series II agrees with that predicted by the well-known models, showing a decrease with increasing SW mode number.

Of special interest is the series of peaks I observed for $\Theta_H = 90°$, the nature of which is by no means evident. The peak intensity in this series decreases with distance from the zero-mode peak of the second layer. However, it is clear that these peaks cannot be related to harmonic SW modes excited in the second layer because this layer represents a reactive (elastic) medium

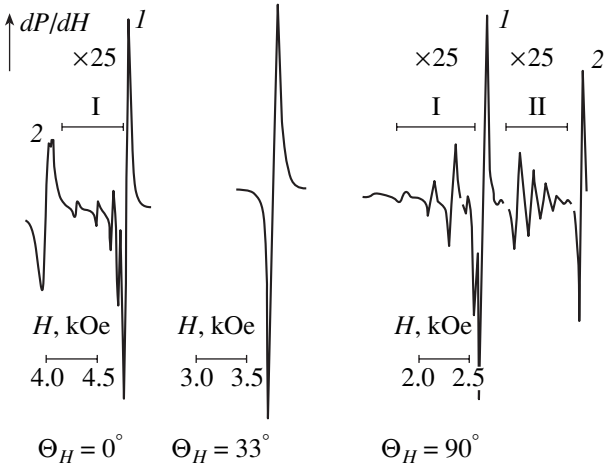

Fig. 1. SWR spectra measured for the perpendicular (Θ_H = 0°), intermediate (Θ_H = 33°), and parallel (Θ_H = 90°) orientations of the magnetic field **H** relative to the film surface: peaks *1* and *2* correspond to zero modes of the corresponding layers; I and II are the series of excited bands.

1063-7850/01/2702-0147$21.00 © 2001 MAIK "Nauka/Interperiodica"

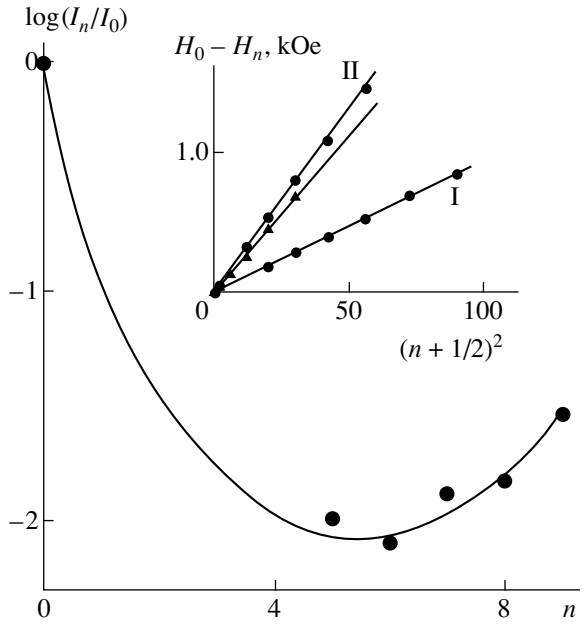

Fig. 2. A plot of the absorption peak intensity I_n versus SW mode number n. The inset shows the dispersion relationships for the peaks in series I and II (Fig. 1) measured for (▲) perpendicular and (●) parallel orientations.

for the spin waves in the range of the magnetic field strengths studied. At first glance, these peaks cannot be related to the first layer either, since their intensities increase with n. Nevertheless, an analysis of the experimental results and the model showed that the observed series of peaks I corresponds to the harmonic SW modes excited in the first layer.

This conclusion is confirmed by the following data. As the angle Θ_H changed from 90° to 33°, the interval of field strengths between the zero-mode peaks decreased. The distance from the observed SW mode peaks of series I to the zero-mode peak of the first layer remained unchanged, while the distance to the zero-mode peak of the second layer gradually increased. As a result, the peaks in series I sequentially disappeared, beginning from those most closely spaced from the zero-mode peak of the second layer. This is evidence that the wavenumbers of SW modes in series I are determined by parameters of the first layer.

More evidence confirming the above conclusion is the character of evolution of the SWR spectrum observed on gradually decreasing the thickness of the second layer. As the layer was gradually removed by chemical etching, the resonance fields corresponding to the peaks of series II changed and the slope of the corresponding dispersion curve increased. At the same time, no such changes were observed during etching for the absorption peaks of series I, except for a gradual decrease in the peak intensity beginning with a certain value (~0.08 μm) of the second layer thickness. The latter effect is explained by the second layer thickness becoming smaller than the penetration depth (path length) l of the spin wave in this layer, which results in a lower degree of spin pinning.

It should be noted that, in a two-layer film with homogeneous layers, the difference of the resonance field strengths between zeroth and nth modes ($H_0 - H_n$) must be the linear function of $(n + 1/2)^2$ (see the inset in Fig. 2). The error in the SW mode numbering toward either side would lead to a deviation of the above difference from linearity. This criterion was used to determine the absorption peak numbers of the SW modes in series I.

The SWR spectrum in the region of series I, including some features such as the absence of absorption peaks with small numbers and the "anomalous" increase in the peak intensity with the SW mode number, can be explained as follows. A relatively large thickness of the first layer results in that distances between the zero-mode peak and the low-mode SW peaks in this layer $\left(H_0 - H_n \approx \frac{2A}{M}\left(n + \frac{1}{2}\right)^2 \frac{\pi^2}{h^2}\ [4]\right)$ are very small, not exceeding the absorption band width $2\Delta H$ (this value is about 115 Oe for the first layer in the structure studied). Therefore, the peaks corresponding to small SW mode numbers, despite a still rather large intensity, superimpose onto the zero-mode peak and are not manifested in the SWR spectrum [6].

As the SW mode number grows, the SW penetration depth l into the second layer and, hence, the variable magnetic moment related to the exponential SW decay, markedly increase (although the total variable magnetic moment of the harmonic SW component in the first layer decreases). Since the magnetization in the second layer is approximately three times that in the first layer, while the decay parameter in the second layer is smaller than that in the first layer, the effect of the SW decay region in I_n becomes dominating.

For a quantitative description of the observed SWR spectrum of a two-layer film, we have calculated the intensities of absorption bands corresponding to various SW modes. For the parallel orientation (in the H_{01}–H_{02} field strength interval), the spin wave was assumed to be harmonic in the first layer and exponentially decaying in the second layer:

$$m_1(z) = B\cos(k_1 z), \quad m_2(z) = C\exp[-k_2''(z - h_1)], \quad (1)$$

where B and C are constant coefficients; k_1 is the wavenumber of the spin wave in the first layer; $k_2'' = (1/l)$ is the wavenumber of the spin wave in the second layer; h_1 and h_2 are the thicknesses of the first and second layer, respectively; and the plane $z = 0$ corresponds to the free surface of the first layer. The wavenumbers k_1 and k_2'' were calculated using the dispersion relationships written for both layers [5]. The set of permissible k_1 values was determined for the boundary exchange

conditions. The SW mode peak intensities were calculated using relationship [7]

$$I_n \sim \frac{\left(\int_0^{h_1} m_1(z)dz\right)^2 + \left(\int_{h_1}^{h_1+h_2} m_2(z)dz\right)^2}{\int_0^{h_1} \frac{\alpha_1}{\gamma_1 M_1} m_1^2(z)dz + \int_{h_1}^{h_1+h_2} \frac{\alpha_2}{\gamma_2 M_2} m_2^2(z)dz}. \quad (2)$$

Figure 2 shows a comparison of the measured and calculated $I(n)$ values. As seen, the agreement between theory and experiment is quite satisfactory. For the first modes, the absorption peak intensity decreases with increasing mode number, but then the effect of the SW decay region in the second layer gradually increases and becomes dominating. This results in the peak intensity of the large SW modes increasing with n. However, the pronounced discrete character of the SWR spectrum in series I is evidence that, despite the dominating contribution of the exponential SW decay region to the total variable magnetic moment, the set of wavenumbers of the excited SW modes is determined by parameters of the first layer (where the harmonic component of the standing spin weave is localized). This is confirmed, in particular, by a linear character of the dispersion relationship observed for the SW modes of series I (Fig. 2).

Acknowledgments. This study was partly supported by the Russian Foundation for Basic Research, project no. 98-02-03320.

REFERENCES

1. C. Kittel, Phys. Rev. **110** (6), 1295 (1958).
2. A. G. Gurevich and G. A. Melkov, *Magnetic Oscillations and Waves* (Nauka, Moscow, 1994).
3. A. I. Akhiezer, V. G. Bar'yakhtar, and S. V. Peletminskiĭ, *Spin Waves* (Nauka, Moscow, 1967; North-Holland, Amsterdam, 1968).
4. A. M. Zyuzin and A. G. Bazhanov, Zh. Éksp. Teor. Fiz. **112** (10), 1430 (1997) [JETP **85**, 778 (1997)].
5. C. H. Wilts and S. Prasad, IEEE Trans. Magn. **MAG-17**, 2405 (1981).
6. A. M. Zyuzin and V. V. Radaĭkin, in *Proceedings of the 13th All-Union School-Seminar "Novel Magnetic Materials for Microelectronics," Astrakhan', 1992*, Part 1, p. 253.
7. N. M. Salanskiĭ and M. Sh. Erukhimov, *Physical Properties and Applications of Magnetic Films* (Nauka, Novosibirsk, 1975).

Translated by P. Pozdeev

Technical Physics Letters, Vol. 27, No. 2, 2001, pp. 150–152. Translated from Pis'ma v Zhurnal Tekhnicheskoĭ Fiziki, Vol. 27, No. 4, 2001, pp. 39–46.

Relativistic Gigawatt BWT Microwave Pulse Duration Increased upon Treating the Slow-Wave Structure Surface with a Low-Energy High-Current Electron Beam

A. V. Batrakov, K. V. Karlik, S. A. Kitsanov, A. I. Klimov, I. N. Konovalov, S. D. Korovin, G. A. Mesyats, G. E. Ozur, I. V. Pegel', S. D. Polevin, D. I. Proskurovskiĭ, and M. Yu. Sukhov

Institute of High-Current Electronics, Siberian Division, Russian Academy of Sciences, Tomsk, 634055 Russia
Institute of Electrophysics, Ural Division, Russian Academy of Sciences, Yekaterinburg, 620219 Russia

Received July 6, 2000

Abstract—A new method of insulator surface treatment, which allows the electric strength of the material to be increased, is proposed and verified. Using this method for treating the slow-wave structure of a relativistic backward wave tube (BWT), the microwave pulse duration was increased from ~6 to ~30 ns at an output BWT radiation power of 3 GW. *© 2001 MAIK "Nauka/Interperiodica".*

The first experiments with a relativistic backward-wave tube (BWT) possessing an output microwave pulse power of 3 GW showed spontaneous limitation of the microwave pulse duration on a level of ~6 ns [1, 2]. Subsequent investigations showed that the microwave pulse width was restricted as a result of the joint action of several factors: (i) appearance of the explosive emission centers on the surface of the slow-wave structure (SWS); (ii) plasma accumulation in the electrodynamic system volume (caused by the explosive emission process, as well as the ion and electron bombardment of the system surface), and (iii) partial absorption of the wave energy by the electron plasma component, leading to an increase in the critical BWT current and the breakdown of oscillations [3]. Thus, the task of increasing the BWT output pulse duration reduces to suppressing or delaying the onset of explosive electron emission in the electrodynamic system of BWT, that is, to increasing the SWS electric strength in the pulsed RF field.

There are several methods of surface treatment that allow the electric strength of an insulator operating in vacuum to be increased [4–6]. Unfortunately, these methods usually do not provide for an effective surface cleaning from impurities and contaminations together with a maximum smoothening of the surface roughness. Moreover, many of these techniques are rather cumbersome and employ expensive equipment.

Previously [7, 8] we proposed a new method of increasing the electric strength of vacuum insulation, which is based on the electrode surface treatment with a pulsed low-energy high-current electron beam (LHEB) of microsecond pulse width. A high energy density (~10–20 J/cm^2) at a relatively short duration of the electron beam pulse provide for the surface treatment involving fusion and partial evaporation of the material. Effectively removing the dielectric inclusions, contaminations, and dissolved gases from the metal and smoothening the electrode surface, this treatment suppresses development of the explosive emission process. The results of our preliminary experiments showed that the treatment leads to a considerable decrease in the prebreakdown current strength and an increase in the electric strength of vacuum gaps. For example, the LHEB processing of stainless steel electrodes followed by a high-voltage training of the system (250 kV, 40 ns, 100 pulses) increased the electric strength of a 1-mm gap up to ~2.2 MV/cm [8].

Recently [9], we developed a special electron source with plasma anode for the LHEB treatment of the surface of the electrodynamic systems of BWTs comprising a set of stainless steel rings. The anode plasma is produced by means of a pulsed Penning's reflection discharge in an inert gas (Ar) [9]. This source differs from the vacuum-spark system employed previously [10] by producing a markedly lower amount of erosion products, which is a principal advantage from the standpoint of our final task. The LHEB source parameters are as follows: electron energy, 20–30 keV; pulse width, 2–4 μs; electron beam energy density, 2–20 J/cm^2; beam diameter, up to 8 cm.

The parts of the electrodynamic system of a BWT were processed in the following order. Upon the cutting process, the rings were electrochemically polished in an orthophosphoric acid solution and rinsed in distilled water and ethanol. The parts to be processed were placed one by one into the working chamber of the electron source for the LHEB treatment (Fig. 1). Prior to the treatment cycle, the working chamber was evacuated to a residual vacuum of ~10^{-5} Torr using a high-

1063-7850/01/2702-0150$21.00

performance oil-diffusion pump with an FM-1 working fluid and a cryotrap. Then the chamber is filled with argon to a pressure of ~5×10^{-4} Torr and the electric discharge is initiated between the Penning cell cathodes (i.e., the explosive-emission cathode, a collector, or the processed part) and a ring anode surrounding the beam aperture, which is provided by applying a voltage pulse (5 kV, 100 μs) to the anode. The discharge current could be varied from 50 to 400 A. The discharge operating in the Penning cell gives rise to an Ar plasma column with an ion density of (1–5) $\times 10^{12}$ cm^{-3}. After ~20 μs of the discharge operation, an accelerating voltage pulse with a leading front width smaller than 10 ns and an amplitude of 25–40 kV was applied to the explosive-emission cathode. Upon excitation of the explosive electron emission, the applied voltage drops across an electric double layer between the cathode and anode plasmas. The electron beam formed in this region escapes through the anode aperture and passes through the plasma to the collector. The beam is transported by an external magnetic field applied in order to maintain the reflection discharge.

The BWT electrodynamic system parts were successively treated by LHEB in two modes with an energy density of 8–10 J/cm^2 (evaporation of an ~0.4-μm-thick surface layer and fusion down to a depth of ~4 μm) and 5–6 J/cm^2 (fusion down to a depth of ~0.3 μm without evaporation). The first regime ensured the removal of the surface inclusions, contaminations, and dissolved gases from the metal, while the second regime produced smoothening of the surface. The irradiation regime (beam energy density) was controlled by changing the pulse generator charging voltage and the magnetic field strength and configuration in the LHEB source. After termination of the LHEB treatment, the part was allowed to cool in an argon atmosphere at a pressure of 50–100 Torr.

The experimental investigation of a 3-cm relativistic BWT operation was performed on a SINUS-7 accelerator with the following electron beam parameters: electron energy, up to 2 MeV; electron beam current, up to 20 kA; pulse duration, 50 ns. The electrodynamic system of the BWT was analogous to that described previously [1, 2]: a mean radius of the corrugated SWS waveguide was 15 mm; the corrugation period and amplitude were 16.1 and 2.1 mm, respectively; and the SWS length was 113 mm. The working electromagnetic wave (TM_{01}) reflected from a 40-mm-long narrowing with a diameter of 23 mm at the cathode end. The electron beam was formed in a coaxial vacuum diode with magnetic isolation. The beam-transporting magnetic field strength was up to 4 T. Electrons were emitted from an explosive-emission graphite edge cathode with a diameter of 19 mm. The radiation was extracted into atmosphere via a horn antenna with an aperture diameter of 50 cm. The microwave output window was made of a 8-mm-thick organic glass.

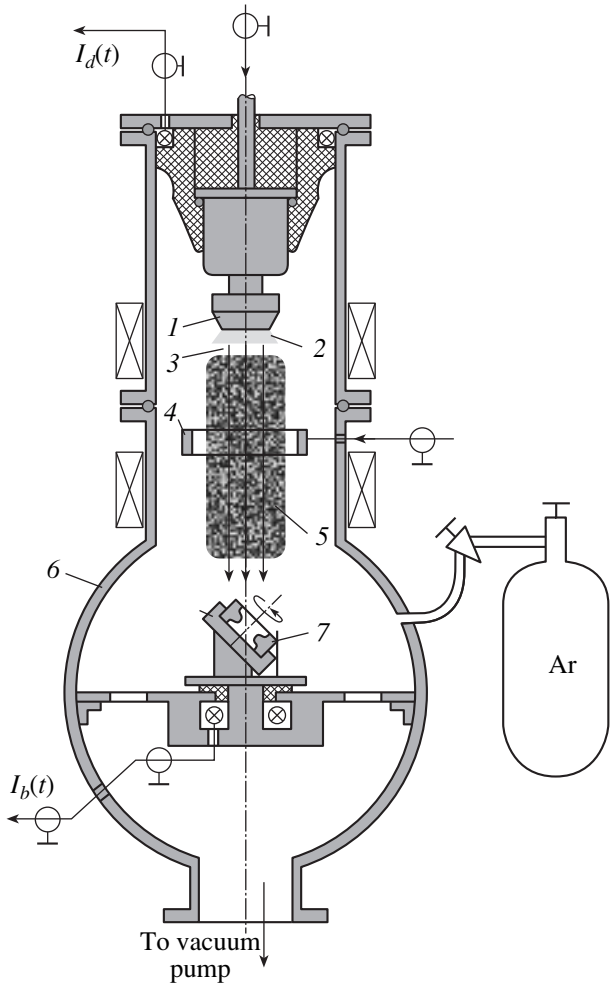

Fig. 1. A schematic diagram illustrating the LHEB surface processing of parts of the electrodynamic system of a BWT: (*1*) explosive-emission cathode; (*2*) cathode plasma; (*3*) electric double layer; (*4*) Penning cell anode; (*5*) anode gas-discharge plasma; (*6*) vacuum chamber; (*7*) processed part.

The BWT output power could be controlled by changing either the beam-transporting magnetic field strength or the electron beam energy density. Figure 2 shows a plot of the microwave pulse width at half height versus radiation power measured under various vacuum conditions (oil-diffusion against oil-free pumping) for the BWT electrodynamic system surface with or without the LHEB treatment. As seen, the state of the electrodynamic system surface significantly affects the microwave pulse duration. In the presence of an absorbed oil film (oil-diffusion pumping), the BWT pulse width limitation was observed for an output power level of ~1 GW. For the electrodynamic system surface treated with LHEB under the oil-free vacuum conditions, no BWT pulse width limitation was observed at an output energy of up to 3 GW (Fig. 3). According to estimates, a maximum electric field strength at the SWS surface and in the narrowing reached up to 1.8 MV/cm.

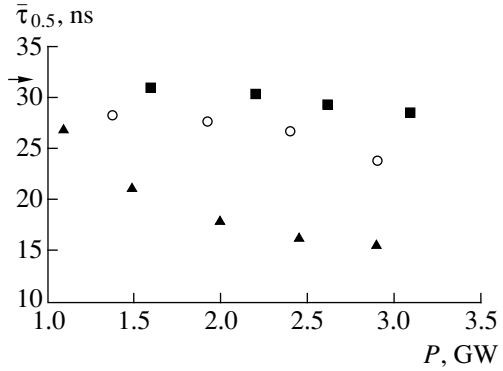

Fig. 2. A plot of the BWT microwave pulse width at half height versus radiation power measured under various vacuum conditions for a BWT with the electrodynamic system surface without (electrochemical finish) or with the LHEB treatment: triangles, electrochemical polishing and oil-diffusion pumping; circles, electrochemical polishing and oil-free vacuum; squares, LHEB and oil-free vacuum. The arrow indicates a decay of the working electron beam pulse.

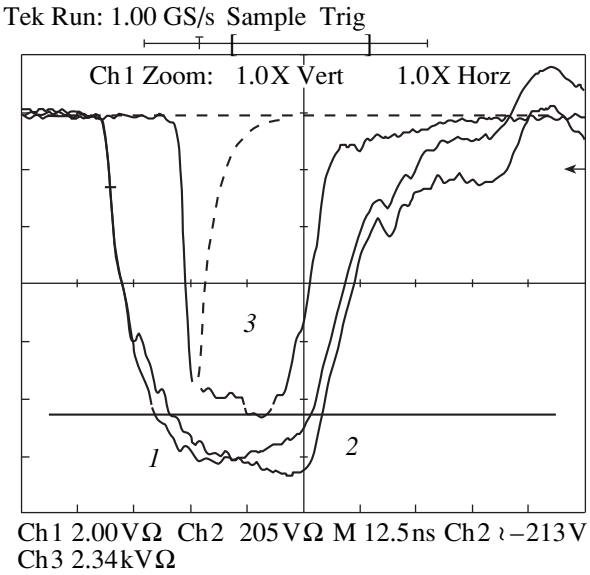

Fig. 3. Oscillograms illustrating the BWT operation: (*1*) diode current; (*2*) electron beam current; (*3*) output microwave power. Dashed line shows the microwave power decay for a BWT with the electrodynamic system not processed by LHEB.

During the experimental system operation, we have observed the effect of the BWT electrodynamic system "training" in the intense RF field, which was similar to that reported in [3]. According to this, the output pulse duration was initially 20 ns (which is greater than the pulse width observed in [1, 2]) and increased (over a series of 15–20 pulses generated without admitting air to the working chamber) to 29 ns (Fig. 3). No significant changes in the pulse duration were observed in the subsequent series of 200 pulses, with the mean-square scatter in the pulse width not exceeding 5%. The energy in the microwave pulse measured using a calorimeter was as high as 90 J.

It should be noted that examination of the BWT electrodynamic system surface operated under the conditions of maximum electric field strength (in the regions of narrowing and the first SWS corrugation) showed evidence of erosion, but the number of craters per unit surface was 2–3 times smaller than that in the case of a surface not treated by the low-energy high-current electron beam.

Thus, a 3-cm relativistic BWT with the electrodynamic system surface treated by LHEB under oil-free vacuum conditions is capable of producing 3-GW output microwave pulses with a duration of up to ~30 ns without evidence of a spontaneous limitation of the pulse width. These results provide additional evidence for the hypothesis that the phenomenon of spontaneous limitation of the nanosecond output pulses of super-high-power microwave generators is predominantly related to the explosive emission effects.

Acknowledgments. The work was supported by the European Office for Aerospace Research and Development (EOARD), contract no. F61775-98-WE080.

REFERENCES

1. A. V. Gunin, S. A. Kitsanov, A. I. Klimov, *et al.*, Izv. Vyssh. Uchebn. Zaved., Fiz., No. 12, 84 (1996).
2. A. V. Gunin, A. I. Klimov, S. D. Korovin, *et al.*, IEEE Trans. Plasma Sci. **26** (3), 326 (1998).
3. S. D. Korovin, G. A. Mesyats, I. V. Pegel, *et al.*, in *Proceedings of the International University Conference "Electronics and Radiophysics of Ultra-High Frequencies" (UHF-99), St. Petersburg, May 24–28, 1999*, p. 229.
4. R. V. Latham, *High-Voltage Vacuum Insulation* (Academic, London, 1981).
5. G. A. Mesyats and D. I. Proskurovsky, *Pulsed Electrical Discharge in Vacuum* (Springer-Verlag, Berlin, 1989).
6. G. A. Mesyats, *Ectons in Vacuum Discharge: Breakdown, Spark, Arc* (Nauka, Moscow, 2000).
7. A. V. Batrakov, A. B. Markov, G. E. Ozur, *et al.*, IEEE Trans. Dielectr. Electr. Insul. **2**, 237 (1995).
8. A. V. Batrakov, D. S. Nazarov, G. E. Ozur, *et al.*, IEEE Trans. Dielectr. Electr. Insul. **4** (6), 857 (1997).
9. G. E. Ozur, D. I. Proskurovskiĭ, D. S. Nazarov, and K. V. Karlik, Pis'ma Zh. Tekh. Fiz. **23** (10), 42 (1997) [Tech. Phys. Lett. **23**, 393 (1997)].
10. D. S. Nazarov, G. E. Ozur, and D. I. Proskurovskiĭ, Izv. Vyssh. Uchebn. Zaved., Fiz., No. 3, 100 (1994).

Translated by P. Pozdeev

Technical Physics Letters, Vol. 27, No. 2, 2001, pp. 153–154. Translated from Pis'ma v Zhurnal Tekhnicheskoĭ Fiziki, Vol. 27, No. 4, 2001, pp. 47–51.

Multiparticle Tunneling during Field Electron Emission from $Bi_2CaSr_2Cu_2O_8$

V. I. Maslov

St. Petersburg State University of Telecommunications, St. Petersburg, 191065 Russia

Received September 28, 2000

Abstract—An analysis of data on the experimental statistics of the field electron emission (FEE) from an oxide superconductor of the $Bi_2CaSr_2Cu_2O_8$ system reveals the multielectron tunneling effect. The spectral curves and statistical data obtained under various experimental conditions are considered, and possible mechanisms of the multiparticle tunneling are discussed. © *2001 MAIK "Nauka/Interperiodica".*

The physics of tunneling phenomena in superconductors gives unique information concerning various properties of these materials in both superconducting and normal states. This is related, in particular, to the fact that electrons involved in the field electron emission (FEE) are tunneling into vacuum without external excitation.

We have studied the correlation effects for FEE by determining the numbers of various elementary emission events and the distribution of these events with respect to their occurrence (number)—that is, by measuring the FEE statistics [1, 2]. Using an experimental setup described in [1], we have previously studied the FEE statistics in tungsten and niobium (a classical superconductor) at a liquid helium temperature [3]. In both normal and superconducting states, these metals showed (to within a 99.9% precision) only one-electron emission events. The results obtained in a series of studies showed that the one-electron FEE is also inherent in the usual (non-superconducting) metals in a broad range of temperatures and current densities [4].

With the discovery of high-temperature superconductors (HTSCs), the probability of observing correlated electrons tunneling from a superconducting condensate must increase. This is related, first, to a smaller coherent length and, second, to a greater energy gap typical of HTSCs [5]. The first results on the study of FEE statistics in HTSC metal ceramics of the Y–Ba–Cu–O system were reported in [6], where the phenomenon of multiparticle tunneling from oxide superconductors was discussed.

In this study, the experiments were performed with electron emitters made of a bismuth compound with the formula $Bi_2CaSr_2Cu_2O_8$, characterized by a critical temperature of 110 K. The emitter tips were mechanically sharpened and the samples were mounted in clamps of a cathode unit.

The FEE experiments were carried out in a setup analogous to that described previously [1]. The first experiments were conducted with a multichannel pulse analyzer and then the system was modified so as to use an analog-to-digital (ADC) converter linked to a personal computer. The computer-controlled setup allowed the experimental procedure to be automated and improved the quality of data processing.

The all-glass working unit of the experimental setup was evacuated to a vacuum of not worse than 5×10^{-7} Pa. The probe current (i.e., the flux of electrons) reaching a detector was varied from 100 to 7000 electrons per second. This corresponded to a total FEE current variation in a range from 10^{-16} to 10^{-10} A, because the electron beam extracted through the probing hole was collected from both strongly and weakly emitting cathode regions.

The emission pattern exhibited a structureless character, representing separate spots of different size. A special feature of the FEE from emitters of the Bi–Ca–Sr–Cu–O system is a considerable (more than tenfold) decrease in the current fluctuations at temperatures below the critical temperature. Above this temperature, the current fluctuations reached tens of percent.

It was established that FEE from most of the HTSC sample surface had a one-electron character. However, in contrast to the Y–Ba–Cu–O system, a multielectron tunneling from both weakly emitting regions and bright areas was observed as well. Some characteristic spectra of the FEE statistics from $Bi_2CaSr_2Cu_2O_8$ are presented in Figs. 1a and 1b.

In the total flux, the groups of two electrons accounted for up to several percent (which is two orders of magnitude higher than the Poisson superposition frequency). A fraction of the groups of three electrons amounted to a few tenths of a percent, and the groups of four electrons were still more seldom–their proportion not exceeding 0.01%–but even this level was 100 times greater than the sensitivity level with respect to the four-electron emission events.

1063-7850/01/2702-0153$21.00 © 2001 MAIK "Nauka/Interperiodica"

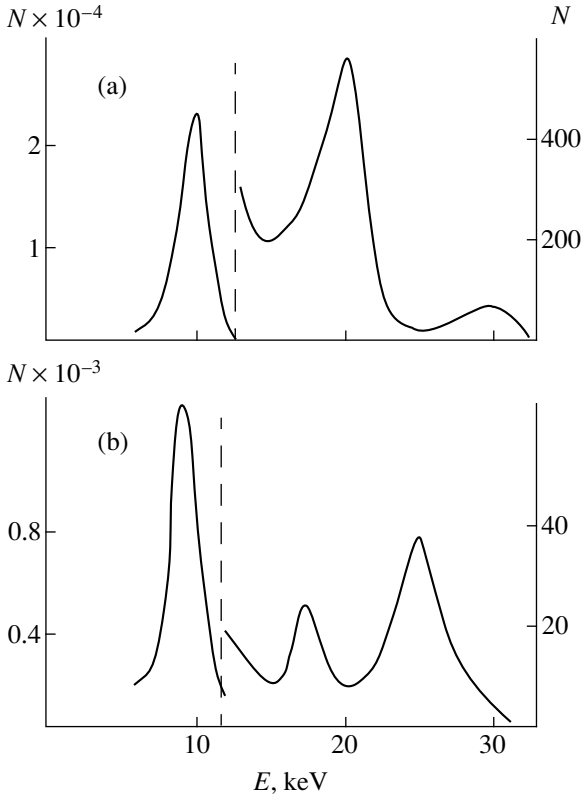

Fig. 1. The typical spectra of FEE statistics for (a) weakly and (b) strongly emitting spots of $Bi_2CaSr_2Cu_2O_8$ emitters.

Most frequently, the intensity of multiparticle emission observed in our experiments monotonically decreased with the group multiplicity, but some emitter spots exhibited an exception to this rule: Fig. 1b shows a FEE spectrum where the three-electron flux intensity is greater than the two-electron component.

An analysis of the FEE spectra showed that the shapes of the multielectron emission peaks is close to Gaussian. This leads to an important conclusion that the electron correlation time in a group is much smaller than the probing pulse duration used in the measurements (~4 μs). However, some emitter spots exhibited multielectron emission events with a steplike peak shape that corresponds to an electron correlation time comparable to the working pulse duration.

The character of the FEE statistics did not change when the sample passed from normal to superconducting state and back (for the registration parameters indicated). This fact is evidence that the multielectron tunneling is related to the intrinsic properties of the HTSC compound.

Previously [6], we explained the multiparticle effect in terms of a model assuming an avalanche multiplication of free electrons in the dielectric layers of metal ceramics under the action of a penetrating electric field. However, a joint analysis of the results obtained in this study and those reported in [6] rejects this mechanism as improbable. First, if this mechanism were operative, the "hot" electrons emitted at voltages far from the breakdown level would lead to an inverse temperature dependence of the current [7], which is not the case in our experiment (showing rather the opposite behavior). Second, this mechanism is inconsistent with the nonmonotonic character of some spectra (Fig. 1b).

Taking into account that the yttrium and bismuth oxide superconductors possess a hole conductivity, we may suggest that the multiparticle effects are related to the electron scattering on the hole centers. Also possible is the multielectron tunneling from strongly localized states.

A correct interpretation of the multielectron tunneling phenomenon requires additional experiments, in particular, those involving the electron beam rejection technique [2].

Acknowledgments. The author is grateful to V.V. Monakhov for the development of the computer software and to T.Yu. Chemekov for kindly providing the samples.

REFERENCES

1. V. I. Maslov, G. N. Furseĭ, A. V. Kocheryzhenkov, and N. P. Afanas'eva, Prib. Tekh. Éksp., No. 5, 133 (1987).
2. V. I. Maslov, G. N. Furseĭ, and A. V. Kocheryzhenkov, Prib. Tekh. Éksp., No. 2, 145 (1990).
3. A. V. Kocheryzhenkov, V. I. Maslov, and G. N. Furseĭ, Fiz. Tverd. Tela (Leningrad) **29** (8), 2471 (1987) [Sov. Phys. Solid State **29**, 1421 (1987)].
4. G. N. Fursey, A. V. Kocheryzhenkov, and V. I. Maslov, Surf. Sci. **246**, 365 (1991).
5. N. M. Plakida, *High-Temperature Superconductors* (Mezhdunarodn. Programma Obrazovaniya, Moscow, 1996), p. 288.
6. G. N. Furseĭ, A. V. Kocheryzhenkov, V. I. Maslov, and A. P. Smirnov, Pis'ma Zh. Tekh. Fiz. **14** (20), 1853 (1988) [Sov. Tech. Phys. Lett. **14**, 804 (1988)].
7. *Non-Incandescent Cathodes*, Ed. by M. I. Elinson (Sov. Radio, Moscow, 1974), p. 336.

Translated by P. Pozdeev

Technical Physics Letters, Vol. 27, No. 2, 2001, pp. 155–156. Translated from Pis'ma v Zhurnal Tekhnicheskoĭ Fiziki, Vol. 27, No. 4, 2001, pp. 52–56.

The Field-Induced Ion Evaporation Effect in the Bipartition of Charged Droplets

A. I. Grigor'ev

Yaroslavl State University, Yaroslavl, 150000 Russia

e-mail: grig@uniar.ac.ru

Received September 18, 2000

Abstract—A physical mechanism explaining the formation of a cluster phase during the electrostatic bipartition of droplets unstable with respect to their own charge is suggested. The mechanism assumes the possibility of the field-induced evaporation of ions from the surface of droplets of a micron size formed in the final stage of a droplet decay cascade. © *2001 MAIK "Nauka/Interperiodica".*

Investigation of the physical laws governing the electrodispersion of liquids in the case of the development of the free surface instability with respect to intrinsic or induced electric charge is of considerable importance both from a theoretical standpoint and for numerous technological applications [1, 2]. Of special interest is the still unsolved problem concerning the determination of a distribution function with respect to size and charge of submicron droplets and clusters formed in the course of the electrodispersion process. According to the existing notions [3, 4], a series of decay cascades developed in strongly charged droplets emitted from the surface of a charged liquid terminates when the smallest droplet size reaches micron level. This is explained by the effect of viscosity that becomes significant when

$$\mu \equiv \nu(\rho_m/R\sigma)^{1/2} \geq 1. \quad (1)$$

Here, ν is the kinematic viscosity coefficient, R is the droplet radius, ρ_m is the liquid density, and σ is the surface tension coefficient.

Once the condition (1) is satisfied, which takes place for the droplets of submicron dimensions [1, 3, 4], a strongly charged droplet unstable with respect to its own surface charge exhibits a decay (bipartition) with the formation of two smaller droplets of comparable size, each of the two being stable. In liquid-metal ion sources and the mass spectrometers (employing the electrodispersion effect) used for the analysis of thermally unstable and nonvolatile liquids, the droplets and clusters (forming the ion–cluster–droplet flows) possess dimensions essentially on a submicron level. Apparently, the submicron fraction formation in these systems proceeds with a considerable contribution of the phenomenon of field-induced evaporation of clustered (solvated) ions. This phenomenon takes place with an electric field strength of $E \approx 1$ V/nm at the charged surface, as was indicated in application to mass spectrometry [5].

The concept assuming a key role of the field-induced ion evaporation in the submicron droplet fraction formation was criticized [6] because (i) the agreement between theory and experiment for a system of droplets with a fixed particle size (0.8 nm) was achieved for very high field strength ($E \sim 10$ V/nm) and (ii) there was a discrepancy between theory and experiment in the values of cation and anion current densities in the ion beam. An alternative concept of the ion–cluster beam formation formulated in [7, 8] was based on the field-induced evaporation of clustered ions from vertices of the emitting protrusions formed on the charged liquid surface in the final stage of the instability development. However, we believe that the mechanism proposed in [7, 8] does not take into account the aforementioned restriction on the curvature of emitting vertices, related to the effect of the liquid viscosity. Anyhow, the field-induced evaporation must play a significant role in the formation of a submicron fraction in the ensemble of droplets formed in the course of electrodispersion.

1. Let us consider the possible evolution of a droplet with micron radius carrying a limiting charge Q (in terms of the Rayleigh stability) related to the particle radius R by the formula $Q^2/16\pi\sigma R^3 = 1$. This droplet is unstable with respect to infinitesimal perturbation in amplitude of the fundamental mode of the capillary oscillations. On losing stability, the droplet elongates to acquire a spheroidlike shape. Having $\mu \approx 1$ and possessing a viscosity considerably damping the high-mode instability development during the eccentricity growth, this droplet cannot release the excess charge (as it does in the case of $\mu \ll 1$) [3] by emitting strongly charged droplets of a size two orders smaller. Therefore, the spheroidal deformation of the droplet will increase until either the particle breaks in two or the field strength at the vertex reaches a level of $E \approx 1$ V/nm corresponding to the onset of the field-induced ion evaporation.

1063-7850/01/2702-0155$21.00

The characteristic time τ_0 of the spheroidal deformation buildup is determined by the liquid viscosity ν (or by the μ value). According to [9], the quantity τ_0 is a simple linear function of ν (or μ):

$$\tau_0 = a + b\mu \equiv R^2\left(\frac{\rho}{2\zeta_0\sigma}\right)^{1/2} + \nu\frac{\rho R^{5/2}}{34\zeta_0^{3/2}\sigma}, \qquad (2)$$

where ζ_0 is the amplitude of the initial virtual deformation (for an initial deformation of a thermal nature, $\zeta_0 \sim 0.1$ nm [9]). For a water droplet with $R = 1$ μm, $\rho = 10^3$ kg/m^3, and $\sigma = 0.07$ N/m, equation (2) readily yields

$$\tau_0 \cong (5 \times 10^{-6} + \nu \times 3 \times 10^{-3})\text{s} \sim 10\ \mu\text{s}.$$

The electric field strength at the surface of a charged spheroid is given by a well-known expression [10]

$$E_c = \frac{Q}{ab^2}\left(\frac{x^2}{a^4} + \frac{\rho^2}{b^4}\right)^{-1/2}.$$

The maximum surface charge density is observed at the spheroid vertices ($x = \pm a$; $\rho = 0$):

$$E = Q/b^2 = Q/R^2(1 - e^2)^{1/3}.$$

The latter relationship is conveniently written in the following form:

$$E/E_0 = (1 - e^2)^{-1/3},$$

where $E_0 = Q/R^2$ is the field strength of the intrinsic charge at the surface of the initial spherical droplet. As is readily seen, the field strength E at the vertices of the spheroidal droplet with large eccentricity may significantly exceed E_0. For a droplet possessing a limiting charge according to Rayleigh, the latter quantity is

$$E_0 = (Q/R^2) = (16\pi\sigma/R)^{1/2}. \qquad (3)$$

For a water droplet, this formula yields $E_0 \approx 0.2$ V/nm. If the square eccentricity of a spheroidal water droplet becomes equal to $e^2 = 0.92$, the field strength at the vertices is 1 V/nm and the droplet will lose the charge by the field-induced ion evaporation mechanism. Note, however, that the field strength $E = 1$ V/nm is not a critical threshold: the field-induced evaporation of ions may take place, albeit at a lower intensity, at smaller E values.

2. The characteristic time τ^* during which a droplet loses its charge by means of the field-induced evaporation of clustered ions from the charged surface can be estimated (by the order of magnitude) using the formula [6, 7]

$$\tau^* \sim (\beta\omega_0)^{-1}, \quad \beta = \exp\left[-\frac{\Delta G - N_A(z^3q^3E)^{1/2}}{R_0T}\right], \qquad (4)$$

where ω_0 is the ion vibration frequency on the droplet surface; ΔG is a change in the system enthalpy upon the ion passage from liquid to vacuum; β is the probability for an ion to be field-evaporated; N_A is the Avogadro number; q is the electron charge; z is the ion charge; E is the electric field strength at the droplet surface; R_0 is the universal gas constant; and T is the absolute temperature. As can be readily seen from this expression, the τ^* value is quite small (on the order of "molecular" times) due to a rather large value of ω_0 even for the field-induced ion evaporation probability markedly below unity. In any case, the τ^* value is markedly smaller than the characteristic time τ_0 of the spheroidal deformation buildup determined by formula (2). Upon partly losing its charge by means of the field-induced ion evaporation, the parent droplet will regain a spherical shape. The subsequent thermal evaporation at a constant charge will result in that the droplet would satisfy the Rayleigh instability criterion again, elongate to acquire a spheroidal shape, and release the charge by means of the field-induced ion evaporation. This process will proceed until complete evaporation of the droplet.

Conclusion. A submicron phase may form upon the electrostatic decay of strongly charged droplets or in cluster–cluster–droplet beams of mass spectrometers (employing the electrodispersion effect) used for the analysis of thermally unstable and nonvolatile liquids as a result of the field-induced ion evaporation from the surface of droplets of a micron size, the fundamental oscillation mode of which is unstable in the sense of the Rayleigh instability criterion with respect to intrinsic charge.

REFERENCES

1. A. I. Grigor'ev and S. O. Shiryaeva, Izv. Ross. Akad. Nauk, Mekh. Zhidk. Gaza, No. 3, 3 (1994).
2. A. I. Grigor'ev, Zh. Tekh. Fiz. **70** (5), 22 (2000) [Tech. Phys. **45**, 543 (2000)].
3. A. I. Grigor'ev and S. O. Shiryaeva, Zh. Tekh. Fiz. **61** (5), 19 (1991) [Sov. Phys. Tech. Phys. **36**, 258 (1991)].
4. A. I. Grigor'ev and A. É. Lazaryants, Zh. Vychisl. Mat. Mat. Fiz. **32** (6), 929 (1992).
5. J. V. Iribarne and V. A. Thomson, J. Chem. Phys. **64** (6), 2287 (1976).
6. N. B. Zolotoĭ, G. V. Karpov, and V. E. Skurat, Zh. Tekh. Fiz. **58** (2), 315 (1988) [Sov. Phys. Tech. Phys. **33**, 193 (1988)].
7. N. B. Zolotoĭ, Zh. Tekh. Fiz. **65** (11), 159 (1995) [Tech. Phys. **40**, 1175 (1995)].
8. N. B. Zolotoĭ and G. V. Karpov, Dokl. Akad. Nauk **348** (3), 336 (1996).
9. S. O. Shiryaeva, Zh. Tekh. Fiz. **70** (9), 30 (2000) [Tech. Phys. **45**, 1128 (2000)].
10. L. D. Landau and E. M. Lifshitz, *Course of Theoretical Physics*, Vol. 8: *Electrodynamics of Continuous Media* (Nauka, Moscow, 1982; Pergamon, New York, 1984).

Translated by P. Pozdeev

Technical Physics Letters, Vol. 27, No. 2, 2001, pp. 157–159. Translated from Pis'ma v Zhurnal Tekhnicheskoĭ Fiziki, Vol. 27, No. 4, 2001, pp. 57–61.

A Change in the Microwave Radiation Reflection upon a Dielectric–Metal Transition in Vanadium Dioxide

B. M. Gorelov, K. P. Konin, V. V. Koval', and V. M. Ogenko

Institute of Surface Chemistry, National Academy of Sciences of Ukraine, Kiev, Ukraine

e-mail: user@surfchem.freenet.kiev.ua

Received September 7, 2000

Abstract—The microwave radiation reflection coefficient of pure vanadium dioxide and its compositions with dielectrics exhibits a jumplike change upon a sample transition from dielectric into metallic state. The reflection coefficient may either increase or decrease, the sign and magnitude of the effect depending on the electromagnetic field frequency and the sample thickness. The phenomenon is explained by changes in the wave interference conditions upon the phase transition. *© 2001 MAIK "Nauka/Interperiodica".*

As is known [1–3], the phase transition of vanadium dioxide from dielectric to metallic state at ~68°C is accompanied by a jumplike increase in the reflection coefficient (R) of this material for electromagnetic radiation in the IR wavelength range. The jump in the R value is related to a change the complex dielectric permittivity $\varepsilon = \varepsilon_1 - i\varepsilon_2$ by the following expression (for the normal incidence angle) [4]:

$$R = \left|(\sqrt{\varepsilon_1} - \sqrt{\varepsilon_2})/(\sqrt{\varepsilon_1} + \sqrt{\varepsilon_2})\right|^2. \qquad (1)$$

The phenomenon is explained by a sharp growth in the conductivity $\sigma(T) = \omega\varepsilon_2(T)/4\pi$ and the imaginary part (ε_2) of the permittivity with increasing temperature T (ω is the wave frequency), provided that the real part of ε is sufficiently small and $\varepsilon_1 \ll \varepsilon_2$.

In the SHF (microwave radiation) range of the spectrum, where the wavelength is comparable to a sample thickness, the behavior of R during the dielectric–metal transition may depend on both the radiation frequency and the sample thickness. For example, the reflection of a wave with $\omega = \pi c/(2l)$ from a quarter-wave nonmagnetic sample with the thickness $l = \lambda/4 = \lambda_0/(4\sqrt{\varepsilon_1})$ (λ_0 and λ are the wavelengths in the free space and in the sample, respectively, and c is the speed of light) is determined by interference of the waves reflected from two boundary surfaces: $J_0\cos(wt + \varphi)$ and $J_0 e^{-2\alpha ml}\cos\left[\omega\left(t + \dfrac{\lambda_0 m}{2c\sqrt{\varepsilon_1}}\right) + \varphi\right]$, where J_0 is the incident wave intensity, $\alpha = 4\pi\sigma/(nc)$ is the absorption coefficient, n is the index of refraction, and m is an integer. Thus, the reflection depends on ε_1, α, and l—the sample parameters. Being accompanied by a jumplike change in ε_1 and α values, the phase transition changes the conditions of superposition of the reflected waves, namely, the differences of their phases $\Delta = \lambda_0\pi m/(4l\sqrt{\varepsilon_1})$ and intensities. For this reason, the phase transition in a quarter-wave ω sample may lead, depending on the Δ value, to either a decrease (for $\Delta = \pi$) or an increase ($\Delta = 0$) in the reflection coefficient for the same ω.

The purpose of this work was to study a change in the reflection of SHF electromagnetic waves upon the dielectric–metal transition in a quarter-wave sample of vanadium dioxide. The experiments were performed with the samples made of a disperse vanadium powder (particle size, 60–80 μm; relative powder density, 0.4–0.6) prepared by grinding polycrystalline VO_2. The conductivity of the VO_2 powder was 5–7 $(\Omega\ \text{cm})^{-1}$ at room temperature and exhibited a jumplike increase to 10^4 $(\Omega\ \text{cm})^{-1}$ at T = 68–72°C. We have also studied the compositions of VO_2 with a dielectric (styrene–butadiene rubber, SBR) with various degrees of filling $f = V/V_0 = 0.2$–0.7, where V and V_0 are the volumes of VO_2 inclusions and the polymer matrix, respectively. The reflection coefficient was measured in the 8–12 GHz frequency range by a short-circuit line technique using a standing-wave meter of the Ya2R-67 type [4].

Figure 1 shows typical plots of the standing-wave ratio R versus temperature T for VO_2 samples of various thicknesses. For a 3.0-mm-thick sample measured in the 10.0–12.0 GHz frequency interval, the dielectric–metal transition is manifested by a jumplike increase of R for ω = 10.0–10.8 GHz or by a sharp drop of R for ω = 12.0 GHz. At a frequency of ω = 8.2 GHz, the VO_2 transition to the metallic state at 68–72°C is not manifested (Fig. 1a).

It should be noted that a VO_2 layer with a thickness of l = 3.0 mm produces a maximum attenuation of the 10.0 GHz radiation at T = 21°C (Fig. 2, curve *1*). In a

sample with the thickness corresponding to quenching of the radiation with ω = 11.0 GHz in the dielectric state (Fig. 2, curve *2*), the behavior of *R* upon the phase transition in a 10.0–12.0 GHz interval is reversed: the reflection coefficient sharply drops at ω = 10.0 GHz. As the microwave frequency ω increases, the drop magnitude decreases. The *R* value gradually decreases at ω = 10.4 GHz and shows a jump at ω = 11.1–12.0 GHz (Fig. 1b). No jumps in *R* are observed for ω = 8.0–9.2 GHz.

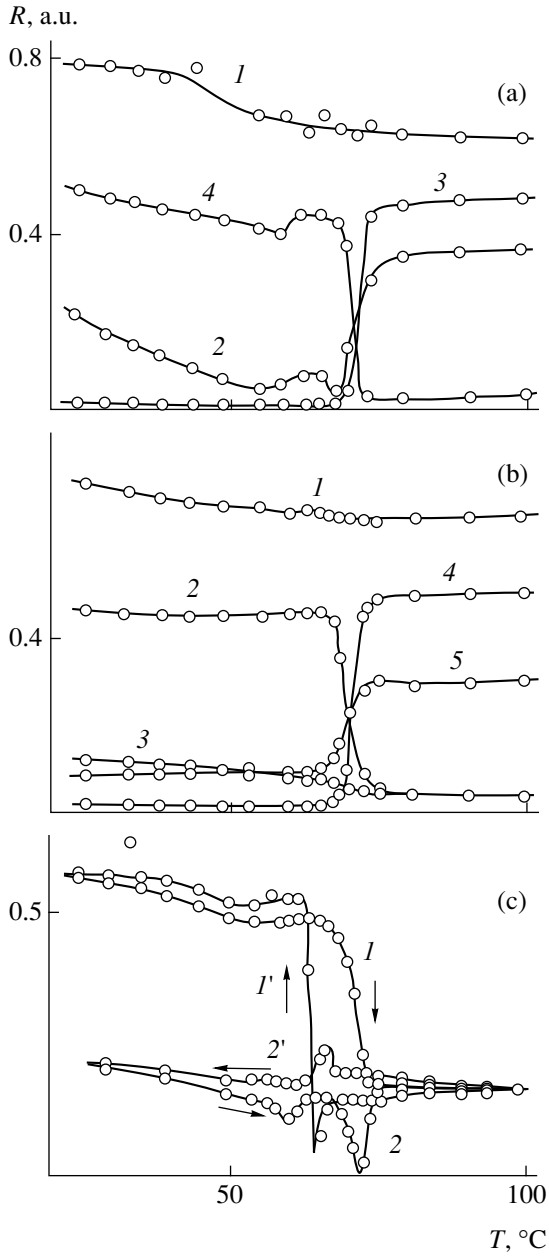

Fig. 1. Typical plots of the reflection coefficient (standing-wave ratio) *R* versus temperature *T* measured at various frequencies (a, b) for vanadium dioxide of different thicknesses *l* = 3.0 mm (a) [ω = 8.2 (*1*), 10.0 (*2*), 10.8 (*3*), 12.0 GHz (*4*)] and 2.3 mm (b) [ω = 8.2 (*1*), 10.0 (*2*), 10.4 (*3*), 11.1 (*4*), 12.0 GHz (*5*)] and (c) for a VO_2–SBR composition with *f* = 0.2 and *l* = 2.5 mm [ω = 8.2 (*1*, *1*') and 10.3 GHz (*2*, *2*') on (*1*, *2*) heating and (*1*', *2*') cooling.

Analogous changes in the behavior of *R*(ω) were observed for the VO_2–SBR compositions, the permittivity of which is determined by the *f* value [5]:

$$\tilde{\varepsilon} = \varepsilon + \frac{3f\tilde{\varepsilon}(\varepsilon - \varepsilon_m)}{(2\tilde{\varepsilon} + \varepsilon) - f(\varepsilon - \tilde{\varepsilon})}, \qquad (2)$$

where ε_m is the permittivity of the dielectric component (SBR). For $f \le 0.3$, the behavior of *R*(*T*) on heating and cooling may differ. An example is offered by a VO_2–SBR sample with *f* = 0.2 and *l* = 2.5 mm, where the *R*(*T*) curves measured at ω = 8.2 GHz exhibit a similar character, while the curves measured at ω = 10.3 GHz reveal a difference in the *R* variation with increasing and decreasing temperature *T* (Fig. 1c).

Thus, the reflection coefficient of vanadium dioxide and its compositions with dielectrics is a function of the electromagnetic radiation frequency and sample thickness. Depending on these parameters, the *R* value upon the phase transition of VO_2 from a dielectric to metallic state may increase or decrease in a jumplike manner or remain unchanged. This behavior of *R*(ω, *T*) can be explained by a change in the conditions of interference of the reflected waves as a result of variation of the real part of the dielectric permittivity. Depending on the sample thickness (for the same frequency), the conditions change from quenching ($\Delta \simeq \pi$) to amplification ($\Delta = 0$) or vice versa. At the same time, the phase difference Δ exhibits small variations at frequencies not

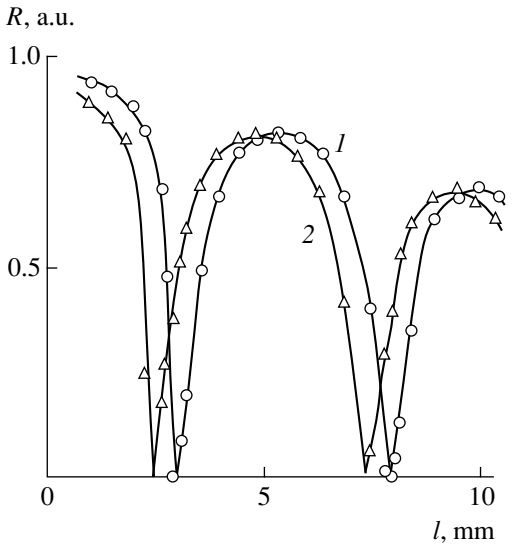

Fig. 2. The plots of room-temperature reflection coefficient versus sample thickness for vanadium dioxide measured at a frequency of (*1*) 10.0 and (*2*) 11.0 GHz.

corresponding to the interference extrema in the dielectric or metallic state of vanadium oxide.

REFERENCES

1. A. A. Bugaev, B. P. Zakharchenya, and F. A. Chudnovskiĭ, *Metal–Semiconductor Phase Transition and Its Applications* (Nauka, Leningrad, 1979).
2. F. A. Chudnovskiĭ, Metal–Semiconductor Phase Transition in Vanadium Dioxide, in *Readings in Memory of A. F. Ioffe (1987–1988)* (Nauka, Leningrad, 1988), pp. 58–65.
3. M. Imada, A. Fujimori, and Y. Takura, Rev. Mod. Phys. **70** (4), 1039 (1998).
4. Yu. K. Kovneristyĭ, I. Yu. Lazarev, and A. A. Ravaev, *Materials Absorbing Microwave Radiation* (Nauka, Moscow, 1982).
5. L. G. Grechko, V. V. Motrich, and V. M. Ogenko, *Surface Modes in Small Particles of Inhomogeneous Dispersed Media* (A Preprint of the Institute of Theoretical Physics), ITF (Kiev, 1990).

Translated by P. Pozdeev

Technical Physics Letters, Vol. 27, No. 2, 2001, pp. 160–163. Translated from Pis'ma v Zhurnal Tekhnicheskoĭ Fiziki, Vol. 27, No. 4, 2001, pp. 62–71.

A New Integral Equation for Calculating Thin Electric Vibrators

V. A. Neganov, M. G. Kornev, and I. V. Matveev

State Academy of Telecommunications and Informatics, Russia

e-mail: neganov@mail.ru

Received July 11, 2000; in final form, September 20, 2000

Abstract—A new singular integral equation describing the current distribution in a thin electric vibrator is derived, which provides for a mathematically correct calculation of this radiating system. © *2001 MAIK "Nauka/Interperiodica".*

Introduction. The calculations of thin electric vibrators are usually based on solving the Pocklington–Harrington integrodifferential equations and the Hallen integral equation [1–4]. Most widely used is the method of moments and its modifications determined by selection of the basis set functions. The main disadvantage of this approach, in our opinion, consists in that the aforementioned integral equations are solved by replacing the initial singular kernels (written in an implicit form) by regular ones (of the Fredholm type). As a result, we arrive at a set of Fredholm integral equations of the first kind representing an ill-posed problem [5]. In addition, there appears an open question of verifying the correctness of solutions and establishing the adequacy of the solution to the initial physical problem. Eminov [6] introduced a new class of functions (called the eigenfunctions of an integrodifferential operator) for solving these problems, but the numerical solution algorithm based on these functions turns out to be highly complicated.

This study is a continuation of our previous work [7, 8] where a mathematical apparatus of the theory of singular integral equations, developed for the description of the strip–slit waveguide structures operating in the SHF and EHF ranges [9–11], was used to obtain a set of inhomogeneous singular integral equations for a derivative of the longitudinal coordinate with respect to the surface current density in a vibrator. A disadvantage of these equations was that the inhomogeneous terms in their right-hand parts contained singularities of the first kind complicating the regularization process.

The approach proposed in this paper principally differs from that used in [8] by obtaining a new singular integral equation for the surface current density with a continuous right-hand part.

Problem formulation. Generalized Hallen integral equation. Let us consider a thin conductor with a length of $2L$ and a radius of a, excited at a break point (i.e., in the gap) with a signal from an RF generator (Fig. 1). In deriving the equations describing this system, we will proceed from the conventional model of thin electric vibrator ($a \ll L, \lambda$), according to which the longitudinal electric current density η_z^e (with an equivalent magnetic current density in the gap) is replaced by an infinitely thin longitudinal electric current thread $I_z(z) = 2\pi a \eta_z^e(z)$. It is assumed that the current is continuous in the gap region and becomes zero at the vibrator ends. The edge currents are ignored. The electric field component E_z generated by the current thread on the surface of a cylinder $\rho = a (z \in [-L, L])$ becomes zero everywhere except for the gap region with a width of $2b$, where this component is taken equal to the external field strength $E^0(z)$.

Within the framework of the physical model adopted, the radiation field of the vibrator (indepen-

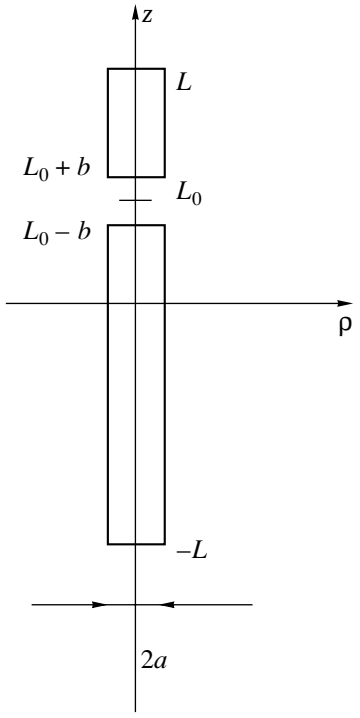

Fig. 1. A schematic diagram of the electric vibrator.

1063-7850/01/2702-0160$21.00 © 2001 MAIK "Nauka/Interperiodica"

dent of the angle φ) is described by the Pocklington equation [1–4]

$$\left(\frac{d^2}{dz^2}+\gamma^2\right)\int_{-L}^{L}\frac{I_z(z')}{R}e^{-i\gamma R}dz = -i\omega\varepsilon_0\varepsilon E^0, \qquad (1)$$

where $R = \sqrt{(z-z')^2+a^2}$; $\gamma^2 = k^2\varepsilon\mu$; $k = \omega/c$ is the wavenumber; ε and μ are the relative dielectric permittivity and magnetic permeability of the space around the vibrator, respectively; and ε_0 is the dielectric permittivity of vacuum.

Let us consider relationship (1) as a second-order differential equation for the unknown function (*z*-component of the vector potential) introduced by the definite integral

$$A_z = \int_{-L}^{L}\frac{I_z(z')}{R}e^{-i\gamma R}dz',$$

and assume that the vibrator is excited by a constant external field E_0 determined in the gap

$$E^0(z) = \begin{Bmatrix} E_0, & z\in[L_0-b, L_0+b] \\ 0, & z\notin[L_0-b, L_0+b]\end{Bmatrix}. \qquad (2)$$

Now we will analyze the Pocklington equation (1) in three regions:

$$\left(\frac{d^2}{dz^2}+\gamma^2\right)A_z^{(1)} = 0, \quad z\in[-L, L_0-b],$$

$$\left(\frac{d^2}{dz^2}+\gamma^2\right)A_z^{(2)} = -i\omega\varepsilon_0\varepsilon E_0, \quad z\in[L_0-b, L_0+b], \qquad (3)$$

$$\left(\frac{d^2}{dz^2}+\gamma^2\right)A_z^{(3)} = 0, \quad z\in[L_0+b, L].$$

Here the superscript *k* (*k* = 1, 2, 3) refers to quantities determined in the corresponding region. Equations (3) have to be solved consistently with the corresponding boundary conditions for the tangential components of the electric and magnetic fields at the interfaces between different regions ($z = L_0 - b$; $z = L_0 + b$). For the *z*-component of the vector potential A_z, the boundary conditions are as follows:

$$\begin{aligned} A_z^{(1)} &= A_z^{(2)}, \quad \frac{\partial A_z^{(1)}}{\partial z} = \frac{\partial A_z^{(2)}}{dz}, \quad z = L_0-b, \\ A_z^{(2)} &= A_z^{(3)}, \quad \frac{\partial A_z^{(2)}}{\partial z} = \frac{\partial A_z^{(3)}}{\partial z}, \quad z = L_0+b. \end{aligned} \qquad (4)$$

For a symmetric vibrator ($L_0 = 0$), the expression for A_z can be written as ($z\in[-L, L]$)

$$\int_{-L}^{L} I_z(z')\frac{e^{-i\gamma R}}{R}dz' = C\cos(\gamma z) - \frac{2\pi i U}{\gamma b Z_c}\psi(z), \qquad (5)$$

where

$$\psi(z) = \begin{Bmatrix} 1-\cos(\gamma b)\cos(\gamma z), & z\in[-b, b] \\ \sin(\gamma b)\sin(\gamma|z|), & z\notin[-b, b]\end{Bmatrix},$$

$U = 2bE_0$ is the voltage drop across the vibrator gap, $Z_c = \sqrt{\mu_0\mu/\varepsilon_0\varepsilon}$ is the characteristic impedance of the medium, and *C* is an unknown constant determined from additional physical conditions.

The integral equation (5) will be called the generalized Hallen integral equation. In the limit $b \longrightarrow 0$, this equation transforms into the known Hallen integral equation [1–4]

$$\int_{-L}^{L} I_z(z')\frac{e^{-i\gamma R}}{R}dz' = C\cos(\gamma z) - \frac{2\pi i U}{Z_c}\sin(k|z|). \qquad (6)$$

The right-hand part of the generalized Hallen integral equation (5) possesses a continuous first derivative in contrast to that for Eq. (6) where the derivative of the right-hand part exhibits a first-order singularity at $z = 0$. This is related to the fact that the conventional Hallen integral equation descries a vibrator excited by a generator situated at $z = 0$ (zero gap width). In contrast to Eq. (6), the generalized Hallen integral equation (5) allows a finite gap width to be taken into account.

New singular integral equation. Upon differentiating Eq. (5) with respect to *z* and using the known expansion [10]

$$\frac{e^{-i\gamma R}}{R} = -\frac{i}{2}\int_{-\infty}^{\infty} e^{-ih(z-z')}J_0(\nu a)H_0^{(2)}(\nu a)dh, \qquad (7)$$

where $\nu = -i\sqrt{h^2-\gamma^2}$, $J_0(\nu a)$ is the zero-order Bessel function of the first kind, and $H_0^{(2)}(\nu a)$ is the zero-order Hankel function of the second kind, we arrive at the following integral equation:

$$\int_{-L}^{L} I_z(z')G(z, z')dz' = 2\gamma\left[C\sin(\gamma z) + \frac{2\pi i U}{\gamma b Z_c}\psi'(z)\right], \qquad (8)$$

where

$$\begin{aligned} G(z, z') &= \int_{-\infty}^{\infty} g(h)e^{-ih(z-z')}dh \\ &= \int_{-\infty}^{\infty} he^{-ih(z-z')}J_0(\nu a)H_0^{(2)}(\nu a)dh, \end{aligned} \qquad (9)$$

$$\psi'(z) = \left\{ \begin{array}{ll} \cos(\gamma b)\sin(\gamma z), & z \in [-b, b] \\ \mathrm{sgn}(z)\sin(\gamma b)\cos(\gamma z), & z \notin [-b, b] \end{array} \right\}.$$

Considering the asymptotic behavior of the integrand in (9) for $|h| \longrightarrow \infty$, one may readily show that

$$G_\infty(z, z') = \int_{-\infty}^{\infty} \{\lim_{|h|\to\infty} g(h)\} e^{-ih(z-z')} dh = \frac{2i}{z'-z}. \quad (10)$$

Thus, the kernel $G(z, z')$ in the integral equation (6) implicitly contains a singularity (10) of the Cauchy type and, hence, is a singular kernel.

Separating the singularity (10) in Eq. (8) and passing to the new variables $z = Lt$ and $z' = Lt'$, we may write the latter equation in the following form ($t \in [-1, 1]$):

$$\frac{1}{\pi}\int_{-1}^{1} \frac{I_z(t')}{t'-t} dt' = \frac{\lambda}{2}\int_{-1}^{1} I_z(t') g(t, t') dt' + \gamma a\left[C\sin(\gamma L t) + \frac{2\pi i U}{\gamma b Z_c}\psi'(t)\right], \quad (11)$$

where

$$g(t, t') = \int_{-\infty}^{\infty} \Delta G(\beta) e^{-i\beta\lambda(t-t')} d\beta,$$

$$\Delta G(\beta) = \beta J_0(\beta) H_0^{(2)}(\beta) - \frac{i}{\pi}\mathrm{sgn}(\beta), \quad \lambda = \frac{L}{a}.$$

Taking into account that the unknown constant C can be determined from (5) at $z = 0$ as

$$C = \lambda\int_{-1}^{1} I(t') G_0(t') dt' + \frac{2\pi i U}{\gamma b Z_c}\psi_0, \quad (12)$$

where

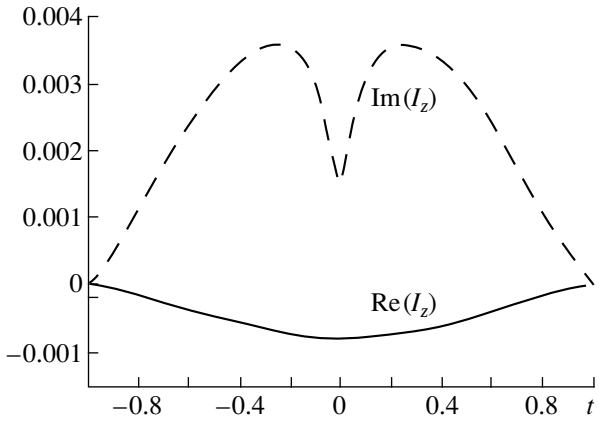

Fig. 2. The results of a numerical calculation of the real $\mathrm{Re}\{I_z(t)\}$ and imaginary $\mathrm{Im}\{I_z(t)\}$ current components for a vibrator with $b/L = 1/100$, $a/\lambda = 1/40$, and $L/\lambda = 1/4$.

$$G_0(t) = \frac{e^{-i\gamma a\sqrt{\lambda^2 t^2 + 1}}}{\sqrt{\lambda^2 t^2 + 1}}, \quad \psi_0 = 1 - \cos(\gamma b),$$

we readily obtain the following singular integral equation instead of Eq. (8) ($t \in [-1, 1]$):

$$\frac{1}{\pi}\int_{-1}^{1} \frac{I_z(t')}{t'-t} dt' + \int_{-1}^{1} I_z(t') M(t, t') dt' = \Phi(t), \quad (13)$$

where

$$M(t, t') = -\frac{\lambda}{2} g(t, t') + \gamma L G_0(t')\sin(\gamma L t),$$

$$\Phi(t) = [\psi_0\sin(\gamma L t) + \psi'(t)] 2\pi i \frac{a}{b}\frac{U}{Z_c}.$$

Relationship (13) is a singular integral equation of the first kind describing the current distribution $I_z(t)$ in a thin electric vibrator, which has no analogs in the available literature. Note that the singular integral equation (12) was written in terms of the surface current density (in contrast to the singular integral equation [8, Eq. (15)] involving a derivative of the surface current density with respect to the longitudinal coordinate. From the standpoint of practice, where it is usually necessary to know the distribution of the current (rather than of its derivative) in a vibrator, Eq. (12) should be preferred to the equation derived in [8]. For example, the new equation provides for a simpler method of determining the input impedance $Z = U/I_z(0)$,where $I_z(0)$ is the current at $z = 0$ and U is the voltage drop across the gap.

Solving the singular integral equation. Numerical results. In order to solve the singular integral equation (13), we will use the formula of inversion for the Cauchy integral. Taking into account the behavior of the function $I_z(t)$ at $t = \pm 1$, whereby $I_z(1) - I_z(-1) = 0$, this formula can be written as

$$I_z(t) = \frac{\sqrt{1-t^2}}{\pi}\int_{-1}^{1} \frac{F(\tau)}{\sqrt{1-\tau^2}(\tau - t)} d\tau, \quad (14)$$

where

$$F(\tau) = \int_{-1}^{1} I_z(t) M(\tau, t) dt - \Phi(\tau).$$

Equation (14) is essentially an inhomogeneous Fredholm integral equation of the second kind with respect to the unknown function $I_z(t)$.

Note that the singular integral equation (12) has a continuous right-hand part, in contrast to the singular integral equation [8, Eq. (15)] involving the first-order singularity at $z = \pm b$. Regularization of the latter singular integral equation using the formulas of inversion of the Cauchy integral would require separating these singularities. Without taking special measures (see,

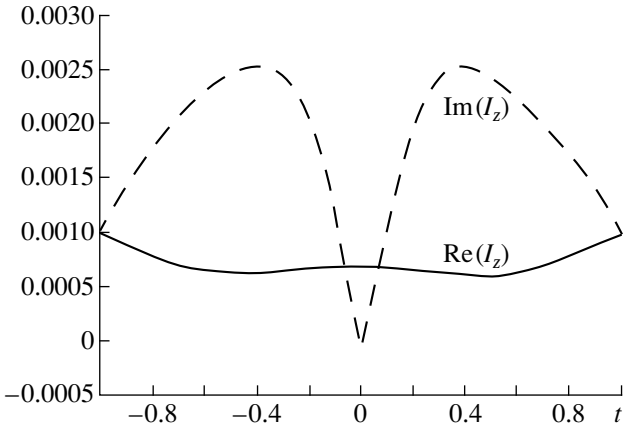

Fig. 3. The results of a numerical calculation of the real $\mathrm{Re}\{I_z(t)\}$ and imaginary $\mathrm{Im}\{I_z(t)\}$ current components for a vibrator with $b/L = 1/100$, $a/\lambda = 1/40$, and $L/\lambda = 1/2$.

e.g., [12]), the Cauchy integral for the inhomogeneous Fredholm integral equation of the second kind such as [8, Eq. (17)] will diverge. The inhomogeneous Fredholm integral equation of the second kind (14) derived above is free of this significant disadvantage.

We have numerically studied Eq. (14) by the method of mechanical quadratures [13]. Figures 2 and 3 show characteristic distributions of the real $\mathrm{Re}\{I_z(t)\}$ and imaginary $\mathrm{Im}\{I_z(t)\}$ current components for a vibrator with $b/L = 1/100$, $a/\lambda = 1/40$, and $L/\lambda = 1/4$ (Fig. 2) and 1/2 (Fig. 3). The solid curves show the behavior of $\mathrm{Re}\{I_z(t)\}$, and the dashed curves represent $\mathrm{Im}\{I_z(t)\}$. The numerical results well agree with the data reported in [6, 7].

Conclusion. It is necessary to emphasize two new results important from both a practical and theoretical standpoint.

First, we have obtained a generalized Hallen integral equation (5) possessing a number of advantages over the conventional Hallen integral equation (6) used in the antenna theory. The right-hand part of Eq. (5) has a continuous first derivative, while the derivative of the right-hand part of Eq. (6) exhibits a first-order singularity markedly complicating the solution. As a result, Eq. (5) allows a finite vibrator gap thickness b to be taken into account, in contrast to Eq. (6) referring to the case of zero-gap vibrator ($b \equiv 0$).

Second, the proposed approach based on the mathematical apparatus of the theory of singular integral equations allowed a new Fredholm integral equation of the second kind (14) with a continuous right-hand part to be derived for the description of the surface current density in a vibrator. The obtained Fredholm integral equation of the second kind provides for a mathematically correct calculation of characteristics of a thin electric vibrator. In particular, using this equation does not lead to the phenomenon of relative convergence encountered in solving the Fredholm integral equations of the first kind [4, 5], including the conventional Hallen equation.

The new singular integral equation derived in this work may, in principle, serve as a base for obtaining approximate analytical formulas for evaluating the electric current in a vibrator. The proposed method completely solves the problem of calculating the input conductivities and impedances of antennas of the vibrator type.

REFERENCES

1. *Computational Techniques for Electrodynamics*, Ed. by R. Mitrs (Pergamon, Oxford, 1973; Mir, Moscow, 1977).
2. D. M. Sazonov, *Microwave Antennas and Devices: Textbook for Radio Engineering Faculties of High Schools* (Vysshaya Shkola, Moscow, 1988).
3. G. A. Erokhin, O. V. Chernyshev, N. D. Kozyrev, and V. G. Kochershevskiĭ, *Transmission-Line and Antenna Devices and Radio Wave Propagation: Textbook for High Schools*, Ed. by G. A. Erokhin (Radio i Svyaz', Moscow, 1996).
4. V. A. Neganov, S. B. Raevskiĭ, and G. P. Yarovoĭ, *Linear Macroscopic Electrodynamics*, Ed. by V. A. Neganov (Radio i Svyaz', Moscow, 2000), Vol. 1.
5. A. N. Tikhonov and V. Ya. Arsenin, *Methods for Solving Ill-Posed Problems* (Nauka, Moscow, 1986; Halsted Press, New York, 1977).
6. S. I. Éminov, Radiotekh. Élektron. (Moscow) **38**, 2160 (1993).
7. V. A. Neganov and I. V. Matveev, Izv. Vyssh. Uchebn. Zaved., Radiofiz. **43** (3), 412 (2000).
8. V. A. Neganov, I. V. Matveev, and S. V. Medvedev, Pis'ma Zh. Tekh. Fiz. **26** (12), 86 (2000) [Tech. Phys. Lett. **26**, 535 (2000)].
9. V. A. Neganov, E. I. Nefedov, and G. P. Yarovoĭ, *Strip and Slot Structures for SHF and EHF Ranges* (Nauka, Moscow, 1996).
10. V. A. Neganov, E. I. Nefedov, and G. P. Yarovoĭ, *Modern Methods of Designing SHF and EHF Transmission Lines and Resonators* (Pedagogika-Press, Moscow, 1998).
11. G. T. Markov and A. F. Chaplin, *Excitation of Electromagnetic Waves* (Énergiya, Moscow, 1967).
12. F. D. Gakhov, *Boundary Value Problems* (Nauka, Moscow, 1977; Addison-Wesley, Reading, 1966).
13. V. V. Panasyuk, M. P. Savruk, and Z. T. Nazaruk, *Methods of Singular Integral Equations in Two-Dimensional Diffraction Problems* (Naukova Dumka, Kiev, 1984).

Translated by P. Pozdeev

Technical Physics Letters, Vol. 27, No. 2, 2001, pp. 164–167. Translated from Pis'ma v Zhurnal Tekhnicheskoĭ Fiziki, Vol. 27, No. 4, 2001, pp. 72–81.

A Decrease in the Noise Stokes Field Modulation during the Induced Mandel'shtam–Brillouin Scattering in a Single-Mode Optical Fiber with High Rayleigh Scattering Losses

A. A. Fotiadi and R. V. Kiyan

Ioffe Physicotechnical Institute, Russian Academy of Sciences, St. Petersburg, 194021 Russia

Received September 15, 2000

Abstract—Noise fluctuations of the Stokes field intensity during the induced Mandel'shtam–Brillouin scattering (IMBS) of microsecond pumping radiation pulses in a 300-m-long single-mode optical fiber with 17 dB/km losses were experimentally studied. As the pumping pulse width increases from 20 to 600 μs, the noise modulation amplitude of the IMBS intensity and the IMBS line width tend to decrease. This phenomenon is explained by a distributed feedback mechanism related to the double Rayleigh backscattering of the Stokes component of IMBS. © *2001 MAIK "Nauka/Interperiodica".*

Introduction. In many practical applications of the induced Mandel'shtam–Brillouin scattering (IMBS) effect, a highly undesirable interference is the strong temporal modulation of the accompanying Stokes radiation field. This phenomenon is usually observed for the IMBS in both nonwaveguide media [1] and in optical fibers [2].

The main reason leading to fluctuations of the Stokes field with a characteristic time in the nanosecond range is the noise nature of a seeding Stokes wave. Initiated due to the pumping radiation scattering from thermal hypersonic waves, the Stokes wave retains the stochastic properties of the spontaneous scattering upon a single passage. This is manifested in the random amplitude and phase modulation of the Stokes radiation. In the course of amplification of the Stokes field, the spontaneous scattering spectrum exhibits narrowing by a factor of $\sim\sqrt{M}$, where $M \approx 16$–20 is the IMBS gain increment.

At the fiber output, the Stokes radiation field represents a Gaussian random process with a zero mean and a wave intensity distribution of the Rayleigh type. The IMBS intensity is randomly modulated at a 100% amplitude and a characteristic correlation time $\sim\sqrt{M}\,T_2$, where $T_2 \approx 10$ ns is the hypersonic wave relaxation time (estimated for $\lambda \sim 1$ μm) [3]. A significant decrease in the IMBS modulation can be achieved only for a sufficiently high pumping intensity (>1 W), when the light travel time over the effective IMBS gain length is on the order of the hypersonic wave relaxation time [4, 5].

The noise fluctuations of the Stokes field intensity can be completely suppressed in IMBS lasers representing optical fiber systems with Stokes field feedback. However, these systems are usually characterized by a modulation instability with respect to fluctuations related to a finite resonator length. This factor also gives rise to profound modulation in the output radiation intensity [6, 7].

This paper describes the results of investigation of the noise fluctuations of the Stokes field intensity in a long optical fiber with high Rayleigh scattering losses. The experiments revealed a threefold decrease in amplitude of the noise-related IMBS intensity modulation and a 100-fold narrowing of the IMBS line. The effects are explained by a distributed feedback mechanism related to the double Rayleigh backscattering of the Stokes component of IMBS.

Experimental setup and procedure. Figure 1 shows a schematic diagram of the experimental setup.

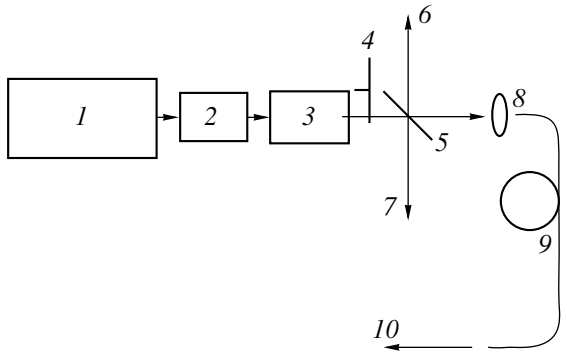

Fig. 1. A schematic diagram of the experimental setup: (*1*) Nd:YAG laser (λ = 1064 nm); (*2*) electrooptical modulator; (*3*) optical decoupler; (*4*) mechanical modulator; (*5*) glass plate; (*6*) to the Stokes signal detector; (*7*) to the pumping signal detector; (*8*) objective; (*9*) 300-m-long single-mode fiber; (*10*) to the transmitted pumping signal detector.

1063-7850/01/2702-0164$21.00 © 2001 MAIK "Nauka/Interperiodica"

The IMBS pumping was provided by a source based on a continuous Nd:YAG laser operating in a single transverse and a single longitudinal mode at a wavelength of 1.06 μm and an output power of 1–2 W. The pumping source was built around a commercial LTN-503 laser with the front mirror replaced by an optical element comprising a stack of five plane-parallel glass plates with ring spacers (both plates and rings were 4 mm thick). The stack had a maximum reflection coefficient of 80% at the working wavelength and ensured reliable selection of a single longitudinal mode. Selection of a single transverse mode was provided by a diaphragm mounted in the laser cavity between the active element and the stack.

The spectral line width of the laser used in our experiments did not exceed ~50 kHz. The pumping pulses were produced from the continuous Nd:YAG laser radiation with the aid of external electrooptical (EOM) or mechanical (chopper) modulators. The pumping laser was decoupled from spurious reflections by means of a magnetooptical pulse Faraday cell. The moment of the cell switching was adjusted so as to coincide with opening of the modulator forming the pumping radiation pulses.

The Mandel'shtam–Brillouin scattering was induced in a single-mode quartz fiber with a core diameter of ~5 μm and an aperture of 0.09. The level of light attenuation in the fiber was ~17 dB/km. The losses were related primarily to the Rayleigh scattering, the absorption contribution being rather insignificant. The fiber length was about 300 m; in order to avoid spurious reflections, the fiber ends were cut so as to make an oblique angle with the axis. The effect of external vibrations was minimized by putting the fiber into a foamed-plastic box.

The experiments were conducted by simultaneously measuring the time variation of the input and output pumping powers and the scattered Stokes wave intensity. For this purpose, the corresponding radiation beam was separated by decoupling plates and directed to photodiodes of the LFD-2 type with a characteristic rise time of ~0.5 ns. The output signals from the detector diodes were transmitted to storage oscillographs. The oscillograms were digitized and fed to a computer for processing and analysis.

Experimental results. The measurements were carried out for the pumping pulses of two types entering the optical fiber.

In the first case, the laser radiation was transmitted through the electrooptical modulator controlled by a sinusoidal voltage with a period that could be varied from 10 to 40 μs. Figure 2 shows typical oscillograms of the IMBS signal observed with the pumping intensity modulated by a sinusoidal law. For a maximum pumping power of ~200 mW, the IMBS leads to a significant exhaustion of the pumping power transmitted through the fiber. The output signal exhibits deep fluctuations related to the noise character of a seeding

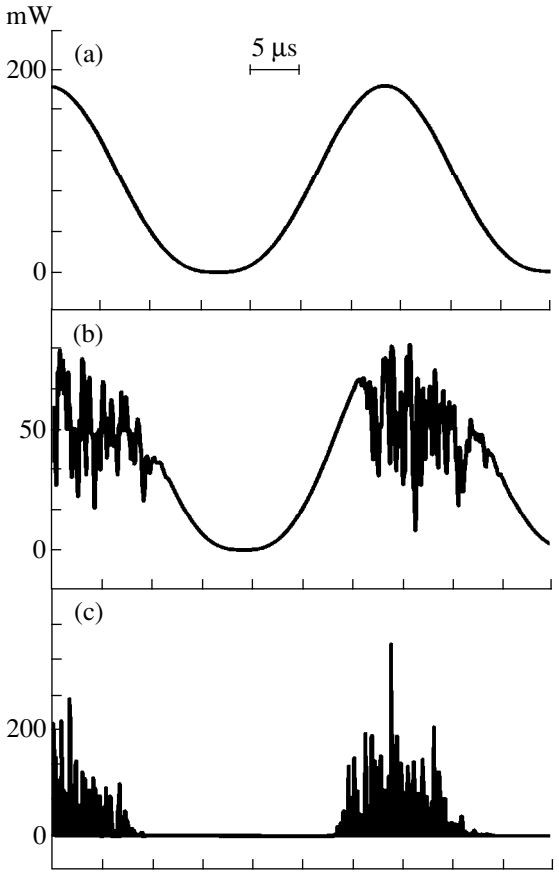

Fig. 2. Typical oscillograms of the IMBS signals: (a) input pumping radiation, (b) pumping radiation transmitted through the fiber, (c) scattered Stokes radiation. The pumping radiation is modulated by a sinusoidal signal with a period of ~33 μs.

Stokes radiation. A thorough analysis of these fluctuations confirmed their chaotic nature and showed their characteristic time scale to be 50–200 ns and the modulation amplitude to reach 100%. The normal standard deviation of the Stokes wave intensity $\Delta P_S = \sqrt{\langle P_S^2(t)\rangle / \langle P_S(t)\rangle^2 - 1}$ for all oscillograms was unity (to within 0.05). A correlation function of the Stokes field intensity $C(\tau) = \langle P_S(t+\tau)P_S(t)\rangle / \langle P_S(t)\rangle^2 - 1$ calculated using these oscillograms is well described by the Gaussian curve with a correlation time of ~50 ns.

A statistical analysis of the oscillograms of the scattered radiation showed the distribution of instantaneous realizations of the Stokes field intensity to obey the Rayleigh law. This fact proves the Stokes wave field to represent a Gaussian random process with zero mean. The energy spectrum of the Stokes field restored from the correlation function has a full width of ~10 MHz on the e^{-1} level (FWe^{-1} M). It should be noted that the correlation time τ_c and the energy spectrum width FWe^{-1} M = $\Delta\nu_S$ for the Gaussian random process are related by the formula $\Delta\nu_S = \sqrt{2}/\pi\tau_c$ [8].

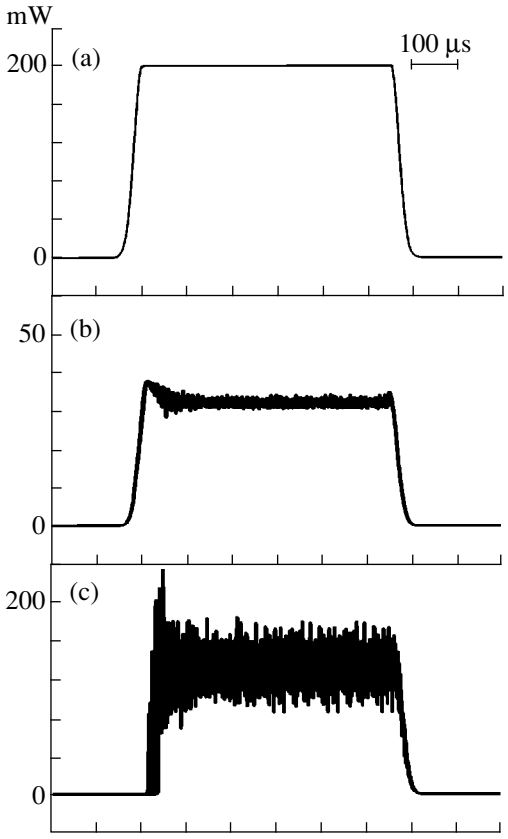

Fig. 3. Typical oscillograms of the IMBS signals: (a) input pumping radiation pulse, (b) pumping radiation pulse transmitted through the fiber, (c) scattered Stokes radiation. The pumping radiation is modulated by rectangular pulses with a ~600 μs duration.

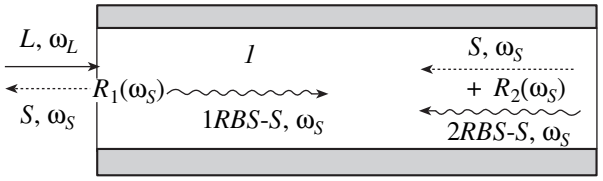

Fig. 4. A schematic diagram illustrating joint IMBS and Rayleigh backscattering (*RBS*) processes in a single-mode optical fiber; *I* indicates an IMBS gain of ~exp(20).

In the second case, the pumping was effected with 600-μs-long rectangular pulses cut from the continuous laser radiation by the mechanical modulator (chopper). Here, the leading and trailing front duration was ~20 μs and the pulse height instability within a pulse width did not exceed ~1%. Figure 3 shows typical oscillograms of the IMBS signal obtained with the pumping intensity modulated by rectangular pulses. For the same maximum pumping power of ~200 mW as above, we observe a lower exhaustion of the pumping power transmitted through the fiber and, accordingly, a smaller coefficient of the power conversion from pumping to Stokes waves. The noise fluctuations in both the Stokes and transmitted radiation components modulate the output signals to a much lower extent as compared to the case of sinusoidal modulation. As seen, the modulation amplitude does not exceed 30%, and the output signal intensity never drops to zero. The characteristic time scale of the fluctuations remained on the same level (100–200 ns).

More detailed characteristics were provided by the computer-aided analysis of the oscillograms. The normal standard deviation of the Stokes wave intensity $\Delta P_S = \sqrt{\langle P_S^2(t)\rangle / \langle P_S(t)\rangle^2 - 1}$ for all oscillograms is ~0.13 (to within 0.02). The correlation function of the Stokes field intensity is still well described by the Gaussian curve with a correlation time of ~50 ns. A statistical distribution of the instantaneous realizations of the Stokes field intensity is approximated by a Gaussian curve centered at $P_S = \langle P_S \rangle \approx 100$ W, which implies that the Stokes wave field no longer represents a Gaussian random process with zero mean.

The energy spectrum of the Stokes radiation was directly measured using a self-heterodyne fiber interferometer with a 2-km-long delay line. An acoustooptical modulator in the short shoulder of the interferometer provided for a ~70 MHz frequency shift for the nondelayed radiation component. The results of these measurements showed that the IMBS spectrum width did not exceed 100 kHz, this estimate being determined by the interferometer resolution.

Discussion of results. The main reason for a qualitative difference between oscillograms obtained in the different pumping modes cannot be related to the nonstationary character of the IMBS process. Indeed, the period of the pumping intensity modulation in both cases is markedly greater than the hypersonic wave relaxation time ($T_2 \approx 10$ ns [3]), and, hence, the IMBS process in both cases is stationary. The observed effect can be explained in terms of a distributed feedback mechanism operative in the fiber due to the double Rayleigh backscattering of the Stokes component of IMBS.

Let us consider qualitatively the IMBS process with a continuous pumping in a single-mode optical fiber with an allowance for the Rayleigh scattering losses. The pattern of waves participating in the process is schematically depicted in Fig. 4. Monochromatic radiation with a pumping frequency ω_L entering the optical fiber induces effective generation of the Stokes waves from the noise, which takes place within a spectral band of $\Delta\omega_S \sim 2/T_2$ around the central Stokes central frequency $\omega_{S0} = \omega_L - \Omega_0$. Spreading in the fiber, each Stokes wave with a frequency ω_S is subject to the Rayleigh backscattering with the formation of a Stokes counterwave with the same frequency ω_S (1-*RBS*-*S*). The latter wave travels together with the pumping wave and is not involved in the IMBS process. However, the 1-*RBS*-*S* wave is also scattered by the Rayleigh mechanism with the formation of a doubly scattered Stokes

wave (2-*RBS*-*S*) that adds coherently to the initial Stokes wave. This addition takes place with different phases (i.e., either in phase or in counterphase) for various points and spectral components, giving rise to both positive and negative local feedback. The effective feedback averaged over the fiber length is also different for various spectral components ω_S of the Stokes field.

The pattern outlined above is essentially equivalent to an interferometer realized in the fiber between two Rayleigh mirrors denoted by $R_1(\omega_S)$ and $R_2(\omega_S)$ in Fig. 4. Although the reflection coefficients of these Rayleigh mirrors are very small (in single-mode fibers, the Rayleigh backscattering intensity amounts to ~1/600 of the losses due to the Rayleigh scattering [9]), the giant IMBS gain in the optical fiber (reaching $\sim e^{20}$ times) is sufficient to produce the preferred amplification of separate narrow spectral components of the Stokes field and may even lead to lasing at the selected frequencies obeying the condition $R_1(\omega_S)R_2(\omega_S)\exp\{20\} \sim 1$. This circumstance explains a strong narrowing of the IMBS lines observed in the experiment.

Based on this model, we may qualitatively explain the experimental results presented above. In the case of a sinusoidal pumping, the modulation frequency (corresponding to a period of 10–40 μs) was sufficiently high to prevent the formation of an effective feedback related to the double Rayleigh scattering. In other words, a feedback process with respect to the Stokes signal could not develop during the pumping pulse and was suppressed. Therefore, the system featured the usual dynamics of the IMBS signal development from noise, with the process parameters being in good agreement with the values reported previously for the IMBS experiments in fibers [2].

In the second case, stable rectangular pumping pulses with a duration of ~600 μs allowed an effective stationary Rayleigh feedback to establish. This feedback led to a narrowing of the generation line and a decrease in the Stokes field modulation amplitude.

Conclusion. The IMBS in a single-mode optical fiber with large Rayleigh scattering losses was accompanied by a decrease in the amplitude of noise modulation of the Stokes radiation field, a narrowing of the IMBS spectrum, and a change in the statistical characteristics. These effects are explained by the formation of a distributed feedback mechanism related to the double Rayleigh backscattering of the Stokes component of IMBS.

This phenomenon can be used for creating new tunable lasers and active distributed fiber sensors. Statistical characteristics of the joint scattering by the Rayleigh and Mandel'shtam–Brillouin mechanisms will be considered in more detail in subsequent publications.

Acknowledgments. This study was supported by the Russian Foundation for Basic Research, project no. 00-02-16903.

REFERENCES

1. V. I. Bespalov, A. A. Betin, G. A. Pasmanik, and A. A. Shilov, Pis'ma Zh. Éksp. Teor. Fiz. **31** (11), 668 (1980) [JETP Lett. **31**, 630 (1980)].
2. G. L. Gaeta and R. W. Boyd, Phys. Rev. A **44** (5), 3205 (1991).
3. E. M. Dianov, A. Ya. Karasik, A. V. Luchnikov, and A. K. Senatorov, Kvantovaya Élektron. (Moscow) **16** (4), 778 (1989).
4. E. M. Dianov, A. Ya. Karasik, A. V. Lutchnikov, and A. N. Pilipetskii, Opt. Quantum Electron. **21** (5), 381 (1989).
5. A. A. Fotiadi and E. A. Kuzin, Zh. Tekh. Fiz. **65** (7), 195 (1995) [Tech. Phys. **40**, 740 (1995)].
6. I. Bar-Joserph, A. A. Friesem, E. Lichman, and R. G. Waarts, J. Opt. Soc. Am. B **2** (10), 1606 (1985).
7. R. G. Harrison, P. M. Ripley, and W. Lu, Phys. Rev. A **49** (1), R24 (1994).
8. S. A. Akhmanov, Yu. E. D'yakov, and A. S. Chirkin, *Introduction to Statistical Radio Physics and Optics* (Nauka, Moscow, 1981).
9. A. Y. Hartog and M. P. Gold, J. Lightwave Technol. **LT-2** (2), 76 (1984).

Translated by P. Pozdeev

Technical Physics Letters, Vol. 27, No. 2, 2001, pp. 168–170. Translated from Pis'ma v Zhurnal Tekhnicheskoĭ Fiziki, Vol. 27, No. 4, 2001, pp. 82–88.

Manganese Depth–Concentration Profiles in Ion-Implanted Silicon Studied by Rutherford Backscattering

B. É. Égamberdiev and M. Yu. Adylov

Abu Raikhan Beruni State Technical University, Tashkent, Uzbekistan

Received September 4, 2000

Abstract—Variation of the depth–concentration profiles of manganese atoms implanted into silicon was studied by the Rutherford backscattering (RBS) method in samples irradiated to various doses and annealed at different temperatures. The results are consistent with the analogous data obtained by an independent method. The post-implantation thermal annealing affects the distribution of Mn and other impurities, in particular, oxygen. The RBS method provides data both on the distribution of implanted dopants and on their interaction with other impurities. © *2001 MAIK "Nauka/Interperiodica".*

The obtaining of thin ion-implanted layers at the silicon surface, possessing a preset thickness and desired physical properties, is important for development of the technology of various transducers and high-performance sensors. Among the most interesting dopants are elements of the transition groups, in particular, manganese. Unfortunately, thin silicon layers doped with the transition elements, characterized by a sharply restricted depth and sufficiently large dopant concentration, cannot be obtained by methods based on diffusive penetration because the diffusion coefficients of these elements in silicon are rather large. For this reason, silicon is usually doped with the transition elements using ion beam implantation technology.

Since the Mn impurity atoms may occupy both the lattice sites and interstitial positions in the silicon crystal lattice and are capable of interacting with the lattice defects, it is of interest to know the distribution of implanted Mn atoms and the mechanism of their activation. However, no data on the ion implantation of manganese into silicon and on the implant depth distribution were found in the literature. The purpose of this study was to determine the depth–concentration profiles of manganese atoms ion-implanted into silicon and study their variation depending on the ion irradiation dose and the post-implantation annealing temperature.

As is known, the dopant depth–concentration profiles in the ion-implanted layers are most frequently studied by methods of the secondary-ion mass spectrometry (SIMS) and Auger electron spectroscopy (AES) in combination with the gradual layer removal by ion sputtering. Unfortunately, these conventional techniques do not provide sufficiently precise quantitative data on the dopant concentration necessary to obtain thin manganese-doped layers with preset parameters. For this reason, we have studied the manganese dopant depth–concentration profiles and the effect of temperature on their shapes by the method of Rutherford backscattering (RBS).

The experiments were performed with samples made of single-crystal silicon wafers of the KDB grade with $\rho = 10\ \Omega$ cm. The samples were implanted with 40-keV Mn ions on an ILU-3 setup, using an ion beam incident along the (111) axis direction. The ion irradiation (implantation) dose $N_{\square}$ was varied from 10^{15} to 10^{17} cm^{-2}. The resistivity of samples was determined by the conventional four-point-probe technique.

Figure 1 shows the depth–concentration profiles of silicon implanted with Mn to various doses. Irrespec-

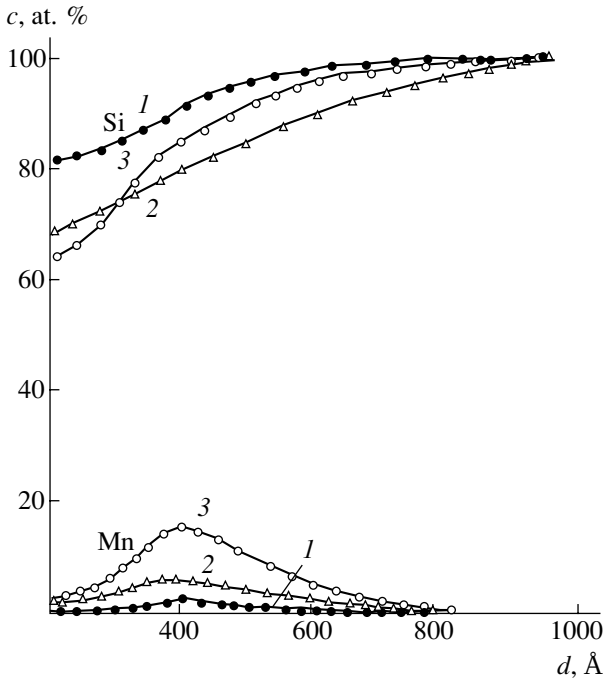

Fig. 1. Manganese and silicon depth–concentration profiles in silicon single crystals ion-implanted with Mn to a dose of (*1*) 10^{15}, (*2*) 10^{16}, and (*3*) 10^{17} cm^{-2}.

tive of the implantation dose, the curves are described by the Gaussian function. The projected ion range *Rp* varies from 398 to 410 Å, depending on the dose. These results are consistent with the data obtained by other methods, for example, by SIMS profiling [1].

The RBS analysis of the silicon samples irradiated with manganese ions to a dose of 10^{15} cm^{-2} gave the following results. The uppermost surface layer composition (at. %): Si, 82.7; O, 17; Mn, 0.5; the composition of a 200-Å-deep layer (at. %): Si, 88; O, 10; Mn, 2; to within the RBS sensitivity, manganese is detected to a depth of ~600 Å and oxygen, to ~900 Å. For the silicon samples implanted with Mn ions to a dose of 10^{16} cm^{-2}, the results were as follows. The uppermost surface layer composition (at. %): Si, 69; O, 29; Mn, 2; a considerable variation was observed for a 200-Å-deep layer composition (at. %): Si, 76; O, 18; Mn, 6. To within the RBS sensitivity, manganese is detected to a depth of ~650 Å, while the oxygen content sharply decreases beginning with this depth and is not at all detected at ~900 Å. Finally, for the samples implanted with Mn ions to a dose of 10^{17} cm^{-2}, the uppermost surface layer composition was as follows (at. %): Si, 64; O, 34; Mn, 2; and for a 200-Å-deep layer, the composition was (at. %): Si, 82; O, 3; Mn, 15.

Analysis of the obtained profiles showed that the ion implantation of manganese is accompanied by oxygen redistribution both in the uppermost surface layer and at a depth of the maximum manganese concentration. We may suggest that implanted manganese ions mostly displace oxygen atoms, which is valid provided that this oxygen occurs in the free state in a silicon crystal.

Data on the behavior of dopants in the course of thermal annealing are of considerable interest from both theoretical and practical standpoints. Below we present the results of investigation of the effect of a 30-min annealing at various temperatures on the manganese profiles in ion-implanted silicon. As seen from Fig. 2, the annealing at 600°C has no significant influence on the dopant distribution. Pronounced effects are observed in the samples annealed at a temperature of 900°C. In a sample doped with a dose of 10^{15} cm^{-2} and annealed at this temperature, the maximum Mn concentration is ~2 at. % and this peak shifts to a depth of ~800 Å (Fig. 3); manganese is not detected on the surface. The surface concentration of oxygen decreases to 27 at. %; oxygen is not detected at a depth of 800 Å.

In a sample doped with a dose of 10^{16} cm^{-2}, the annealing for 30 min at 600°C also barely influenced the dopant distribution: only some smearing of the Mn profile is observed. In the sample annealed at 900°C, the maximum of the Mn distribution shifted to 800 Å and decreased to 5 at. %. More pronounced changes were observed upon annealing a sample doped with a dose of 10^{17} cm^{-2}. The 30-min treatment at 600°C shifted the Mn distribution peak to a depth of 380 Å and slightly increased the content of manganese on the surface. The Mn profile was strongly changed by the

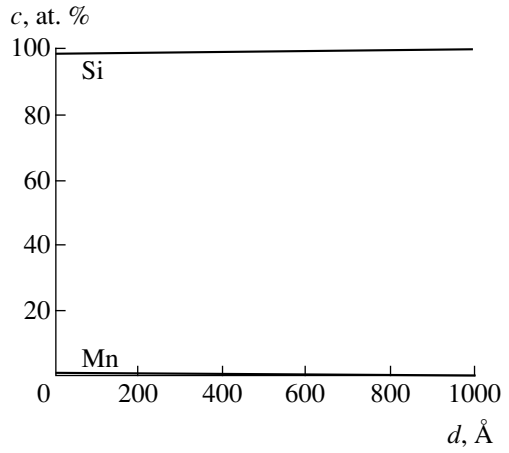

Fig. 2. Manganese and silicon depth–concentration profiles in silicon single crystals ion-implanted with Mn to a dose of 10^{15} cm^{-2} and then annealed for 30 min at 600°C.

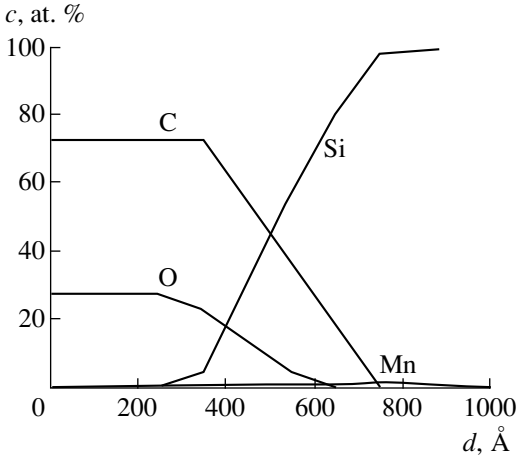

Fig. 3. The depth–concentration profiles of silicon, dopant (Mn) and impurities (O and C) in silicon single crystals ion-implanted with Mn to a dose of 10^{15} cm^{-2} and then annealed for 30 min at 900°C.

30-min annealing at 900°C, whereby the dopant concentration peak shifted to a depth of 600 Å, the distribution became more smooth, and Mn was observed at an amount of 5 at. % down to a depth of ~1200 Å.

An analysis of the experimental results indicates that the RBS method not only provides data on the distribution of elements in relative units, but allows the absolute quantitative characteristics to be obtained as well.

In our opinion, there is a interesting relationship between the distributions of manganese and oxygen in the manganese-doped silicon crystals. A comparison of the oxygen and manganese profiles shows a maximum in the content of Mn corresponding to a minimum in the concentration of oxygen and vice versa. The undoped (unimplanted) initial silicon samples are characterized by the oxygen distribution with some excess on the surface, followed by a monotonic decrease with depth and

certain constant concentration in the bulk. This distribution is changed upon manganese ion implantation. The content of oxygen increases on the surface and in the subsurface layer and sharply drops in the region of maximum Mn concentration. This pattern is generally the same in silicon samples implanted with various doses of manganese.

Based on the obtained results, we may ascertain that implanted manganese ions mostly displace oxygen atoms. This statement is valid provided that oxygen occurs in the free (unbound) state in a silicon crystal. The ion implantation process not only affects the oxygen profile, but changes the distribution of defects as well. The defects appearing both on the surface and in depth of silicon expose free radical species capable of attracting free particles (in particular, oxygen).

Conclusion. We investigated the depth–concentration profiles of Mn in silicon crystals ion-implanted with various doses of manganese ions. The results obtained by RBS agree well with analogous SIMS profiling data. We have also studied the effect of post-implantation thermal annealing on the manganese and oxygen profiles. The RBS data can be used both for the analysis of dopant distribution and for the study of interaction between various impurities. In order to confirm these conclusions, it is necessary to study the structure and defects of the crystal lattice of implanted silicon.

REFERENCES

1. M. K. Bakhadyrkhanov, B. É. Égamberdiev, M. S. Abdugabbarov, and K. Khaĭdarov, Neorg. Mater. **31** (3), 301 (1995).

Translated by P. Pozdeev

Technical Physics Letters, Vol. 27, No. 2, 2001, pp. 87–89. Translated from Pis'ma v Zhurnal Tekhnicheskoĭ Fiziki, Vol. 27, No. 3, 2001, pp. 1–6.

Electron Structure of Thin Fullerene Films Deposited by Various Methods

A. L. Shakhmin*, A. M. Khodorkovskiĭ*, S. V. Murashov*, T. O. Artamonova, and A. V. Golod****

** State Scientific Center of Applied Chemistry, St. Petersburg, Russia*

*** Ioffe Physicotechnical Institute, Russian Academy of Sciences, St. Petersburg, 194021 Russia*

Received September 14, 2000

Abstract—The valence-band photoelectron spectra and the photoelectron energy loss spectra behind the C1*s* peak in the X-ray photoelectron spectra were studied in thin fullerene films deposited by various methods. The fine structure in the density of states near the valence band bottom observed for the fullerene films deposited by the method of pulsed supersonic molecular beam (SMB) with a helium carrier may be indicative of the presence of a long-range order. The spectra of π-plasmon losses in the films obtained by methods of thermal and SMB deposition exhibit a significant difference that can be related to a closer packing of C_{60} molecules in the latter case. © *2001 MAIK "Nauka/Interperiodica".*

Previously [1], we proposed a new method for depositing fullerene films based on a supersonic molecular beam (SMB) of an inert gas enriched with C_{60} molecules. In SMBs using helium as a carrier gas, the kinetic energy of fullerene molecules was on the order of one electronvolt. This is more than ten times greater as compared to the kinetic energy of C_{60} molecules in the gas phase upon the evaporation of fullerite. We have also observed [1] a considerable difference in the stability under laser irradiation and in the desorption temperature for the films obtained by methods of (i) conventional thermal deposition (TD) of a fullerene vapor in vacuum and (ii) interaction of a fullerene-rich SMB with a substrate surface. This difference is probably related to the fact that accelerated fullerene molecules employed in the latter case form stronger bonds both with the substrate surface and with each other, this factor affecting the structure and properties of the films as well as the individual characteristics of C_{60} molecules.

In order to determine how the kinetic energy of deposited molecules may affect the characteristics of thin fullerene films, we have performed a comparative study of the electron structures of such films obtained by TD and SMB methods. The electron properties of the films were studied by X-ray photoelectron spectroscopy (XPS). Using this method, it is possible to estimate a change in the binding energy between molecules in a thin film [2] and in the degree of crystallinity [3] by the spectra of plasma losses and valence-band energy levels.

The C_{60} fullerene films were deposited by TD and SMB methods onto nickel substrates as described [1]. The time of exposure to air after deposition (prior to charging into the electron spectrometer) did not exceed 3 min. All fullerene films had a thickness of about 200 nm, which allowed the substrate to be ignored because the probed depth in XPS does not exceed 10 nm. The amount of oxygen on the film surface did not exceed 4 at. %.

The photoelectron spectra of the valence-band levels and the photoelectron energy loss spectra were measured on an ESCA-5400 spectrometer using Al*K*α radiation, which was monochromatized in order to increase the energy resolution. Figure 1a shows the valence-band photoelectron spectra of the SMB and TD films. The main features of the density of states (DOS) in the valence band, which are determined by the atomic properties and the short-range atomic order, are consistent with the published data [2, 4]. At the same time, it is necessary to note a small decrease (~1 eV) in width of the valence band in SMB fullerene films as compared to that in the TD films. This decrease in the energy band width is also manifested in the *KVV* Auger peak of carbon, which contains a contribution due to the valence-band electrons. The lower valence band width allows us to expect the SMB films to be more ordered in comparison with the TD fullerene film, since any additional disorder naturally leads to the appearance of extra levels and, hence, to the band broadening [5].

Affecting the valence band width, the structural ordering must be also manifested in the structure of the valence band bottom. As demonstrated in [3], the DOS structure at the valence band bottom in some substances (graphite, silicon, germanium, etc.) is related to the long-range order. A relationship between the fine structure of the valence-band DOS spectrum of carbon, formed by the *s*-electrons, and the degree of crystallinity was also considered [6] for diamond, crystalline graphite, and glassy carbon. The effect of disorder in the fullerene structures on the fine structure of the

1063-7850/01/2702-0087$21.00 © 2001 MAIK "Nauka/Interperiodica"

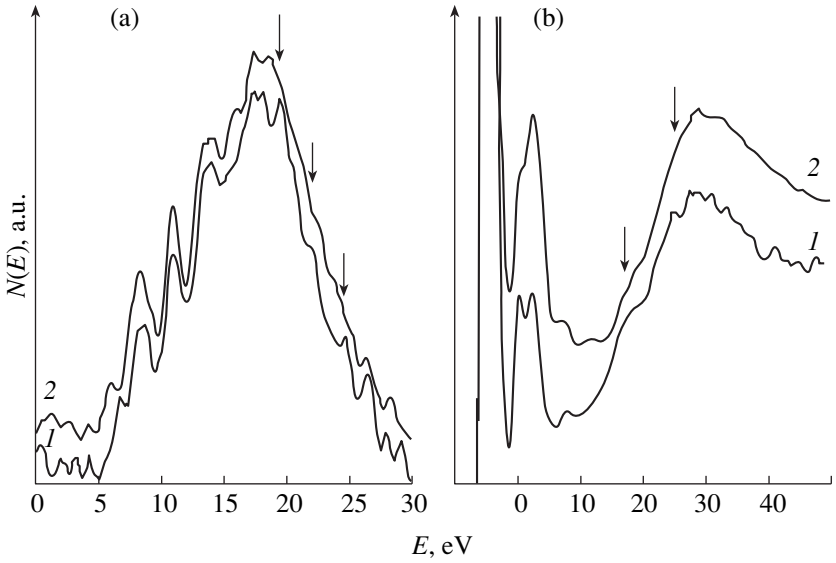

Fig. 1. X-ray photoelectron spectra of (a) the valence-band levels and (b) photoelectron energy losses behind the C1*s* peak for C_{60} fullerene films obtained by (*1*) SMB and (*2*) TD methods. Arrows indicate the characteristic features related to a fine DOS structure at the valence band bottom. The energy loss spectra are normalized to the C1*s* peak amplitude.

valence-band levels was theoretically studied in [7]. The results of these theoretical calculations indicate that the structure of the valence band bottom becomes more pronounced with an increasing degree of ordering.

A comparison of the valence-band level structures of the TD and SMB fullerene films (Fig. 1a) shows that a pronounced fine structure appears in the latter case near the bottom of valence band formed by the *s*-electrons. This fact confirms the above assumption concerning the presence of structures with a long-range order in the SMB films. Additional evidence for the ordering of these films is the presence of certain features in the spectra of photoelectron energy losses behind the C1*s* peak, which are related to the excitation of electrons from the valence band bottom to the conduction band (Fig. 1b).

Thus, taking into account the above considerations, concerning the effect of structural ordering on the DOS structure at the valence band bottom, and the experimental data, we may ascertain that SMB fullerene films possess a more ordered structure as compared to that of the TD films.

As noted above, an increase in the kinetic energy of adsorbed fullerene particles must result in the formation of stronger bonds between C_{60} molecules in the deposited thin films. This, in turn, must be reflected in the XPS spectra, predominantly those of the π-electrons, the orbitals of which are most sensitive to changes in the character of bonding. Unfortunately, a difference between the valence-band spectra of TD and SMB films in the region of the valence band top is poorly pronounced because of a small photoionization cross section of the π-states of carbon for the Al*K*α excitation (1486.3 eV). However, the features related to the short-range order are well manifested in characteristics of the π-plasmons representing the collective oscillations of π-electrons in fullerenes.

The photoelectron energy loss spectra presented in Fig. 1b show that the amplitude of losses (~6.0 eV) related to the excitation of π-plasmons in the TD fullerene film is consistent with the data reported in [2, 8], while the loss amplitude observed in the SMB film is smaller in comparison with both the main carbon peak and the peak of losses due to the interband electron transitions between valence and conduction bands. The π–σ plasmon (~25 eV) loss amplitudes are virtually the same for the films of different types. Similar variations of the π-plasmon amplitudes were observed [2] during the photopolymerization of C_{60} films under the action of a UV radiation. A decrease in the intensity of plasma losses was attributed [2] to the formation of a photopolymer molecules [9], which decreases the number of free π-electrons in C_{60} molecules.

The results of our experiments suggest that a change in the amplitude of plasma losses observed in the SMB fullerene films reflects a change in the state (and symmetry) of π-electrons in the C_{60} molecules. Possible factors responsible for these changes can be the partial polymerization taking place in the course of the film formation and the X-ray-induced photopolymerization during the XPS measurements. However, the results of measurements of the freshly deposited SMB films by the method of Raman scattering spectroscopy did not confirm the presence of a polymerized C_{60} phase [10]. We also did not observe any change in shape of the π-plasmon loss peak with an increasing dose of the X-ray irradiation, which is evidence for the absence of

the X-ray stimulated polymerization (in agreement with the results reported in [2, 11]).

In connection with this, the most probable reason explaining a decrease in the relative amplitude of the π-plasmon peak for the SMB films in comparison with the TD films is the greater binding energy between fullerene molecules, which leads to an increase in the density of the former films. For this reason, a perturbation (caused by the interaction of electron shells of the neighboring C_{60} molecules) introduced into development of the collective oscillations of π-electrons leads to a decrease in probability of the π-plasmon excitation, which is manifested in the photoelectron energy loss spectra.

Thus, the results of a comparative XPS investigation of the fullerene films obtained by thermal deposition (TD) and supersonic molecular beam (SMB) methods lead to the conclusion that the SMB fullerene films contain (in contrast to the TD films) molecular structures possessing a long-range order. The higher density of molecular packing in the SMB fullerene films decreases the probability of the π-plasmon excitation.

Acknowledgments. The work was supported by the "Fullerenes and Atomic Clusters Program" of the Intellectual Cooperation Foundation supported by the Ministry of Science and Technological Policy of the Russian Federation (project no. 98-085).

REFERENCES

1. M. A. Khodorkovskiĭ, A. L. Shakhmin, S. V. Murashov, *et al.*, Pis'ma Zh. Tekh. Fiz. **24** (10), 20 (1998) [Tech. Phys. Lett. **24**, 379 (1998)].
2. Jun Onoe, Aiko Nakao, and Kazuo Takeuchi, Phys. Rev. B **55** (15), 10051 (1997).
3. V. V. Nemoshkalenko and V. G. Aleshin, *Electron Spectroscopy of Crystals* (Naukova Dumka, Kiev, 1976).
4. J. H. Weaver, Jose Luis Martins, T. Komeda, *et al.*, Phys. Rev. Lett. **66** (13), 1741 (1991).
5. A. R. Silin' and A. N. Trukhin, *Point Defects and Elementary Excitations in Crystalline and Glassy SiO_2* (Zinatne, Riga, 1985).
6. F. R. McFeely, S. P. Kowalczyk, L. Ley, *et al.*, Phys. Rev. B **9** (12), 5268 (1974).
7. Martin P. Gelfand and Jian Ping Lu, Phys. Rev. Lett. **68** (7), 1050 (1992).
8. Ryuichi Kuzuo, Masami Terauchi, Michiyoshi Tanaka, *et al.*, Jpn. J. Appl. Phys. **30** (10A), L1817 (1991).
9. A. M. Rao, Ping Zhou, Kai-An Wang, *et al.*, Science **259**, 955 (1993).
10. M. A. Khodorkovski, A. L. Shakhmin, S.V. Murashov, *et al.*, in *Proceedings of the 21st International Symposium on Rarefied Gas Dynamics, Marseille, 1998*, Vol. VIII, Special Session Molecular Beams, MB P-57, 58.
11. Jun Onoe and Kazuo Takeuchi, Phys. Rev. Lett. **79** (16), 2987 (1997).

Translated by P. Pozdeev

Technical Physics Letters, Vol. 27, No. 2, 2001, pp. 90–92. Translated from Pis'ma v Zhurnal Tekhnicheskoĭ Fiziki, Vol. 27, No. 3, 2001, pp. 7–13.

The Formation of Volume Elements for Microelectromechanical Systems in Polyimide by Method of Reactive Ion Beam Etching

A. I. Stognij, T. I. Orekhovskaya, Yu. V. Timoshkov, and S. V. Koryakin

Institute of Solid State and Semiconductor Physics, National Academy of Sciences of Belarus, Minsk, Belarus

e-mail: stognij@ifttp.bas-net.by

Received August 1, 2000

Abstract—The main problem related to the creation of microelectromechanical systems—the formation of an anisotropic profile with vertical side walls and clean flat bottom in a thick resist film—is experimentally solved by optimizing the parameters of the reactive ion beam etching process for polyimide (PI) layers with a thicknesses up to 50 μm. The optimized technique was used to form the volume parts of a microelectromotor structure by etching a PI film with an oxygen ion beam (beam current density $j = 0.5$ mA/cm^2; ion extraction energy $U = 800$ V). © *2001 MAIK "Nauka/Interperiodica".*

The large importance of investigations aimed at the creation of new and optimization of the existing methods of plasma etching for the processing of organic films is related to the development of microelectronics, which proceeds both in the direction of miniaturization and toward integration with some other technologies. An example of the latter trend is offered by investigations aimed at the creation of devices of a new type, the so-called microelectromechanical systems (MEMS) combining the microelectronic and miniature mechanical components [1, 2]. For manufacturing such devices, of special importance from the scientific-technological standpoint is the problem of forming a MEMS element structure with an anisotropic profile in organic films with thicknesses ranging from a few dozen to several hundred microns.

In microelectronics, the methods of anisotropic plasma etching are conventionally employed for the processing of resist layers with thicknesses on the order of one micrometer [3]. The required profile is usually obtained within a few minutes. In view of this short-time process duration, problems related to the heat removal from a polymer target or to the plasma-induced polymer structure modification can usually be ignored or play a secondary role [4, 5]. In contrast, the situation is not as simple in the case of etching of thicker organic layers. For example, it was demonstrated [6] that the films of polyamic acid with thicknesses above 6 μm etched in an oxygen plasma exhibit the effect of explosion-like acceleration of the etching process. The explosion-like etching kinetics is related to a chemical reaction initiated and proceeding in the bulk of the polymer film. This reaction can be additionally accelerated by the sample heating caused by exothermal oxidation reactions occurring on the sample surface. It was indicated [6] that the sample surface temperature may reach up to 600 K at a bulk temperature below 450 K. This circumstance must be taken into account in considering the problem of stability of a polymer and a metal mask in the course of prolonged etching of real structures.

It must be noted that the ion etching of thick (10–100 μm) organic (polymer) films in a gas mixture of, e.g., oxygen and argon (where no explosion-like etching acceleration is observed [6]) proceeds at a markedly slower rate than the process in pure oxygen. For this reason, the etching duration, according to estimates [4–6], may increase to take up dozens to several hundreds of minutes. Moreover, during this time the metal of the mask sputtered with argon ions will be continuously supplied to the open surface of the polymer film, markedly affecting the etching kinetics. The thickness of a sputtered metal layer may reach several hundred nanometers.

Below we will demonstrate that the required profiles of MEMS elements in polyimide (PI) samples with standard metal masks can be obtained by method of reactive ion beam etching.

The PI films with thicknesses up to 50 μm, based on pyromellitic anhydride and diaminodiphenyl oxide, were deposited onto standard 100-mm-diam silicon wafers by centrifuging technique. The subsequent imidization process was carried out in a nitrogen atmosphere at 620 K. Prior to obtaining the polymer film, a transition 1.0-μm-thick copper layer and a 0.2-μm-thick chromium adhesion layer were formed on the plate surface by method of thermal deposition. Using the conventional thermal deposition and photolithography methods, a 0.8-μm-thick aluminum mask with a required pattern of MEMS elements was formed on the PI film surface.

The reactive ion beam etching process was performed using a modified wide-aperture ion source with

1063-7850/01/2702-0090$21.00

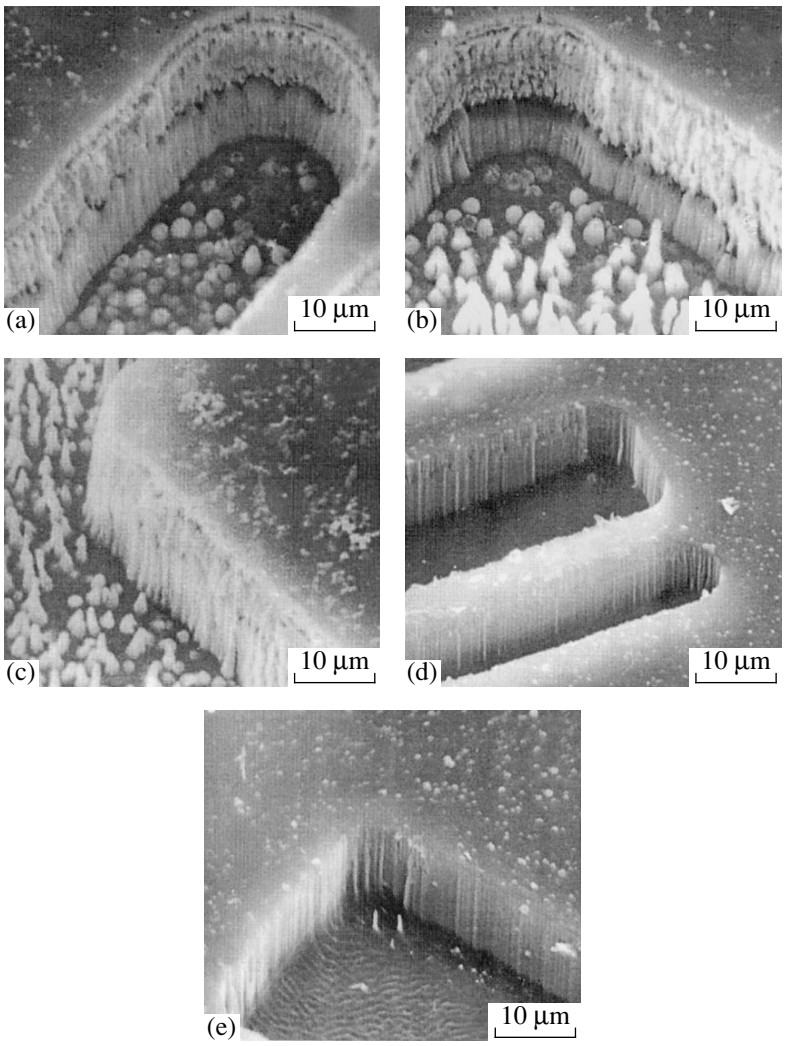

Fig. 1. Images of the volume figures in a PI film obtained by method of reactive ion beam etching: (a) working medium, 80% O_2 + 20% Ar, $j = 0.4$ mA/cm^2, $U = 2000$ V; (b) 95% O_2 + 5% Ar, $j = 0.6$ mA/cm^2, $U = 1400$ V; (c) 100% O_2, $j = 0.6$ mA/cm^2, $U = 1400$ V; (d) 100% O_2, $j = 0.5$ mA/cm^2, $U = 1000$ V; (e) 100% O_2, $j = 0.5$ mA/cm^2, $U = 800$ V.

cold hollow cathode [4]. The working gas (oxygen or an oxygen–argon mixture) was admitted via the ion source. The ion beam current density j could be varied from 0.2 to 0.8 mA/cm^2; the ion extraction energy, from 400 to 2000 V. The temperature regime was monitored with the aid of thermocouples contacting with the sample.

Preliminary experiments showed that the sample heating above 400 K in the course of etching leads to exfoliation and cracking of the mask. For this reason, the films were processed by alternating the cycles of etching and cooling in vacuum, so that the sample temperature did not exceed 350 K. The state of the samples in various stages of etching was monitored by optical microscopy (NU-2 polarization microscope) and scanning electron microscopy (Nanolab-9 electron microscope).

Figure 1 shows typical images of some characteristic elements formed in PI films in the course of optimization of the ion beam etching process parameters (observation angle 60°; aluminum mask removed). Previously [4], it was established that optimum etching regimes for a thin PI layer are provided by using a mixture of oxygen with 20% of argon and the ion beam with $j = 0.4$ mA/cm^2 and $U = 2000$ V. Figure 1a shows a typical profile obtained upon etching in this regime. The profile has a height above 20 μm and exhibits vertical side walls without a lateral etching wedge. However, the walls possess an inhomogeneous structure that can be visually divided into three layers. The bottom layer retains the structure of initial polyimide. The thin top and thick intermediate layers represent PI modified to more or less pronounced extent as compared to the initial polymer.

A possible reason for the PI modification and stratification may be the rapid transfer of heat liberated in the mask during the ion bombardment, accumulation of

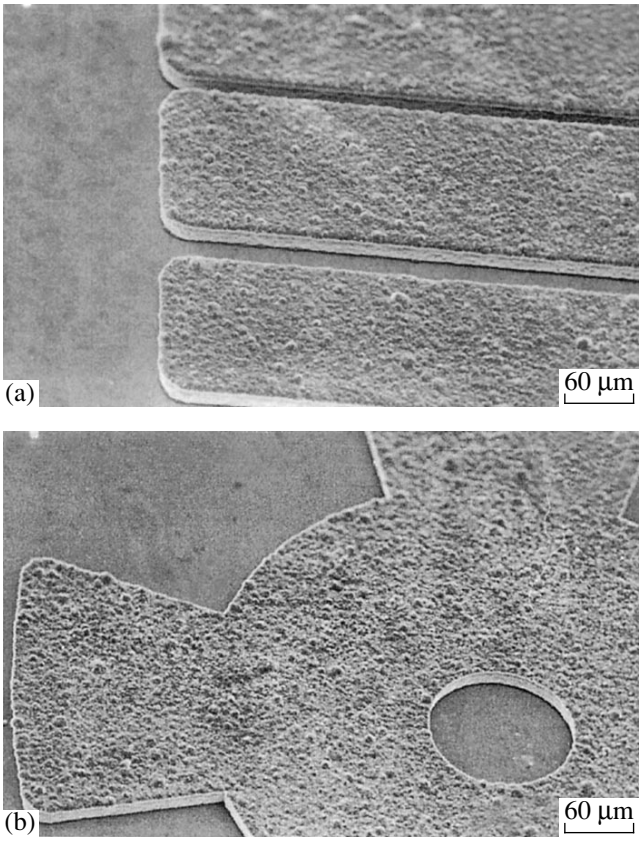

Fig. 2. Images of some parts of a microelectromotor of (a) elongated and (b) rounded shape formed by the reactive ion beam etching under optimum conditions (pure oxygen, $j = 0.5$ mA/cm^2, $U = 800$ V).

this heat in the bulk of PI, and subsequent effective removal through the chromium adhesion layer to the substrate and the substrate holder. As a result of this heat transfer process, the system features thermal stresses leading to the PI stratification, impairing the conditions of heat removal from polymer and causing redistribution of the thermal fluxes in the mask. In order to eliminate this drawback, it was sufficient to pass to less rigid ion irradiation conditions.

In addition, Fig. 1a shows that the bottom of the etched profile is covered by coarse rounded particles. Examination of the sample in the optical microscope showed that the particles are composed of a dark material, are loosely bound to the sample surface, and can be readily removed with a soft brush. At the same time, the particles were poorly sputtered and could not be removed in this way even when the polymer layer was sputtered off to expose the substrate. We believe that these particles may form as a result of sputtering of the aluminum mask, which fall onto the etched PI surface through windows in the mask. As is known, aluminum (and the more so aluminum oxide) is characterized by a much (more than one order of magnitude) lower sputtering rate as compared to that of PI (the average rate of PI etching was 0.2 μm/min) [3]. Therefore, the products of mask sputtering would accumulate within the windows (partly screening PI from the ion beam action). This hypothesis was confirmed by etching a nonmasked PI sample with a thickness below 30 μm, whereby no formation of dark rounded particles described above was observed.

The main steps in solving the problems described above are illustrated in Fig. 1. Figure 1b shows a profile obtained by etching in a mixture of oxygen containing 5% of argon, and the ion beam with $j = 0.6$ mA/cm^2 and $U = 1400$ V. As seen, the pattern of stratification on the side walls is still retained, but the inhomogeneities on the profile bottom acquire a shape elongated toward the surface, possess a smaller size, and occupy a smaller area as compared to those in Fig. 1a. Figure 1c shows a profile etched in pure oxygen at $j = 0.6$ mA/cm^2 and $U = 1000$ V. As seen, there is almost no evidence of stratification (although the side wall is still inhomogeneous in the vertical direction). The roughnesses on the bottom are still more elongated, smaller in size, and occupy even lower area.

The profile in Fig. 1d was obtained in pure oxygen at $j = 0.5$ mA/cm^2 and $U = 1000$ V. Here, the side walls are vertical and the bottom is free from roughnesses. However, the PI structure at the surface is somewhat different from that in the other part of the film. Figure 1e shows a profile with vertical homogeneous side walls and clean bottom. The wavy bottom relief was eliminated within a few minutes of etching upon reaching the chromium layer. This pattern was obtained by etching in pure oxygen at $j = 0.5$ mA/cm^2 and $U = 800$ V. The average rate of PI etching was 0.26 μm/min and the total duration of the etching and cooling cycles was about 100 min.

Thus, the method of reactive ion beam etching can be successfully used to form volume MEMS elements in PI films. To confirm this conclusion, Fig. 2 shows the images of some parts of a microelectromotor formed by a combination of the reactive ion beam etching, chemical etching, and electrolytic nickel deposition processes.

REFERENCES

1. B. Lochel, A. Maciossek, M. Konig, *et al.*, Microelectron. Eng. **23**, 455 (1994).
2. B. Lochel, A. Maciossek, H. J. Quenzer, and B. Wagner, J. Electrochem. Soc. **143** (1), 237 (1996).
3. *VLSI Electronics Macrostructure Science*, Vol. 8: *Plasma Processing for VLSI*, Ed. by N. G. Einspruch and D. M. Brown (Academic, New York, 1984).
4. A. I. Stognij and V. V. Tokarev, Prib. Tekh. Éksp., No. 3, 142 (1990).
5. H. Kinoshita, Vacuum **55**, 77 (1999).
6. I. I. Amirov, Zh. Tekh. Fiz. **70** (5), 106 (2000) [Tech. Phys. **45**, 627 (2000)].

Translated by P. Pozdeev

Technical Physics Letters, Vol. 27, No. 2, 2001, pp. 93–96. Translated from Pis'ma v Zhurnal Tekhnicheskoĭ Fiziki, Vol. 27, No. 3, 2001, pp. 14–21.

On the Adiabatic Theorem in Quantum Mechanics

A. G. Chirkov

St. Petersburg State Technical University, St. Petersburg, Russia

Received September 22, 2000

Abstract—The adiabatic and postadiabatic approximations, as well as the adiabatic and nonstationary perturbation theories, are constructed using a canonical averaging method under the assumptions which are more general than those used in the existing theories. An asymptotic evaluation of the proximity of rigorous and approximate solutions is performed. © *2001 MAIK "Nauka/Interperiodica".*

In the passage from the theory of quanta developed by Planck and Einstein to quantum mechanics, an important role belonged to the adiabatic theory of Ehrenfest. In 1928, Born and Fock [1] showed that the Ehrenfest hypothesis follows from the postulates of quantum theory. A rigorous mathematical proof of the adiabatic theory was given in 1949 by Kato [2]. Later, an analogy between the adiabatic and quasiclassical approximations served a basis for the Landau–Dykhne theory [3–5]. However, the Born–Fock adiabatic approximation is essentially not an approximated theory because all terms of the Born–Fock adiabatic series are of the same order of smallness [4, 6]; this, in turn, does not allow the corresponding postadiabatic approximation to be constructed. Selecting real wavefunctions (the Born–Fock condition) does not allow this adiabatic approximation to be used in the problems concerning the magnetic field. The results of the Landau–Dykhne adiabatic approximation only approximately pass to those of the nonstationary perturbation theory. Moreover, both adiabatic approximations give incorrect values of the preexponential term [4].

In a nonstationary case, there arises an important question about a time interval for which an approximate solution only slightly differs from the exact solution. This problem is not even mentioned in the above theories.

In this study, the adiabatic and postadiabatic approximations, as well as the adiabatic and nonstationary perturbation theories, are constructed using general formulas based on a canonical averaging method. The main assumptions of the Born–Fock theory are rejected. The main subject for the investigation in the nonrelativistic quantum theory is the Schrödinger equation [5]:

$$i\hbar\frac{\partial\Psi(q,t)}{\partial t} = \hat{H}\Psi(q,t), \qquad (1)$$

where $i^2 = -1$; $\hbar = 1.054 \times 10^{-27}$ erg s is the Planck constant; $q = (q_1, q_2, \ldots, q_n)$ is, generally speaking, a point in the configuration space of the corresponding classical system; t is the time; $\Psi(q, t)$ is a complex function with integrable square modulus; $\hat{H}$ is a self-conjugated (symmetric) operator defined in the Gilbert space. The Schrödinger equation (1) must be solved jointly with appropriate initial $\Psi(q, 0) = \Psi_0(q)$ and certain boundary conditions.

A situation studied in the nonstationary perturbation theory arises when the operator $\hat{H}$ can be represented as a sum of two self-conjugated operators: $\hat{H} = \hat{H}_0 + \varepsilon\hat{V}(q, t)$ $(0 < \varepsilon \ll 1)$. In the adiabatic approximation, the perturbation operator $\hat{V}(q, t)$ is not small and depends on the slow time $\tau = \varepsilon t$ so that $\hat{V}(q, t) = \hat{V}(q, \tau)$. Here, the solution must be constructed for the asymptotically large times $t \sim 1/\varepsilon$, when a change in the perturbation operator is large. In this case, separation of the total Schrödinger operator $\hat{H}$ into the sum of two operators—generating (unperturbed) and perturbation—is no longer expedient. Therefore, in order to include both possibilities, let us consider the problem (1) with a time-dependent Schrödinger operator $\hat{H} = \hat{H}(q, t)$.

Let us assume that a stationary problem corresponding to Eq. (1) is solvable for a parametric time dependence of the Schrödinger operator and has a discrete spectrum with the corresponding eigenfunctions and eigenvalues:

$$\hat{H}(t)\psi_n(q,t) = E_n(t)\psi_n(q,t), \qquad (2)$$

where the time t is fixed. The eigenfunctions are orthonormalized in the conventional sense:

$$\int_{-\infty}^{\infty}\psi_m(q,t)\bar{\psi}_n(q,t)dq = \delta_{mn} \qquad (3)$$

(the upper bar denoting complex conjugation).

Let us search for a solution to the rigorous problem (1) in the following form:

$$\Psi(q, t) = \sum_n c_n(t)\psi_n(q, t)\exp\left\{-i\int_0^t \Omega_n(z)dz\right\}, \quad (4)$$

where $\Omega_n(t) = \omega_n(t) + \nu_{nn}(t)$, $\omega_n(t) = E_n(t)/\hbar$, and $\nu_{nn} = -i\int_{-\infty}^{\infty} \bar{\psi}_n \frac{\partial \psi_n}{\partial t} dq$. The meaning of this phase selection will become clear below. Substituting (4) into (1), we obtain equations for the expansion coefficients $c_m(t)$

$$\dot{c}_m(t) = -i\sum_{m,n}{}' \nu_{mn}c_n \exp\left\{i\int_0^t \Omega_{mn}(z)dz\right\}, \quad (5)$$

where the upper dot denotes the total derivative with respect to time and the dash at the sum symbol indicates the absence of a diagonal term with $m = n$. The matrix of coefficients ν_{mn} has the form

$$\nu_{mn} = -i\int_{-\infty}^{\infty} \psi_m(q, t)\frac{\partial \psi_n(q, t)}{\partial t} dq \quad (6)$$

and is Hermitian ($\nu_{mn} = \bar{\nu}_{nm}$).

It is the phase selected as indicated in (4) that accounts for the absence of the diagonal term (responsible for the main resonance) in the above sum. If this term were present, the sum (5) would contain a small resonance denominator. Indeed, differentiating Eq. (2) with respect to time and taking into account that the Schrödinger operator is self-conjugated, we obtain

$$\nu_{mn} = (i/\hbar\omega_{mn})(\partial\hat{H}/\partial t)_{mn}, \quad m \neq n. \quad (7)$$

Evidently, in the case of real eigenfunctions ($\bar{\psi}_n = \psi_n$), the diagonal elements are zero ($\nu_{nn} = 0$). This fact was a reason for selecting a real norm in the Born–Fock approximation.

Analogous considerations in the case of $m = n$ lead to the Gell-Mann–Feynman theorem $(\partial\hat{H}/\partial t)_{nn} = \partial E_n/\partial t$ and do not determine the diagonal matrix elements. If the Schrödinger operator depends on time τ via a set of functions $\xi_i(\tau)$ ($i = 1, 2, \ldots, N$), the elements ν_{nn} determine the topological adiabatic Berry's phase [8], the value of which is independent of the evolution time and determined only by a close contour in the space of parameters.

Using relationships (7), we may readily separate three cases in which the perturbation theory can be constructed. In the adiabatic case, $\hat{H} = \hat{H}(\xi(\tau))$, so that $\partial\hat{H}/\partial t = \varepsilon(\partial\hat{H}/\partial\xi)(\partial\xi/\partial\tau)$. The second case corresponds to the nonstationary perturbation theory, with the Schrödinger operator having the form $\hat{H} = \hat{H}_0 + \varepsilon\hat{V}(q, t)$. Finally, the adiabatic perturbation theory corresponds to $\hat{H} = \hat{H}_0 + \varepsilon\hat{V}(q, \tau)$.

The set of equations (5), supplemented by a complex-conjugated relationships, is a Hamiltonian system (in the classical sense) with the Hamiltonian operator

$$H(c, c^*, t) = -i\sum_{m,n}{}' \nu_{mn}(t)c_n c_m^* \exp\left\{i\int_0^t \Omega_{mn}(z)dz\right\} \quad (8)$$

describing a classical distributed system. The property of being the Hamiltonian system, which is ensured by the Hermitian matrix of coefficients ν_{mn}, allows us to use a phase perturbation theory (canonical averaging method) developed previously [7].

In the adiabatic case, we will assume the Schrödinger operator to have the form $\hat{H} = \hat{H}_0 + \hat{V}(q, \xi(\tau))$, where $\tau = \varepsilon t$ is the slow time). Then the matrix elements can be expressed as $\nu_{mn} \sim \varepsilon\xi'$ and the Hamiltonian (8) can be represented as

$$\varepsilon\hat{H}_1(c, c^*, t, \tau) = -i\varepsilon\sum_{m,n}{}' \nu_{mn}(\tau)c_n c_m^* \exp\left\{i\int_0^t \Omega_{mn}(\tau)dt\right\}, \quad (9)$$

where $\dot{\tau} = \varepsilon$ and $\Omega_{mn} = \Omega_m - \Omega_n$.

The canonical form of this function allows us to pass to the evolution equations using the results obtained in [7]:

$$\bar{H}^{(2)}(\bar{c}, \bar{c}^*, \tau) = \varepsilon\bar{H}_1(\bar{c}, \bar{c}^*, \tau) + \varepsilon^2\bar{H}_2(\bar{c}, \bar{c}^*, \tau),$$
$$\bar{H}_1 = \langle H_1\rangle, \quad (10)$$
$$\bar{H}_2 = (-\langle(\partial\tilde{H}_1/\partial c^*)(\partial\{H_1\}/\partial c)\rangle),$$

where $\bar{H}^{(2)}$ is the second approximation for the averaged Hamiltonian; $\bar{c} = (\bar{c}_1, \bar{c}_2, \ldots)$, $\bar{c}^* = (\bar{c}_1^*, \bar{c}_2^*, \ldots)$ are the evolution components of the variables c, c^*; and

$$\langle f\rangle = \lim_{T\to\infty}\frac{1}{T}\int_{t_0}^{t_0+T} f(\bar{c}, \bar{c}^*, t)dt,$$
$$\tilde{f}(\bar{c}, \bar{c}^*, t) = f(\bar{c}, \bar{c}^*, t) - \langle f\rangle, \quad (11)$$
$$\{f\} = \int\tilde{f}(\bar{c}, \bar{c}^*, t)dt.$$

Using relationships (10), the first approximation $c_k^{(1)}$ for the variables c_k is constructed using the formulas $c_k^{(1)} = \bar{c}_k$, where $\bar{c}_k$ is determined from the equa-

tions $\dot{c}_k = \varepsilon(\partial \bar{H}_1/\partial \bar{c}_k^*)$. The second approximation $c_k^{(2)}$ for the variables c_k is constructed by the formulas

$$c_k^{(2)} = \bar{c}_k + \partial\{H_1\}/\partial \bar{c}_k^*, \quad (12)$$

where $\bar{c}_k$ is determined from the equations

$$\dot{\bar{c}}_k = \partial \bar{H}^{(2)}/\partial \bar{c}_k^*. \quad (13)$$

Upon averaging Eq. (9) along the generating solution (c_k = const, τ = const), we obtain $\bar{H}_1 = \langle H_1 \rangle = 0$, which implies that $\dot{\bar{c}}_k = 0$. The latter result is equivalent to the adiabatic Kato theorem [2] (for the proof, see, e.g., [9]), which is derived here virtually without calculations. In the classical sense, the evolution components $\bar{c}_k$ of the initial variables c_k are the adiabatic invariants [10]; that is, they retain the initial values for the asymptotic times $t \sim 1/\varepsilon$. In deriving this result, we must assume that $\Omega_{mn}(t) \neq O(\varepsilon)$; i.e., the system does not exhibit degeneracy, there are no close levels, and the levels do not intersect in course of evolution.

In the adiabatic (first) approximation, a solution to the Schrödinger equation has the following form:

$$\Psi^{(1)}(q, t) = \sum_{n=0}^{\infty} c_n^{(1)} \psi_n(q, t) \exp\left\{-i\int_0^t \Omega_n(z)dz\right\}. \quad (14)$$

Evaluation of the difference $|\Psi(q, t) - \Psi^{(1)}(q)| < C\varepsilon$ for the asymptotic times $t \sim 1/\varepsilon$ (C is a constant quantity independent of ε) under sufficiently general assumptions can be obtained from the Los' theorem [11].

The second (postadiabatic) approximation can be constructed using relationships (10)–(13). After simple calculations, we obtain

$$\bar{H}_2 = -i\sum_k \Delta\Omega_k(\tau)\bar{c}_k\bar{c}_k^*, \qquad \Delta\Omega_k = \sum_l{}' \frac{|V_{kl}|^2}{\Omega_{kl}}, \quad (15)$$

which leads to the following expression for the averaged Hamiltonian function:

$$\bar{H}^{(2)} = -i\varepsilon^2\sum_k \Delta\Omega_k(\tau)\bar{c}_k\bar{c}_k^*. \quad (16)$$

The Hamiltonian equation (13) with the function (16) for the evolution components $\bar{c}_k$ is readily integrated to yield

$$\bar{c}_k = A_k \exp\left\{-i\varepsilon^2\int_0^\tau \Delta\Omega_k(z)dz\right\} = A_k\exp(-i\alpha_k), \quad (17)$$

where A_k are the constants determined from the initial conditions. Note that, evidently, the phase of coefficients $\bar{c}_k$ could be included into the initial expansion (4). In this case, we would obtain $\bar{H}_2 = 0$ and $\bar{H}^{(2)} = 0$.

The second approximation for the coefficients of expansion (4) is constructed using the formulas (12) and (13):

$$c_k^{(2)} = A_k^{(2)}\exp(-i\alpha_k) - \varepsilon\sum_m{}' \frac{V_{km}}{\Omega_{km}} A_m \exp(-i\alpha_m + i\Omega_{km}t). \quad (18)$$

Using the coefficients $c_k^{(2)}$, we obtain the second approximation $\Psi^{(2)}(q, t)$ for a solution to the Schrödinger equation:

$$\Psi^{(2)}(q, t) = \sum_k \left[A_k\exp(-i\alpha_k) - \varepsilon\sum_m{}' \frac{V_{km}}{\Omega_{km}} A_m \exp(-i\alpha_m - i\Omega_{km}t)\right] \times \Psi_k \exp\left[-i\int_0^t \Omega_k(z)dz\right]. \quad (19)$$

Note that the summands in Eqs. (18) and (19) can be restricted to the first approximation $A_m^{(1)}$ with respect to ε for the integration constants.

In the case of the Cauchy problem, the system occurs at the initial instant in a certain stationary state with a discrete spectrum of the nonperturbed problem with the Schrödinger operator $\hat{H}_0$, for example, in the sth state with $\Psi(q, t)|_{t=0} = \Psi_s^0$. Here, in contrast to the stationary state, it is not possible to take $c_n|_{t=0} = \delta_{ns}$ because the expansion is always performed over the eigenfunctions of the perturbed problem $\psi_n(q, t) = \psi_n(q, \xi(t))$, where $\xi(t)$ are the parameters determining the time dependence of the perturbation. Therefore, we will additionally assume the perturbation to be switched in a way such that $\xi(0) = \dot{\xi}(0) = 0$. The problem can also be solved under some other conditions, which would imply a combination of the instantaneous switching followed by adiabatic variation.

Thus, we assume that the equation for determining the coefficients A_k has the following form:

$$c_k|_{t=0} = \delta_{ks} = A_k - \varepsilon\sum_m{}' \left[\frac{V_{km}(\tau)}{\Omega_{km}(\tau)}\right]_{t=0} A_m. \quad (20)$$

Apparently, the matrix elements are $V_{km} \sim \dot{\xi}(\tau)$ and,

under the conditions adopted, we obtain $A_{ks} = \delta_{ks}$; that is,

$$c_{ks}^{(2)} = \delta_{ks}\exp(-i\alpha_k) - \varepsilon\frac{V_{ks}}{\Omega_{ks}}\exp(-i\alpha_s + i\Omega_{ks}t). \quad (21)$$

Finally, the second (postadiabatic) approximation $\Psi^{(2)}$ for the wavefunction acquires the following form:

$$\Psi^{(2)}(q, t) = \psi_s\exp\left[-i\int_0^t\Omega_s(z)dz\right] - \sum_k{}'\frac{V_{ks}}{\Omega_{ks}}\psi_k\exp\left[i\Omega_{ks}t - i\alpha_s - i\int_0^t\Omega_k(z)dz\right]. \quad (22)$$

It is possible to show [1] that we may use an estimate $|\Psi(q, t) - \Psi^{(2)}(q, t)| < B\varepsilon^2$ for the time $t \sim 1/\varepsilon$. In the physical works, the finiteness of the time interval for which the approximate solution approximates the rigorous solution is ignored.

In the case of the adiabatic perturbation theory, the results are obtained from the corresponding expressions for the adiabatic approximation with an allowance for additional smallness of the perturbation amplitude.

REFERENCES

1. M. Born and V. Fock, Z. Phys. **51**, 165 (1928).
2. T. Kato, J. Phys. Soc. Jpn. **5**, 435 (1950).
3. A. M. Dykhne, Zh. Éksp. Teor. Fiz. **38** (2), 570 (1960) [Sov. Phys. JETP **11**, 411 (1960)].
4. A. M. Dykhne, Zh. Éksp. Teor. Fiz. **41** (4), 1324 (1961) [Sov. Phys. JETP **14**, 941 (1962)].
5. L. D. Landau and E. M. Lifshitz, *Quantum Mechanics: Non-Relativistic Theory* (GIFML, Moscow, 1963; Pergamon, New York, 1977).
6. N. B. Delone and V. P. Kraĭnov, *Atom in a Strong Light Field* (Énergoatomizdat, Moscow, 1984).
7. A. G. Chirkov and I. V. Kazinets, Pis'ma Zh. Tekh. Fiz. **26** (8), 8 (2000) [Tech. Phys. Lett. **26**, 318 (2000)].
8. S. I. Vinitskiĭ, V. L. Derbov, V. N. Dubovik, *et al.*, Usp. Fiz. Nauk **160** (6), 1 (1990).
9. A. Messiah, *Quantum Mechanics* (North-Holland, Amsterdam, 1962; Nauka, Moscow, 1979), Vol. 2.
10. V. I. Arnol'd, *Supplementary Chapters of The Theory of Ordinary Differential Equations* (Nauka, Moscow, 1978).
11. F. S. Los', Ukr. Mat. Zh. **2** (3), 87 (1950).

Translated by P. Pozdeev

Technical Physics Letters, Vol. 27, No. 2, 2001, pp. 97–101. Translated from Pis'ma v Zhurnal Tekhnicheskoĭ Fiziki, Vol. 27, No. 3, 2001, pp. 22–30.

"Color" Dynamics Based on a Conservative System

O. I. Gorskiĭ and Yu. P. Kuchugurnyĭ

Institute of Transport Systems and Technologies, National Academy of Sciences of Ukraine, Dnepropetrovsk, Ukraine

Received July 3, 2000

Abstract—A method of two-color painting for the total average energy of a nonlinear chain of oscillators mapped on a plane is proposed. The map is shown to possess a certain structure. It is suggested that this structure is due to a conservative system dynamics. © *2001 MAIK "Nauka/Interperiodica".*

Introduction. As is known, the relaxation time of a nonlinear chain of N oscillators in a conservative Hamiltonian system can be evaluated using the method of spectral entropy [1]. This method gives a rough estimate of the time necessary for relaxation of the system to an equilibrium state characterized by the equiprobable energy distribution over the degrees of freedom. As noted in [1], the relaxation time is roughly estimated by $\tau_{FPU} \sim 10^{-3}$ s in the Fermi–Past–Ulam α-model. This means that the equiprobable energy distribution over the degrees of freedom cannot be attained in the computer experiment. A weak time dependence of the spectral entropy and the absence of data on the features of this dependence allow us to only roughly estimate the relaxation time.

For determining the characteristic times of a nonlinear chain of oscillators, Casetti *et al.* [1] proposed a method based on the comparison of the Lyapunov indices of a given system to those of an integrable dynamic system. In [1], such an integrable dynamic system was represented by a chain of the Tode oscillators. A "bifurcation" of the Lyapunov indices for the two systems allows the trapping time of the studied system to be determined in the region of quasiperiodic oscillations. It was found that the trapping time is very small, amounting to $\tau_{FPU}^{(1)} \sim 4 \times 10^5$ cycles or 10^{-9}–10^{-10} s, which is much shorter than the predicted time of attaining the state with equiprobable energy distribution over the degrees of freedom. The method of Lyapunov can be used to predict the time when the system would leave the region of quasiperiodic tores, but this method is incapable for predicting the subsequent system behavior. This stimulates the search for new methods capable of determining the characteristic times of a nonlinear chain of oscillators.

Below, we propose an approach, called the painting method, which is based on the rough (to a certain approximation) mapping of a system onto a plane. The map is allowed to developed in time. In every time step, the map is given color C_1. If the approximation is determined by the area Δs with color C_1, then (upon elapse of a certain computer modeling time $\Delta\tau$) the region to which the system is mapped also acquires color C_1. In order to avoid limitations on $\Delta\tau$ related to the rough approximation (coarse-grain structure), we may use the following method. At a certain time instant t_1, when some part of the region has color C_1, this color is changed to C_2 (background color) and then (for $t_1 < t \leqslant t_2$) the mapping is performed using color C_2 (the part of the region that was colored C_1 retains this color until $t \leqslant t_1$, provided that the oscillator does not fall within this region during the time $t_1 < t \leqslant t_2$; otherwise, the color is changed). Upon elapse of the time t_2, color C_1 is returned for the subsequent mapping. The following cycles are organized in the same way. Thus, all regions in the coarse-grain states are identically painted with changing colors. At the end of each cycle with the period $t_1 + t_2$, we calculate the number C_1^* of the graphical pixels possessing color C_1, this number called the residual color. We are interested in establishing how the residual color C_1^* can help us reveal the characteristic times of the main conservative system.

Which mapping on the plane should be used? In this study, we will consider the self-mapping of the total energy of each oscillator E^i in each nth time step, that is, to E^i in the $n + m$ step ($E_n^i \longrightarrow E_{n+m}^i$). Each of the N oscillators is mapped on the same plane, which allows a certain portrait of the system to be obtained without recourse to the phase space. It should be noted that no data are available concerning the features of oscillations in the phase space in the case of complete dynamic mixing and equiprobable energy distribution over the degrees of freedom. In [1], it was assumed that a dynamic mixing in the phase space for a nonlinear chain of oscillators requires that the energy is sufficiently large and the initial distribution of the coordinates and momenta of the oscillators is random (nearly Gaussian). It was concluded that, provided the system in the initial state occurred in the lowest mode (even with a large total energy), the equiprobable energy dis-

1063-7850/01/2702-0097$21.00 © 2001 MAIK "Nauka/Interperiodica"

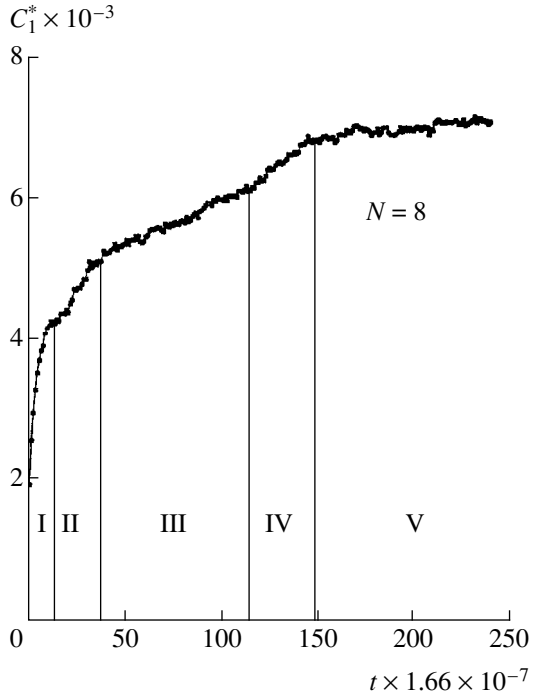

Fig. 1. A typical time variation of the residual color.

tribution is not likely to be attained and the energy of the lowest mode will be pumped to several nearest-neighbor modes and back, as it was in the original Fermi–Past–Ulam. The main purpose of our work is to show that the "color" dynamics based on a conservative system reveals some features of the main conservative system. For this purpose, we have studied time variation of the residual color C_1^*.

Description of model and results. We have modeled a nonlinear chain of the Fermi–Past–Ulam type with the interaction Hamiltonian

$$H(p, q) = \sum_{i=1}^{N}\left[\frac{1}{2}p_1^2 + \frac{1}{2}(q_{i+1} - q_i)^2 + \frac{\alpha}{3}(q_{i+1} - q_i)^3\right]. \quad (1)$$

The equations of motion for a chain of oscillators are as follows:

$$\ddot{q}_i = q_{i-1} - 2q_i + q_{i+1} + \alpha(q_{i+1} - q_i)^2 - \alpha(q_i - q_{i-1})^2, \quad i = 1, 2 \ldots N. \quad (2)$$

The displacements of terminal oscillators were assumed to be zero. The initial conditions for the momenta and coordinates were set in a random manner with the aid of a random number generator, with the condition that the total momentum of all oscillators is zero; the integration step was taken equal to 0.1, which approximately corresponds to 10^{-14} s for argon. Selection of the total energy E_n^i for each oscillator in the nth step and in the $(n + m)$th step was performed using an independent cyclic n-step counter. The n and m values were varied. In order to establish independence of the numerical modeling results on the times t_1 and t_2, these values were varied as well. At the end of each cycle with the $t_1 + t_2$ period, the residual color C_1^* was read.

The physical limitation on the coarse-grain structure (pixel size) has to be compensated. Therefore, it is necessary to determine dependence of the results of modeling on the following parameters: the time of action of the "color fluxes" t_1 and t_2, the sampling steps n and m, and some scale S compensating for the finite area of the graphic pixel. The large number of variable parameters considerably complicates the analysis of results. Special features of the system dynamics related to the variation of these parameters will be considered in a separate publication. Here, we restrict the consideration to the case of fixed parameters ($n = 500$, $m = 100$, $t_1 = t_2 = 25 \times 10^3$). The relative error of calculation of the total system energy was $\sim 10^{-5}$.

A typical behavior of $C_1^*(t)$ for sufficiently large times (in comparison to the trapping time $\tau_{\mathrm{FPU}}^{(1)}$) is as follows (the number of oscillators was taken $N = 8$, because the features of "color" dynamics are most pronounced for the maximum number of oscillators). The $C_1^*(t)$ value initially rapidly increases with time (Fig. 1, region I), this stage lasting for a time period of $\sim(10–20)\tau_{\mathrm{FPU}}^{(1)}$. Then the growth rate of $C_1{}^*(t)$ exhibits a change in comparison to that for the initial stage (Fig. 1, region II). After a time period of $\sim(20–40)\tau_{\mathrm{FPU}}^{(1)}$, depending on the number of oscillators, the growth rate of the residual color exhibits a new change (Fig. 1, region III). Variation of the slope of the $C_1^*(t)$ curve in Fig. 1 may be indicative of the possible characteristic times of the system of eight oscillators. Then the slope of the $C_1^*(t)$ curve changes again (region IV) and attains a plateau (region V). The length of the plateau is very large ($\sim 100\tau_{\mathrm{FPU}}^{(1)}$ cycles). The map ($E_n^i \longrightarrow E_{n+m}^i$) acquires a characteristic shape, which becomes more pronounced as the calculation proceeds. The calculation was terminated after accomplishing $t \sim 1.2 \times 10^8$ cycles.

Discussion of numerical modeling results. The results of the calculation indicate that the map ($E_n^i \longrightarrow E_{n+m}^i$) acquires a certain structure. Figures 2a–2c show the map ($E_n^i \longrightarrow E_{n+m}^i$) for a small number of oscillators ($N = 4$) in the following cases. Case (a) corresponds to a chain of linear ($\alpha = 0$) oscillators with the initial first mode and zero initial momenta; case (b) represents nonlinear oscillators ($\alpha = 0.25$) with the initial coordinates set on a sinusoid with a maximum spatial

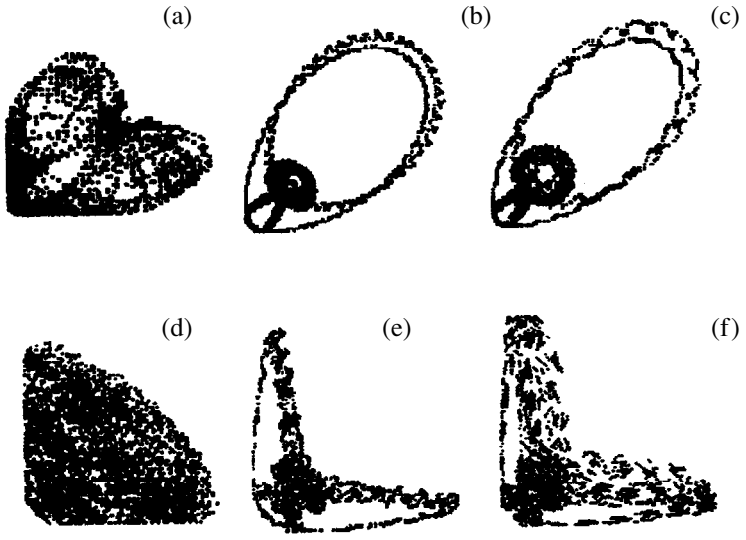

Fig. 2. The forms of $E_n^i \longrightarrow E_{n+m}^i$ maps for $N = 4$ (a–c) and 5 (d–f).

period (conditional first mode) and nonzero random initial momenta; case (c) corresponds to nonlinear oscillators ($\alpha = 0.25$) without the initial conditional first mode and with nonzero random initial momenta. In the case of a random initial distribution of coordinates and momenta (in the absence of conditional first mode), the map also has quite a complicated structure.

In principle, the form of the mapped region $E_n^i \longrightarrow E_{n+m}^i$ immediately shows the number of mapped oscillators because the form of the mapped region strongly depends on this number (see below) for at least a small number of oscillators. The strong dependence of the form of the mapped region on N probably leads to different dynamics on the way to mixing, since the possible localization of oscillations in the region of equiprobable energy distribution is most probably determined by the region of "states" occupied until the moment of mixing (in this work, the "state" is determined by a point on the $E_n^i \longrightarrow E_{n+m}^i$ map with color C_1).

The structure of the map changes with the number of oscillators. For the comparison, Figs. 2d–2f show the $E_n^i \longrightarrow E_{n+m}^i$ maps for $N = 5$ calculated under the same conditions as those used above for $N = 4$. As seen from these data, the map structure may be coarse for small values of the total oscillator energy (near the map region $E_n^i \longrightarrow \sim 0$). Unfortunately, it is not always possible to select the scale S so as to provide for a better resolution. This is one of the disadvantages of the proposed method.

The effect of nonlinearity α on the map structure for $N = 8$ is demonstrated in Fig. 3, where $\alpha = 0$ (a), 0.25 (b), 0.35 (c). The maps in Fig. 3a–3c were obtained for a constant value of the total energy per oscillator $E = 0.428$. As seen from Fig. 3d (curve *1*), the linear case may reveal oscillations related to the alternating "color flux." In addition, the slope of the $C_1^*(t)$ curve exhibits a change and the mapped region varies with α (in the case of strong nonlinearity). Figure 3b shows a conditional first mode with nonzero random initial momenta, while Fig. 3c corresponds to the absence of the conditional first mode (for the initial nonzero random momenta). It must be noted that setting the conditional first mode at the initial time instant determines the shape of the map, which (for a small number of oscillators) cannot be broken even after a very large computational time.

Figure 4 shows the maps for $N = 16$ in the linear case $\alpha = 0$ (a) and in the nonlinear case for $\alpha = 0.25$ with nonzero random initial momenta and with (b) and without (c) the initial conditional first mode. In all cases, the total energy per oscillator was $E^i = 0.550$. Figure 4d shows the time variation of $C_1^*(t)$ for all three cases (curves *1–3*, respectively). In this system, the map forms are rather similar despite the modification of the initial condition. For the linear chain, the slope of the $C_1^*(t)$ curve differs from that for the nonlinear case. A random distribution of momentum in the presence of conditional first mode (Fig. 4, curve *2*) and in the absence of this mode (Fig. 4, curve *3*) leads to different residual colors. Investigation of the $C_1^*(t)$ functions reveals a certain characteristic time $\tau_{\mathrm{PFU}}^{(2)} \sim 10\tau_{\mathrm{PFU}}^{(1)}$ that determines attaining of the first "color flux" stabilization. We may make attempt at increasing the first stabilization time by changing parameters of the conserva-

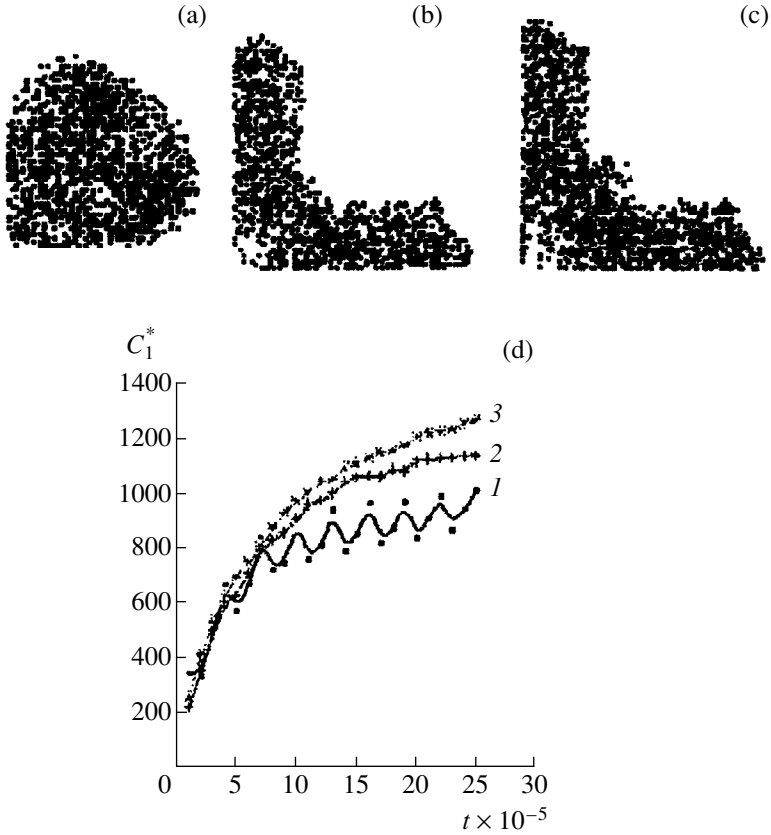

Fig. 3. Effect of the nonlinear interaction on the $E_n^i \longrightarrow E_{n+m}^i$ map structure for $N = 8$. See the text for explanation.

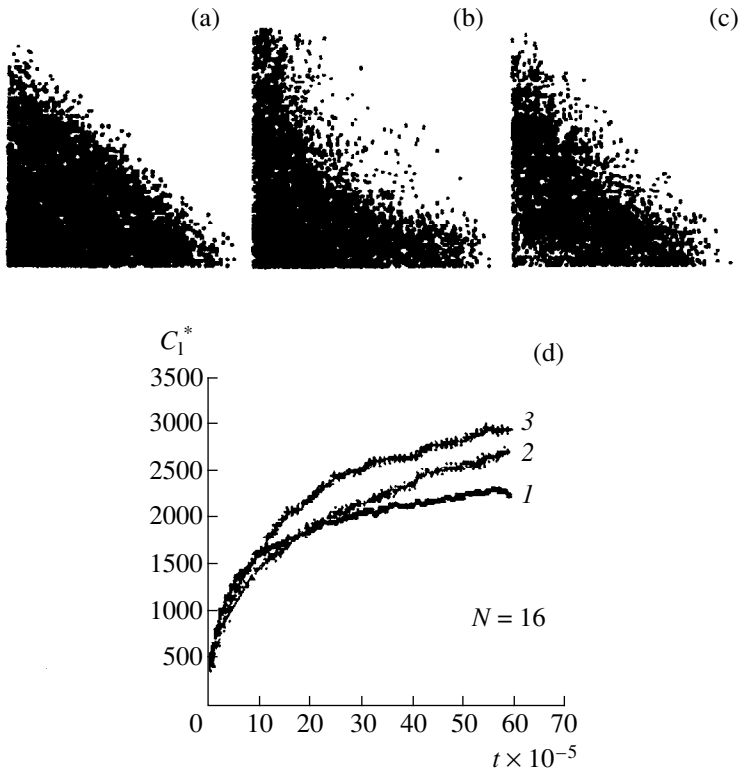

Fig. 4. Effect of the nonlinear interaction on the $E_n^i \longrightarrow E_{n+m}^i$ map structure for $N = 16$. See the text for explanation.

tive system (but not of the "color flux" parameters). A question naturally arises as to how the $\tau_{PFU}^{(2)}$ value depends on n, m, t_1, t_2, and S. Answering this question requires additional investigations. We may compare the results obtained by fixing either the total energy per oscillator or n, m, t_1, t_2, and S (otherwise, there is no any base for the comparison).

Conclusions. The main difficulty in the problem of dynamic justification of the statistical thermodynamics consists in that the first mode appearing in a conservative system cannot be broken from within the system (by forces of its own). As demonstrated above, the "color" dynamics reveals various structures of the map. How are these structures related to the dynamics of the conservative system and why are the fundamental forces insufficient to break these structures? In this stage of investigation, these questions cannot be answered. The revealed structures strongly depend on the number of oscillators and are not broken in the course of a prolonged modeling.

By the form of the map structure, we may determine the number of oscillators. The mapped region appears as divided into two parts: the region of $E^i \sim 0$ (during the calculation of $C_1(t)$* using the two-color map, this region does not contribute to the residual color) and the region of the energy that becomes accessible for the system after a very large computational time. For a more detailed study of the "color flux" dynamics, we may separate a region of the $E_n^i \longrightarrow E_{n+m}^i$ map with a different spatial scale S. This case would require additional investigation.

In this study, we restricted the consideration to calculating the equations of motion for a small number of particles, because the need in reading the residual color at the end of each cycle n strongly affects the modeling time. An increase in the number of oscillators N at a constant area on which the conservative system is mapped leads to a rougher approximation. One possible measure against this may consist in limiting the interval for E_n^i and increasing the scale of mapping. Of course, this implies a deliberate selection of the E_n^i interval, but (as far as we are interested in the equiprobable energy distribution over the degrees of freedom) the selection of this interval close to E seems to be quite reasonable. This was not done in our work.

REFERENCES

1. L. Casetti, M. Cerruti-Sola, and M. Pettini, chao-dyn/9609017.

Translated by P. Pozdeev